Composition and Luminescence Studies of InGaN and InAlN Alloys

Elaine Taylor-Shaw

A thesis submitted to
the Department of Physics
University of Strathclyde
for the degree of
Doctor of Philosophy

September 30, 2015

"Don't cry because it's over, smile because it happened."

- For my husband, parents, sister and gran.

Declaration of author's right

This thesis is the result of the author's original research. It has been composed by the author and has not been previously submitted for examination which has lead to the award of a degree.

The copyright of this thesis belongs to the author under the terms of the United Kingdom Copyright Acts as qualified by University of Strathclyde Regulation 3.50. Due acknowledgment must always be made for the use of any material contained in, or derived from, this thesis.

Signed: Date:

Abstract

III-nitride semiconductors are the leading material for use in solid state lighting (SSL), with highly efficient blue and white nitride-based light emitting diodes (LEDs) commercially available. However challenges still remain to improve their efficiency. The work in this thesis focuses on the optical and compositional characterisation of InGaN and InAlN alloys, which are widely used as active regions in such light emitters.

Composition and luminescence properties of InGaN epilayers with varying growth temperature and hydrogen flow rates are investigated. The measurements revealed that the samples grown with small amounts of hydrogen improved in surface quality, compositional and luminescence homogeneity when compared with samples grown at equivalent temperature. The additional hydrogen did reduce the InN fraction slightly.

Investigations of the optical, compositional and structural properties of Ga auto-incorporated InAl(Ga)N epilayers are made. Composition measurements revealed 12–28 % of Ga incorporated. The growth parameters and resultant Ga indicated the likely cause is residual Ga coming from the reactor walls and delivery pipes, as by increasing the total flow rate from 8000 sccm to 24000 sccm was seen to suppress the GaN from 28 to 12 %. A broad spectral emission peak was seen, whose energy varied with InN content and not GaN.

A large set of InAlN epilayers grown on AlN buffers are studied. Composition measurements revealed a wide range of InN contents from 0.1 % to 25.6 %. The analysis revealed no presence of Ga within the samples. Optical measurements produced broad InAlN luminescence spectra which varied with InN content. The peak energy was found to be 3.46–3.93 eV for InN compositions of 0.7–6.6 %. Analysis suggests this is not bandedge emission due to the low peak energy and very wide FWHMs.

Finally, a home built PL mapping system is demonstrated, along with the design and operation challenges. Utilising this mapping system, investigations of InGaN/GaN MQW LED samples grown under different barrier growth methods are made.

Acknowledgements

I wish to give a huge thank you to everyone who has helped and supported me throughout the duration of my PhD. First I would like to thank my supervisor Prof. Rob Martin for giving me the opportunity to undertake this research project. I am forever grateful for his support, advice and extensive semiconductor knowledge. His confidence in me has kept me positive in the completion of this work.

Secondly, I would like to thank my second supervisor Prof. Kevin O'Donnell for his spectroscopy and semiconductor knowledge, and his help through some hard times. I am also grateful for the times we shared over a few whiskies.

A massive thanks goes to Dr. Paul Edwards for his guidance and training in using the EPMA, Quanta and his CHIMP program. His assistance and discussions with the set up of my PL mapping system were also invaluable. And not to forget the occasional office chats.

I would like to thank Dave Clark for his ability to fix almost anything, his help in providing components for the PL system, and his warm hearted and jovial nature which cheered me up even on the low days.

Another thanks goes to my collaborators Dr. Menno Kappers, Prof. Peter Parbrook, Dr. Vitaly Zubialevich, Matt Smith and Prof Katharina Lorenz for providing me with samples during my PhD, for their XRD and RBS measurements and also their fruitful discussions during my PhD.

A big thank you to my colleagues and friends Dr. Jochen Bruckbauer and Michael Wallace who were always there in need of crisis whether it was an equipment, computational or understanding problem, or just for some fun over a few pints. Thanks also goes to everyone else on level 2 for the great chats at lunch, and to Dr. Carol Trager-Cowan for her cakes and her Nemphlar related activities.

A further thank you to the University of Strathclyde and EPSRC for awarding

me with a DTA and providing the funding for my PhD.

On a more personal level I would like to thank all my friends and family for being there during my PhD, through the good times and hard times. A big thanks to my close friends Claire and Katie for always having an open ear and being there at short notice whether it be for a chat, a swim or some other random activity.

An extra special thanks goes to my mum Carol Anne, dad John, sister Lorna and gran Cathie for their ongoing support, encouragement and unconditional love throughout my studies. For this I will always be indebted. And finally I thank my husband, colleague, best friend and soul mate Martin who is always there for me. I will be forever in debt of his love, understanding and emotional support throughout these past years. It is to my husband and family that I thank for instilling confidence in me, and to them I dedicate this work.

Elaine Taylor-Shaw Glasgow, September 30, 2015

List of Publications

- **E. Taylor**, M. D. Smith, T. C. Sadler, K. Lorenz, H. N. Li, E. Alves, R. W. Martin, P. J. Parbrook, *"Structural and optical properties of Ga auto-incorporated InAlN epilayers"* - J. Cryst. Growth 408 (2014) 97101.
- M. D. Smith, **E. Taylor**, T. C. Sadler, V. Z. Zubialevich, K. Lorenz, H. N. Li, J. OConnell, E. Alves, R. W. Martin, P. J. Parbrook, *"Determination of Ga auto-incorporation in nominal InAlN epilayers grown by MOCVD"* - J. Mater. Chem. C, (2014), 2, 5787–5792.
- **E. Taylor**, F. Fang, F. Oehler, P. R. Edwards, M. J. Kappers, K. Lorenz, E. Alves, C. McAleese, C. J. Humphreys, R. W. Martin, *"Composition and luminescence studies of InGaN epilayers grown at different hydrogen flow rates"* - Semicond. Sci. Technol. 28 (2013) 065011.
- **E. Taylor**, P. R. Edwards, and R. W. Martin, *"Colorimetry and efficiency of white LEDs: Spectral width dependence"* - Phys. Stat. Sol. A, 14 (2012).

Contents

Abstract **iii**

Acknowledgements **v**

List of Publications **vii**

List of Abbreviations **xi**

1 Introduction **1**

1.1 History of LEDs 2
1.2 Applications 7
1.3 Thesis Objectives 8

2 Background **10**

2.1 Properties of III-Nitrides 10
2.1.1 Crystal Structure 10
2.1.2 Polarisation 13
2.1.3 Band Structure 15
2.2 Properties of Alloys 17
2.2.1 InGaN 17
2.2.2 InAlN 19
2.3 Optical Properties 20
2.3.1 Exciton Localisation 21
2.4 Growth of III-Nitride Structures 23
2.4.1 Challenges of Growth 23
2.4.2 Substrates 25
2.4.3 Epilayers and Quantum Wells 26

2.4.4 LEDs and HEMTs 29

3 Growth and Experimental Techniques 31

3.1 Introduction 31

3.2 Growth 31

3.3 Scanning Electron Microscopes 34

3.4 Structural and Composition Characterisation Techniques 39

3.4.1 Wavelength Dispersive X-ray Spectroscopy 39

3.4.2 Rutherford Backscattering Spectrometry, X-ray Diffraction and Atomic Force Microscopy 45

3.5 Optical Characterisation Techniques 51

3.5.1 Cathodoluminescence 52

3.5.2 Photoluminescence 57

4 Composition and Luminescence Studies of InGaN epilayers 61

4.1 Introduction 61

4.2 Sample and Experimental Details 62

4.3 Surface Quality 64

4.4 Compositional Characterisation 67

4.5 Optical Characterisation 73

4.6 Summary 77

5 Composition and Luminescence Studies of InAl(Ga)N Epilayers 79

5.1 Introduction 79

5.2 Sample and Experimental Details 80

5.3 Sample Quality 82

5.4 Compositional and Structural Characterisation 86

5.5 Optical Characterisation 93

5.6 Summary 95

6 Composition and Luminescence Studies of InAlN/AlN Epilayers 97

6.1 Introduction 97

6.2 Sample and Experimental Details 98

6.3 Sample Quality 100

6.4 Compositional Characterisation 103

6.5 Optical Characterisation 110
6.6 Summary 114

7 Luminescence Studies of InGaN Through Photoluminescence Mapping 115

7.1 Introduction 115
7.2 Photoluminescence Mapping System 116
7.2.1 Design and Set Up 116
7.2.2 Operation of Nanopositioners 117
7.3 Initial Measurements 118
7.3.1 Spot Size Measurement 119
7.3.2 RT Maps 121
7.3.3 LT Maps 122
7.4 InGaN/GaN LED Structure Samples 124
7.4.1 Sample and Experimental Details 124
7.4.2 Photoluminescence Characterisation 126
7.5 Summary and Further Developments 134

8 Summary and Future Work 135

8.1 Overall Summary 135
8.2 Future Work 138

References 140

Conference Contributions 161

List of Abbreviations

2DEG	2-dimensional electron gas
AFM	Atomic force microscope
AlGaN	Aluminium gallium nitride
AlN	Aluminium nitride
BE	Bound exciton
BSE	Backscattered electron
CB	Conduction band
CCD	Charge-coupled device
CCT	Correlated colour temperature
CHIMP	Cathodoluminescence hyperspectral imaging and manipulation program
CL	Cathodoluminescence
CRI	Colour rendering index
e-h	electron-hole
EDX	Energy dispersive x-ray
EPMA	Electron probe microanalyser
EQE	External quantum efficiency
ESEM	Environmental scanning electron microscope
FE	Free exciton
FEGSEM	Field emission gun scanning electron microscope
FWHM	Full width half maximum
GaAs	Gallium arsenide
GaN	Gallium nitride
HEMT	High electron mobility transistor
HVPE	Halide vapour phase epitaxy
InAlN	Indium aluminium nitride

InGaN	Indium gallium nitride
InN	Indium nitride
IQE	Internal quantum efficiency
LD	Laser diode
LDD	Low dislocation density
LED	Light emitting diode
LEEBI	Low energy electron beam irradiation
LM	Lattice matched
LPE	Liquid phase epitaxy
MBE	Molecular beam epitaxy
MOCVD	Metalorganic chemical vapour deposition
MOVPE	Metalorganic vapour phase epitaxy
MQW	Multi-quantum well
NDF	"Nuno's" data furnace
NH_3	Ammonia
PL	Photoluminescence
PLE	Photoluminescence excitation
QCSE	Quantum confined stark effect
QE	Quantum efficiency
QW	Quantum well
RBS	Rutherford backscattering spectrometry
RSM	Reciprocal space map
SE	Secondary electron
SEM	Scanning electron microscope
SiC	Silicon carbide
SSL	Solid state lighting
TMAl	Trimethylaluminum
TMGa	Trimethylgallium
TMIn	Trimethylindium
UV	Ultra-violet
VB	Valence band
WDX	Wavelength dispersive x-ray
XRD	X-ray diffraction
YAG	Yttrium aluminium garnet

Chapter 1

Introduction

Solid state lighting (SSL) devices have come a long way in the last 20 years with the emergence of highly efficient nitride based blue light emitting diodes (LEDs) and laser diodes (LDs). The invention of the blue LED has been recognised as a great achievement worldwide with the inventors Shuji Nakamura, Isamu Akasaki and Hiroshi Amano having been awarded the recent 2014 Nobel prize in physics [1]. The continued research on III-nitride materials is important for the further development of commercial and domestic solid state lighting, and to extend to new wavelengths. Approximately 20 % of the electricity generated globally is used for lighting, and with a limited supply of fossil fuels more efficient light sources (in conjunction with renewable energy) is needed to reduce energy consumption, costs and pollution [2, 3]. This drove the European Union (EU) to ban the inefficient 100W incandescent bulb (∼5 %) in 2009, with the 60W, 40W and 25W also now prohibited for sale across Europe [4]. This has increased the demand for alternative high efficiency lighting such as LEDs [5].

White LED bulbs based on the blue nitride LED are now emerging on to the market place as an alternative to the conventional incandescent bulb. These offer high energy savings due to their increased efficiency compared to the available incandescent lamps. Although expensive, they are now a contender to halogen (∼15-45 % increased efficiency) and compact fluorescent (∼65-80 % increased efficiency) lighting with their high efficiencies (>70 % increased efficiency), long lifetimes ($> 10^5$ hours) and low toxicity (no Hg) [4]. The EU have stated that by 2020 all lighting with <70 % efficiency will be phased out. Progress within

LED research has pushed the efficiency up to 70 % but several factors still need to be resolved in order to fully replace fluorescent strip lighting. This can only be achieved if LEDs produce efficiencies >80 %. The main issues that need to be overcome to obtain these higher efficiencies are efficiency droop, the 'green gap' and cost. These will be discussed further in the subsequent chapter.

When dealing with optoelectronic devices for lighting purposes, such as LEDs, it is more appropriate to look at the bulbs overall output efficiency in terms of luminous efficacy (measured in lumens per Watt). This preferred measurement of lighting efficiency takes into account the human eye's spectral sensitivity - which peaks in the green at 555 nm [6]. This is important when engineering a device as by altering the spectral output it can improve the overall efficacy [7]. However care has to be taken as small variations in shades of white light can be easily perceived as projected by the colour rendering index (CRI) [8]. This results in a trade off occurring with CRI and luminous efficacy [9, 10]. With improvements in semiconductor research and light engineering the commercially available white LEDs have luminous efficacies now exceeding 150 lm/W.

As well as the development of LEDs within the visible region of the III-nitride system for SSL, research into ultra-violet (UV) based LEDs has gained great interest over recent years with UV-LEDs now commercially available [11]. The replacement of UV fluorescent lamps plus many more applications such as water purification (see section 1.2) has driven research in both academia and industry to achieve high efficiency UV-LEDs. The III-nitrides are the leading material system for UV lighting with the ability to produce emission into the deep-UV region (200-300 nm).

This chapter will give an overview on the history of LED research and the development of the III-nitride based blue, UV and white LED. The current and potential applications of these LEDs will also be summarised. And finally the objectives and structure of this thesis will be outlined.

1.1 History of LEDs

The first "LED" was found accidentally in 1907 by Henry Joseph Round when he saw the emission of light from a small silicon carbide (SiC) crystallite used as sandpaper abrasive. Round applied a small voltage at room temperature

across a SiC crystal and noticed a yellowish light being emitted near the metal contact [12, 13]. The first evidence of electroluminescence was observed. He reported his findings in Electrical World journal and LED research had begun [14]. In 1927 a Russian named Oleg Lossev reported on the luminescence and current-voltage (I-V) characteristics of a SiC diode and had deduced that the luminescence was not due to incandescence but rather similar to cold electronic discharge [13, 15]. This was the invention of the now known LED. By the 1960s a SiC blue LED was in production but the efficiency of this LED was very low due to the indirect bandgap. The efficiency did not improve so the focus turned to III-V semiconductors.

The first compound investigated was GaAs in the early 1950s aided by the development of the liquid-phase epitaxy (LPE) growth technique. By 1962 GaAs infrared p-n junction LEDs and lasers were produced by several groups [12]. The next goal was to produce visible emission adopting the same p-n junction diode. Holonyak et al achieved red luminescence in 1962 after using GaAsP which was grown with a bandgap in the red region of the visible spectrum [16]. This led to the emergence of commercially available visible LEDs with the first applications as indicator lights on circuit boards. Work continued through the 1970s and 1980s on other alloys such as AlGaAs, GaAsP:N and GaP:N, which resulted in red, orange, yellow and green emission. The efficiency improved as research developed for the red, orange and yellow based LEDs. This is illustrated in the performance timeline in Figure 1.1, which displays the evolution of LED luminous efficacy up to 2008.

As the red, orange and yellow LED efficiencies improved through the 60s, 70s and 80s, emission in the blue part of the visible spectrum was not as successful. Achieving efficient blue emission would allow the development of full colour displays (including flat panel colour televisions) by replacing the cathode ray tubes with LEDs, as red, green and blue pixels are required to produce a full colour image. Unfortunately producing materials with blue emission had proven difficult. Research started in the late 1960s on III-nitride materials with main emphasis on GaN. The first complication that arrived was in the growth of this material as it was hard to find substrates that matched the lattice structure. Eventually hetero-epitaxial growth was used whereby the GaN was grown on top of a sapphire substrate using a halide vapour phase epitaxy (HVPE) technique [18].

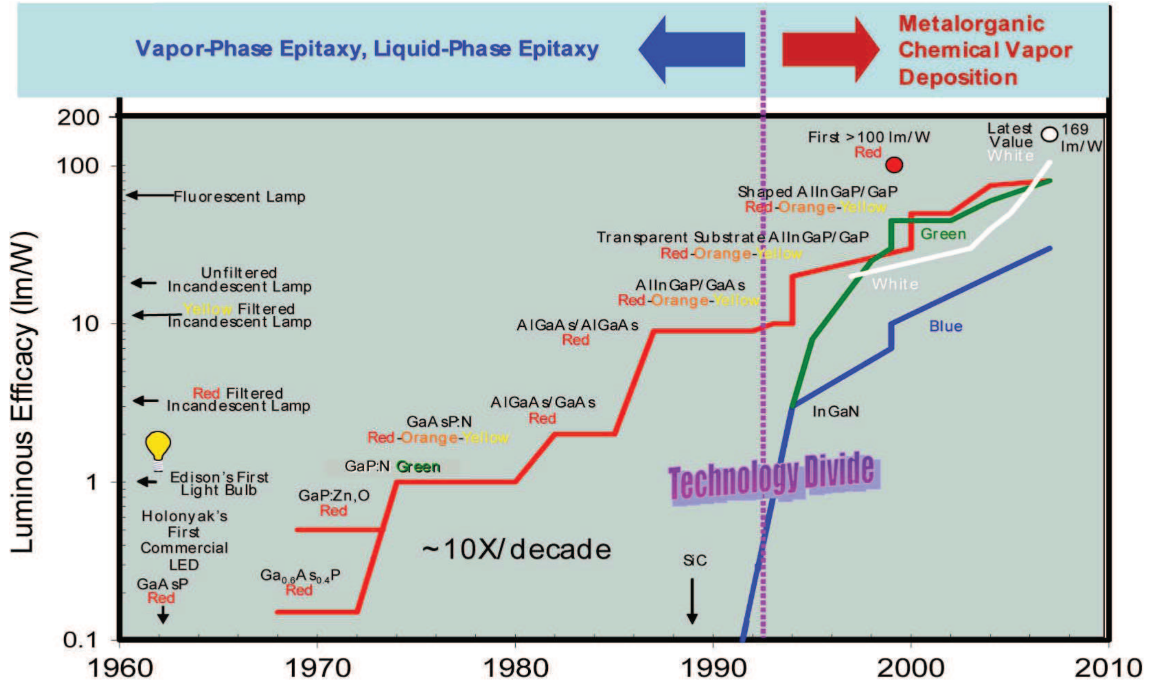

Figure 1.1: LED performance timeline with efficiency defined as luminous efficacy (lm/W). *Image taken from [17].*

This mismatch of substrate led to poor structural quality of the GaN layers. The other complication that became apparent was that the GaN was predominately n-type, so difficulty arose in doping the films p-type. The p-type doping was an important complication to overcome as it was required in producing the p-n junction diode. Pankove and Maruska developed Mg-doped GaN films using the HVPE technique while at RCA in 1972 [19]. This resulted in violet emission at 430 nm but the device was very inefficient (<0.01 %). RCA collapsed in 1974 and the project was cancelled, so interest diminished. Only a handful of researchers pursued the p-doping dilemma, one of which was Akasaki.

The problem was not overcome until the late 1980s by Akasaki and Amano, and indepently by Nakamura, when the development of a new two-flow metal organic chemical vapour deposition (MOCVD) reactor was introduced [20, 21, 22]. This improved crystal growth and allowed high quality GaN layers to be produced with low temperature AlN and GaN buffer layers between the sapphire substrate and the active GaN [23, 24]. By growing the buffers at a lower temperature, and controlling the temperatures and flow rates during the growth, the background

n-type doping levels were also reduced. This eventually led to the breakthrough in p-type doping using Mg as a dopant. Amano and Akasaki, based at Nagoya University, were the first to achieve p-type doping through low energy electron beam irradiation (LEEBI) in 1989 using Mg-doped GaN. The LEEBI treatment reduced the resistivity of the Mg-doped GaN and improved the photoluminescence efficiency [25, 26]. In 1991, while working for Nichia Chemical Company, Nakamura developed a more practical method for increasing the p-type conductivity of a Mg-doped GaN film through a thermal annealing process implemented at the end of growth under nitrogen atmosphere [27, 28]. The resistivity was reduced and hole carrier concentration increased further in comparison to Amano and Akasaki's LEEBI method. Following this Nakamura produced high efficiency homo-junction GaN LEDs that had an active InGaN layer which allowed the emission of blue light of wavelength 440nm [29]. The resultant InGaN blue LEDs were ten times more powerful and had ten times the external quantum efficiencies of the SiC blue LEDs at the time. These InGaN material systems were also able to produce high efficiency green LEDs that had much higher efficiencies than the GaP based green LEDs by altering the ratio of InN to GaN in the $In_xGa_{1-x}N$ active layer [30]. By 1993 Nichia had managed to commercialise these LEDs and the applications for them grew. These discoveries leading to the invention of the blue LED have been recognised as a great achievement worldwide with Nakamura, Akasaki and Amano being awarded the recent 2014 Nobel prize in physics.

After the discovery of high efficiency blue LEDs, it was not long until white LEDs were produced (see Figure 1.1). These blue LEDs are the basis for the white LED. The most common method used in solid state lighting is the blue LED coated in a yellow emitting phosphor. The InGaN blue LEDs are used in conjunction with a cerium doped yttrium aluminium garnet (Ce^{3+}:YAG) phosphor as the Ce^{3+}:YAG has high absorption in the blue allowing the emission from the blue LED to excite the phosphor which emits yellow fluorescence. The mixture of the blue light from the LED and the yellow from the YAG phosphor produces white light. The emission wavelength of the phosphor and blue LED can be varied by altering their compositions allowing a range of white colours to be achieved [12, 20]. Another method to achieve white light is using a combination of three primary coloured LEDs such as AlInGaP for red, and InGaN for green and blue to produce white light. This method requires varied supply currents in

order to control the intensity of each LED and is more expensive than using a single LED. Therefore the RGB method is most suitable to large displays where several millions of these primary LEDs are used to give the effect of white light. A third way to achieve white light is by using a UV LED to pump a mixture of coloured phosphors like blue, green, yellow, red. This has the advantage that it gives greater control over colour rendering but is less efficient than the blue LED and yellow phosphor design [31].

Following the developments of the crystal growth and conductivity control of the III-nitride materials GaN and InGaN, there has been increasing interest in the growth of AlGaN, AlGaInN and more recently InAlN for use as UV and deep-UV emitters (and high power electronic devices). The incorporation of AlN within these alloys allows much lower emission wavelengths (down to $\sim$210 nm) to be accessed. This makes the III-nitrides the leading material for applications in this UV region as no other material system can compete at these low wavelengths. Difficulty arose in achieving good crystalline quality with high AlN fractions due to the large lattice mismatch between the AlGaN and, GaN and sapphire substrates. This resulted in poor quality material with cracking and high dislocation densities [32, 22]. Due to these imperfections the first AlGaN UV LED to produce emission below the GaN band edge (365 nm) was very inefficient (< 1 %) [33]. Many improvements have been made towards UV LEDs by adopting various growth procedures and structures which have allowed lower wavelengths to be achieved. Many UV LEDs are now commercially available with varying wavelengths, however research is still ongoing to obtain higher efficiencies [34]. As mentioned above InAlN is another material which has the potential to produce UV LEDs but is the least studied out of the III-nitride alloys. Like AlGaN the challenge lies with producing high quality layers but has the advantage that it can be lattice matched to GaN (more on this in Chapter 2) [35, 36]. Research is progressing with InAlN UV LEDs but more applications for this material have emerged, some of which are stated in the subsequent section [37, 38].

1.2 Applications

http://ledlight.osram-os.com/applications/street-led-lighting/

https://www.any-lamp.com/blog/philips-bridge-project

http://www.traffictechnologytoday.com/news.php?NewsID=15136

http://www.brightbikelights.com/dual-led-frog-light-pair

http://www.m25audi.co.uk/audi/a6/new-audi-a6-led-headlights.html

Figure 1.2: Examples of LED applications including street, traffic, bike and car lights.

The applications of LEDs from the UV to the visible and into the infrared parts of the electromagnetic spectrum are growing and becoming more apparent in everyday life - not just in solid state lighting (SSL). This is due to the high luminous efficacies, long lifetimes, fast switching times, lower consumable power and compact size. Some well known examples are shown in Figure 1.2. These include; traffic lights, car and bike lighting, artistic lighting, street lighting, large building displays, and emergency lighting. The LEDs in these applications have replaced the less efficient and lower lifetime incandescent, fluorescent and halogen light bulbs, resulting in energy saving, lower maintenance costs and a reduction in toxicity.

In addition to LEDs being used for general lighting purposes other uses have emerged due to their considerably smaller size and faster switching times such as; standby lights on televisions, backlights of large LCD televisions, computer monitors, remote controls, indicator lights and mobile phones. Also the devel-

opment of the III-nitride blue-UV laser diode (LD) has improved optical storage capabilities leading to the invention of the Blu-ray disc player [39].

The III-nitrides AlN, GaN, InN and their alloys have many more applications not just as optoelectronic devices. These include; heterojunction field effect transistors (HFETs) and high electron mobility transistors (HEMTs) for high power devices, photovoltaics, water purification, distributed Bragg reflectors (DBRs) and microcavities, chemical sensors, and uses in communications technology [40, 41, 42, 43, 44, 45, 46, 47].

1.3 Thesis Objectives

This thesis presents investigations of the compositional, structural and luminescence properties of III-nitride alloys InGaN, InAlN and InAl(Ga)N, with preliminary work on applying a photoluminescence (PL) mapping technique also given. Research into the relationships between these material properties, and also the growth procedures is of great interest as they are still not fully understood. In this work the main technique used for measuring the composition is wavelength dispersive x-ray (WDX) and the optical properties are studied mainly through cathodoluminescence (CL) spectroscopy measurements.

Following this introduction chapter the thesis is divided into a further 7 chapters, with Chapters 2 and 3 providing the background to the work presented. Chapter 2 gives information on the properties of III-nitrides and their alloys, and Chapter 3 presents details of the experimental methods used throughout the thesis, including those performed by collaborators. Chapters 4-7 are the experimental results chapters. In Chapter 4 the composition and luminescence properties of a set of InGaN epilayers are presented and the effect of varying hydrogen carrier gas flow during growth is discussed. The composition and luminescence properties of InAlN samples with unintentional Ga incorporation are given in Chapter 5. The effects of the Ga auto-incorporation on the material properties are discussed and a potential cause of this is suggested. Chapter 6 looks at InAlN epilayers with an aim to diminish Ga auto-incorporation, and the compositional, structural and optical properties are presented. Finally the last of the results chapters, Chapter 7, gives information on the development of a PL mapping system and the challenges faced, with initial measurements on InGaN/GaN MQW

LED samples also presented. Chapter 8 provides a summary of the main results of this thesis along with suggestions of future work.

Chapter 2

Background

This chapter provides background information on the properties of binary and ternary III-nitride semiconductors, including details concerning their crystal structure, band structure, optical properties and growth. The properties and background of the ternary alloys InGaN and InAlN, studied in this thesis, are also given.

2.1 Properties of III-Nitrides

This section provides information on the properties of the binary III-nitrides AlN, GaN and InN. It includes details on their crystal structure (mainly wurtzite), polarisation effects, electronic band structure and optical properties. Also highlights of the effects of combining the binaries into ternary alloys (InGaN and InAlN) are given.

2.1.1 Crystal Structure

The crystal structure of the III-nitrides have two common forms; the hexagonal wurtzite structure and the cubic zincblende structure. The wurtzite structure is most thermodynamically stable at room temperature for GaN, AlN and InN, and therefore is the structure of choice when used for devices. This is illustrated in Figure 2.1(a). There is also the lesser known rock salt structure which can be obtained at very high pressures [48]. The wurtzite and zincblende structures are similar as in both cases the bonding of the nearest neighbour is tetrahedral,

with each of the group III atoms having four adjoining nitrogen and vice versa. The difference between these structures is their Bravais lattice and their stacking sequence [20]. The stacking of the layers of atoms along the c-axis for the wurtzite structure of GaN is of the form ABABAB:

$$...Ga_AN_AGa_BN_BGa_AN_AGa_BN_BGa_AN_AGa_BN_B...$$

whereas the cubic zincblende stacking sequence is ABCABC:

$$...Ga_AN_AGa_BN_BGa_CN_CGa_AN_AGa_BN_BGa_CN_C...$$

Figure 2.1(b) shows the unit cell of the wurtzite structure of GaN with the a-axis and c-axis indicated. The length and height of the unit cell, and therefore the hexagon, are defined as the a and c lattice constants. The wurtzite bilayer structure consists of two hexagonal close packed (HCP) sublattices of group III and N atoms, offset along the c-axis by $\frac{5}{8}$c [48]. This is the ideal (unstrained) case and can be observed in Figure 2.1(b). The compounds AlN and InN have the same form, with the Ga atoms substituted for Al and In in each case. The lattice constants differ for each binary compound due to the size of the atomic radii of the group III elements and bonding energy of the III-N binaries (see Table 2.1). All the samples studied in this thesis are in the wurtzite grown in the c-direction [0001], which is the standard growth for III-nitride materials.

Many factors can alter the ideal crystal structure and lattice constants for each of the III-nitride compounds such as growth conditions, defects, doping concentrations, temperature, composition and choice of substrate. The lattice constants and ideal (unstrained) c/a ratio of the wurtzite III-N binaries used throughout this thesis are presented in Table 2.1. The lattice parameters for alloys

Material	a_0 (Å)	c_0 (Å)	c/a ratio	E_b (eV)	E_g (eV)	Δ_{cr} (meV)
AlN	3.112	4.982	1.601	2.88	6.2	-217
GaN	3.189	5.185	1.626	2.2	3.4	42
InN	3.548	5.76	1.623	1.93	≈0.7	41

Table 2.1: Properties of wurtzite AlN, GaN and InN at RT including; a_0 and c_0 lattice constants, ideal c/a ratios, bonding energies (E_b), bandgap (E_g) energy and crystal field splitting energy (Δ_{cr}). Values taken from [48, 20, 49, 50, 51].

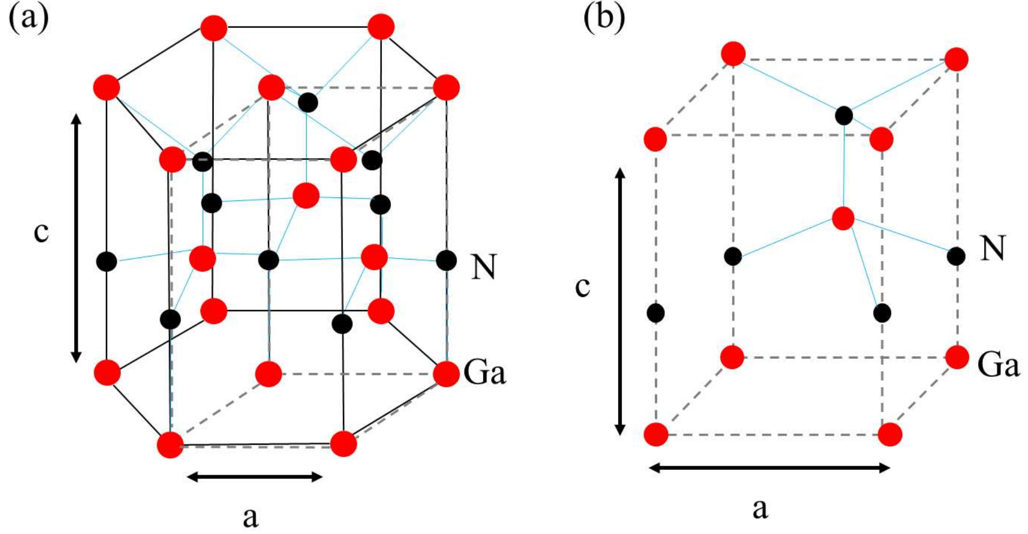

Figure 2.1: (a) Wurtzite structure of GaN with Ga atoms in red and N atoms in black. (b) The unit cell of wurtzite GaN highlighting the *ABAB* stacking sequence.

containing AlN, GaN and InN exhibit a linear relationship with composition at a constant temperature as described by Vegard's law presented in Equations 2.1-2.4 [52, 53]. A ternary alloy made up of two III-N binaries defined as AN and BN, and a quaternary with a third binary CN, have the following lattice parameter relationships:

$$a_{A_xB_{1-x}N} = xa_{0_{AN}} + (1-x)a_{0_{BN}} \tag{2.1}$$

$$c_{A_xB_{1-x}N} = xc_{0_{AN}} + (1-x)c_{0_{BN}} \tag{2.2}$$

$$a_{A_xB_{1-x}C_{1-x-y}N} = xa_{0_{AN}} + ya_{0_{BN}} + (1-x-y)a_{0_{CN}} \tag{2.3}$$

$$c_{A_xB_{1-x}C_{1-x-y}N} = xc_{0_{AN}} + yc_{0_{BN}} + (1-x-y)c_{0_{CN}} \tag{2.4}$$

where x, y, $x-1$ and $1-x-y$ are the compositional fractions of each of the binary compounds within the alloy, and a_0 and c_0 are the lattice constants of each of the corresponding binaries [54, 55]. For example $In_xGa_{x-1}N$ with $x = 0.25$ would have lattice paramters $a = 3.279$ Å and $c = 5.329$ Å using the values given in Table 2.1. Although this rule generally applies there is dispute as to the validity of Vegard's law for InAlN alloys [56, 35]. This is due to the large differences in

ionicity and ionic sizes between the binaries InN and AlN. The deviations from Vegard's law are suggested to be strain driven, with larger deviations occurring the further away from the lattice matched (LM) point of GaN (when InAlN is grown on GaN) [56].

2.1.2 Polarisation

Due to the lack of inversion symmetry in wurtzite III-nitrides the materials possess strong polarisation effects when grown along the c-direction, with other growth directions having less or no polarisation effects [57]. Depending on the orientation of the bilayer the crystal can be either Ga-polar (also In-polar and Al-polar) [0001] or N-polar [$000\bar{1}$], where the surface is metal faced or N faced, respectively. The [0001] and [$000\bar{1}$] represent the direction of polarity from a group III atom to the nearest neighbour N atom. This is illustrated for GaN in Figure 2.2(a) and 2.2(b). The wurtzite structure exhibits spontaneous polarisation ($\mathbf{P}_{SP}$) due to deviations from the ideal crystal structure which is associated with these polarities. This is caused by variations in ionicity across the 4 tetrahedral bonds [58], as shown in Figure 2.2(c). The Ga-polar and N-polar give the direction of the spontaneous polarisation for GaN, with the net ($\mathbf{P}_{SP}$) pointing into the bulk material for Ga-polar and towards the surface for N-polar. This is also the case for the other III-nitrides which exhibit different ($\mathbf{P}_{SP}$) values, increasing from GaN to InN to AlN, and all negative.

The III-nitrides also exhibit piezoelectric polarisation ($\mathbf{P}_{PE}$). This is induced by mechanical strain caused by lattice mismatch from growing on alternative substrates or MQW heterostructures along the c-axis (see section 2.4 for more on lattice mismatch and strain). The $\mathbf{P}_{PE}$ is linearly related to the in-plane strain, therefore when the material is under tensile strain $\mathbf{P}_{PE}$ is negative, and when compressively strained $\mathbf{P}_{PE}$ is positive [59]. The total polarisation has influence on the band structure due to the large in-built electric field (10x larger than other III-V and II-VI compounds), which in-turn affects the optical properties [57]. It also has influence on single and multi-quantum well (SQW and MQW) structures due to effects such as the quantum confined Stark effect (QCSE) (see section 2.4.3). This is important to consider when making optoelectronic devices. A method for getting round this issue is to grow semi or non-polar materials

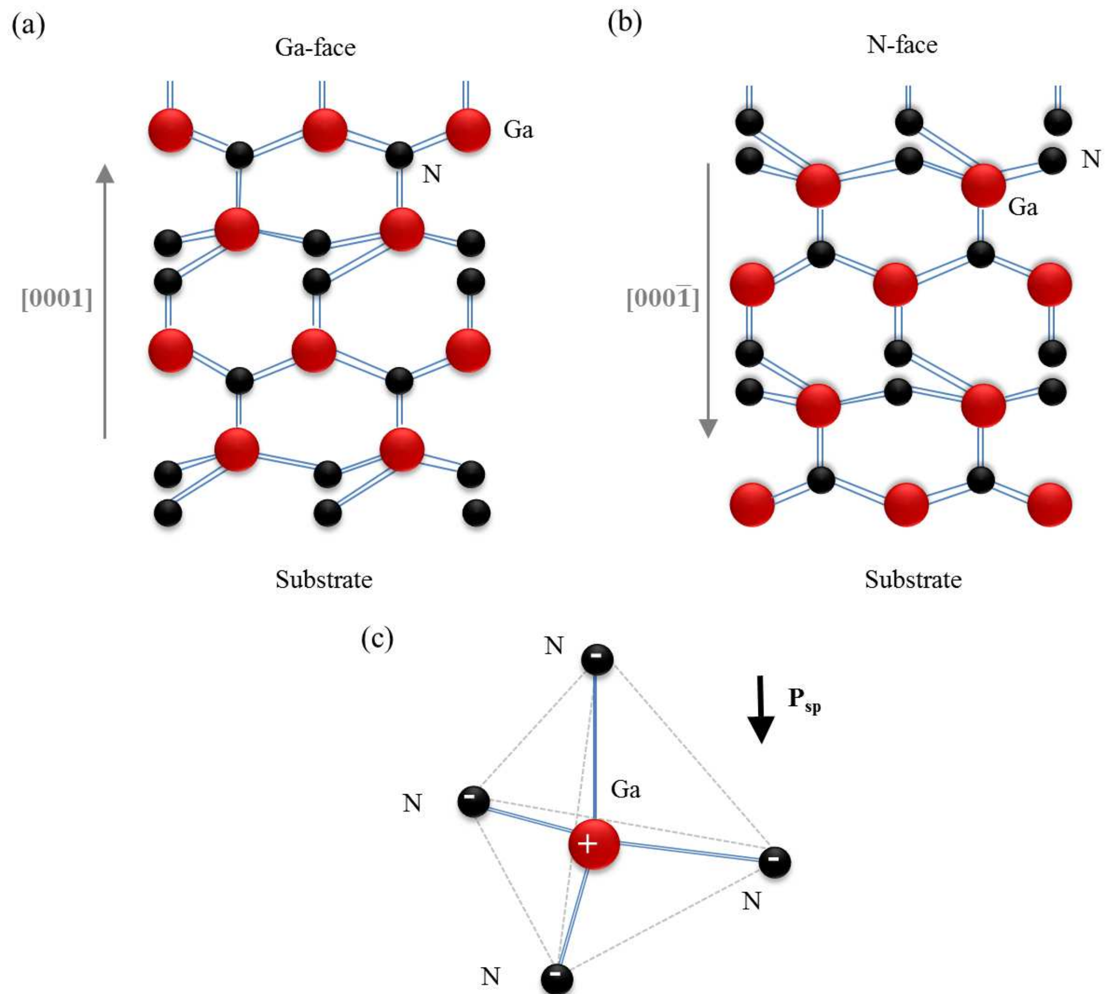

Figure 2.2: (a) Ga polar and (b) N polar showing orientation of Ga and N atoms. *Image adapted from [57].* (c) Tetrahedral bonding of GaN illustrating the net ionicity and direction of spontaneous polarisation ($\mathbf{P}_{SP}$).

which is achieved by growing on other planes such as a-plane and m-plane where there are reduced or no unbalanced electric fields, respectively. These types of materials are not studied here.

2.1.3 Band Structure

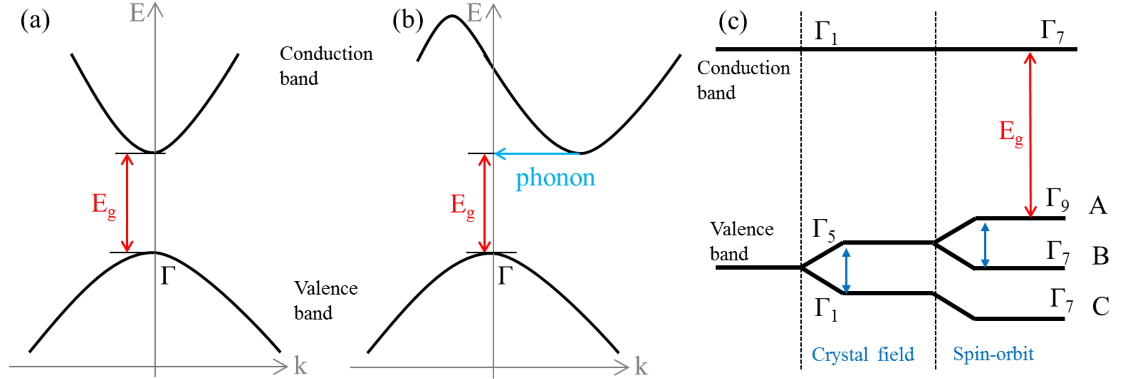

Figure 2.3: Energy band diagram showing direct (a) and indirect (b) bandgap semiconductors of energy vs. momentum k. (c) Schematic of the separation of the valence band due to crystal field splitting and spin-orbit coupling. Example given is of positive crystal field energy splitting as for wurtzite GaN and InN.

A fundamental property of the III-nitrides that is important for their use as light emitters is the band structure. AlN, GaN and InN all exhibit a direct bandgap allowing efficient light emission unlike SiC which is inefficient and indirect. For a direct bandgap the conduction band minima and valence band maxima occur at the same crystal momentum k value ($k = 0$, Γ-point), allowing direct transitions between the bands. The indirect bandgap has different k values for the conduction band minima and valence band maxima which requires phonon assisted transitions between the bands. This reduces the probability of radiative recombination resulting in low emission efficiency (more details given in section 2.3). Simple schematics of direct and indirect bandgaps are given in Figures 2.3 (a) and 2.3 (b).

For the hexagonal wurtzite III-nitrides the valence band is split into three separate bands due to crystal field splitting and spin orbit interactions as shown in Figure 2.3 (c) [49]. This is due to the crystal symmetry and relatively weak spin-orbit interactions. The holes associated with each of these bands A (Γ_9), B (Γ_7) and C (Γ_7) are known as heavy holes (HH), light holes (LH) and crystal field (CH), respectively. For GaN and InN the crystal field splitting energy (Δ_{cr}) is

small and positive whereas for AlN it is larger and negative, (values given in Table 2.1) [20]. This results in a difference in the ordering of the valence bands. For zincblende structures the crystal field splitting is very small, and the spin-orbit dominates.

Each ternary and quaternary wurtzite III-N semiconductor has a direct bandgap value (see Table 2.1) which can be tuned by alloying different fractions of the III-N binaries. This results in bandgaps covering the UV, visible and infrared regions of the electromagnetic spectrum. The compositional dependence of the bandgap for ternary alloys can be described by the standard quadratic bowing equation:

$$E_{g(A_xB_{1-x}N)} = xE_{g(AN)} + (1-x)E_{g(BN)} + bx(1-x) \tag{2.5}$$

where x is the composition, E_g are the bandgaps of the binary compounds and b is the bowing parameter. For InGaN the bowing parameter is reported to be 1.43 eV and for InAlN it is 3.0 eV, however recent publications suggest that b has a compositional dependence for InAlN [60, 61]. This is illustrated in Figure 2.4 for bandgap against a lattice constant, showing the bowing nature of the gap for each of the alloys schematically. The bandgap values of the binary nitrides at room temperature, as shown in Figure 2.4, are 6.2 eV for AlN, 3.4 eV for GaN and 0.7 eV for InN [51, 57]. Note the recently reviewed InN bandgap value (as of 2002) is given, with the previously accepted value being around 1.9 eV [62]. For quaternary alloys the composition dependence is more complex with 3 bandgaps for each of the binary compounds and 3 composition dependent bowing parameters for each of the possible ternary alloys [63].

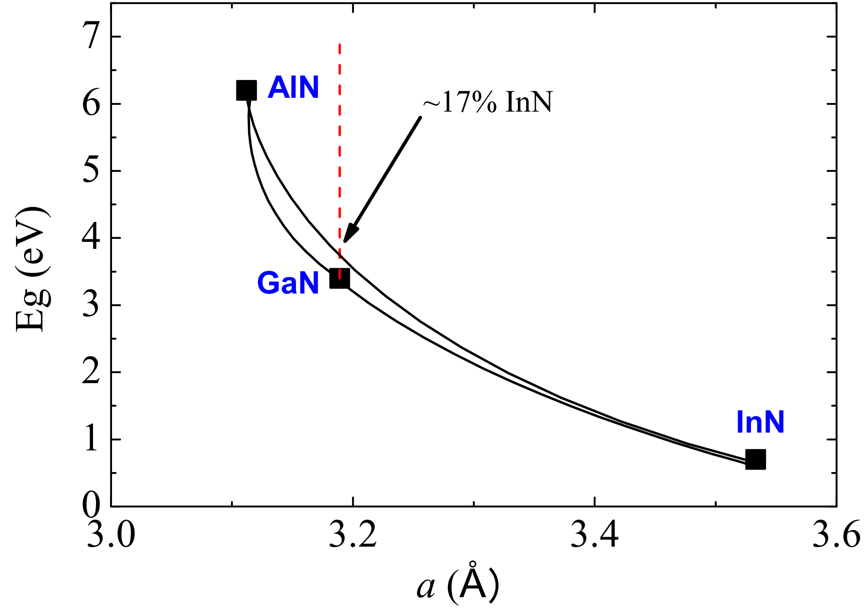

Figure 2.4: Interpretation of the bandgap bowing of the ternary III-nitrides for variations in a lattice constant shown schematically by lines between the compounds. Bandgaps of AlN, GaN and InN shown spanning the UV, visible, and infrared. Also lattice match point of InAlN on GaN indicated with ~17 % InN fraction.

2.2 Properties of Alloys

This section highlights the properties associated with alloying different III-nitride compounds, with specific focus on the composition and optical properties of the alloys InGaN and InAlN.

2.2.1 InGaN

$In_xGa_{1-x}N$, henceforth referred to as InGaN, is the most studied of the III-nitride alloys. It is used as the active region (i.e in the QWs) of the current commercially available blue, green and white LEDs. As shown in Figure 2.4 an InGaN alloy can span the UV, visible and infrared regions of the electromagnetic spectrum however achieving this has proven to be challenging. The increase in InN fraction within the alloy leads to reduced external quantum efficiency (EQE) which drops significantly when x exceeds 0.25 (i.e below ~2.6 eV / above ~480 nm). This is

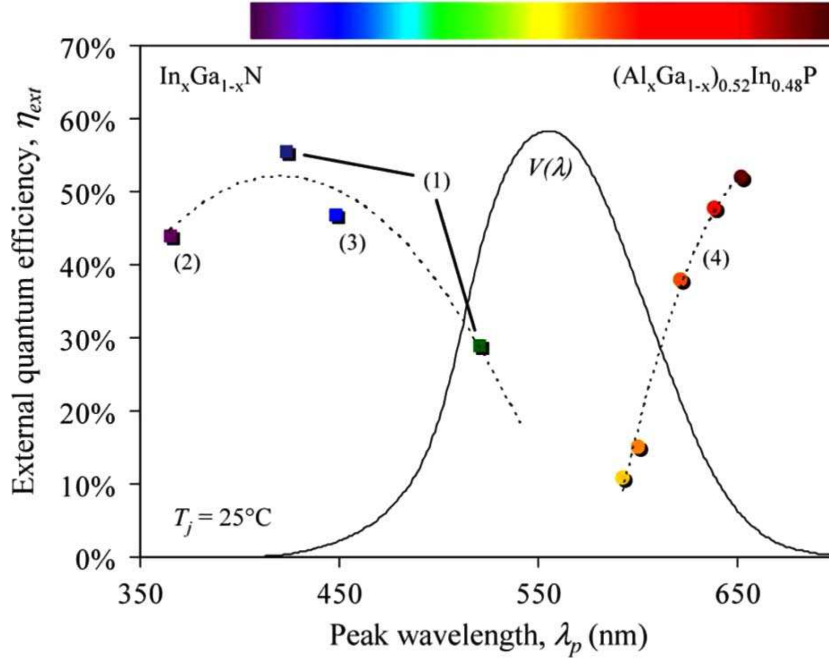

Figure 2.5: Depicting the 'green gap' with the reduction in external quantum efficiency (EQE) shown for increasing and decreasing wavelength of the InGaN and AlGaInP alloys, respectively. The eye's response curve ($V(\lambda)$) is also shown illustrating that it peaks in the green at 550 nm. *Taken from [65].*

the III-nitride side contribution to the 'green gap' problem [64]. Phosphide based materials such as GaAsP, which are used for red and orange light emission, show a similar drop in efficiency when trying to achieve higher emission energies. This is illustrated in Figure 2.5.

The reason for the reduction in efficiency with increasing InN fraction in InGaN is not yet fully understood, although research is ongoing to understand and combat this problem. Growing good quality InGaN with high InN is difficult due to the increase in defects and non-uniformity as x increases. This affects the power performance of the LED. Another proposed cause is an increase in the quantum confined Stark effect (QCSE) due to the creation of deeper quantum wells (QWs) (see section 2.4.3 for more detail on QCSE). The increase in InN fraction decreases the emission energy but incurs an increase in the piezoelectric fields, which further spatially separates the electron and hole wave functions reducing the probability of radiative recombination. A further contributory cause

could be the 'efficiency droop' related to the internal quantum efficiency (IQE). This droop is associated with the increase in excitation whereby with increasing injection current a reduction in intensity occurs [64, 66]. Many arguments have been made to the origin of this drooping at high powers, such as Auger effects, carrier delocalisation, screening of excitons, but the issue has yet been fully resolved. Research into overcoming the green gap issue and pushing the InGaN alloy to longer wavelengths will open new avenues for applications such as improved solid sate lighting (SSL), photovoltaics and chemical sensors [46].

2.2.2 InAlN

$In_xAl_{1-x}N$, henceforth referred to as InAlN, is a lesser studied ternary alloy of the III-nitride group. It has gained more interest in the last decade or so due to the realisation of the potential applications in high power and optoelectronic devices such as DBRs, HEMTs, etc (see section 1.2). This is fuelled by the fact it covers the largest energy range of the III-nitride ternaries and has the ability to be lattice matched (LM) to c-plane GaN with an InN content of $\sim$17 % (shown in Figure 2.4). Achieving InAlN LM to GaN allows reduction (elimination) of mismatch strain and piezoelectric fields, unlike the other ternaries AlGaN and InGaN. However difficulty arises in the growth of the alloy due to the large difference in covalent bonds of the constituent binaries InN and AlN (more details on growth challenges in section 2.4.1) [35, 45].

As research on InAlN has increased more attention has focused on the electrical properties of the alloy and less is known about the optical properties, especially in comparison to AlGaN and InGaN. Understanding these properties will lead to further developments in optoelectronic devices. One main investigation still under discussion is the compositional dependence on the bandgap. Even from early reports, with the previously accepted InN bandgap value, a large InAlN bowing parameter was evident for a range of different compositions which indicates a strong bowing of the bandgap with composition [67, 68]. More recent investigations by Schulz et al have suggested a compositional dependent bowing parameter for InAlN whereby the bowing parameter value changes with changing composition [60]. The optical properties of a set of InAlN epilayers covering a large range of compositions are investigated in this thesis.

2.3 Optical Properties

When an electron is excited from the valence band (VB) to the conduction band (CB) through mechanisms such as electrical excitation, electron beam excitation or photoexcitation it leaves behind a hole. The electron relaxes to the lowest energy state emitting phonons and the semiconductor undergoes various radiative and non-radiative recombination processes. The electron-hole (e-h) radiative recombination processes are summarized in Figure 2.6. Improving the ratio of radiative to non-radiative processes will produce a more efficient light emitter.

Due to the excitonic nature of the III-nitrides the free electron in the CB and free hole in the VB can be bound to each other through Coulomb attraction creating an exciton. Both free and bound excitons exist in the III-nitrides resulting in many optical transitions in addition to the free e-h transition. The free exciton (FE) can move largely unimpeded in the crystal and does not contribute to the electrical conductivity but has influence on the absorption and emission processes [49]. These are usually evident in high quality samples with low defects and impurities, and are more dominant in the emission spectra at low temperature compared to room temperature. The emission energy of the FE is smaller than the material's bandgap (E_g) due to the contribution of the binding energy (E_b). A,B and C FEs can occur due to the valence band splitting as was described earlier in section 2.1.3. Bound excitons (BE) also occur due to impurities existing within the material, such as donors and acceptors. The BEs which are most dominant in the III-nitrides are the neutral donor bound exciton and neutral acceptor bound exciton, which are often a result of nitrogen vacancies and p-type impurities, respectively [69]. These have even lower emission energy than the FEs due to their additional localisation energy (E_{loc}) [49].

As carriers move through the crystal they interact strongly with impurities and lattice vibrations. The latter causes a change in energy and momentum which often results in phonon absorption or emission [69]. Several types of phonons can occur in semiconductors such as optical and acoustic. The optical phonons are more associated with the III-nitrides due to having shorter wavelengths than the acoustic phonons. The strong interactions between electrons and optical phonons in polar materials, such as the III-nitrides, can have an influence on the optical properties. This is often seen in the PL spectra of GaN where several phonon

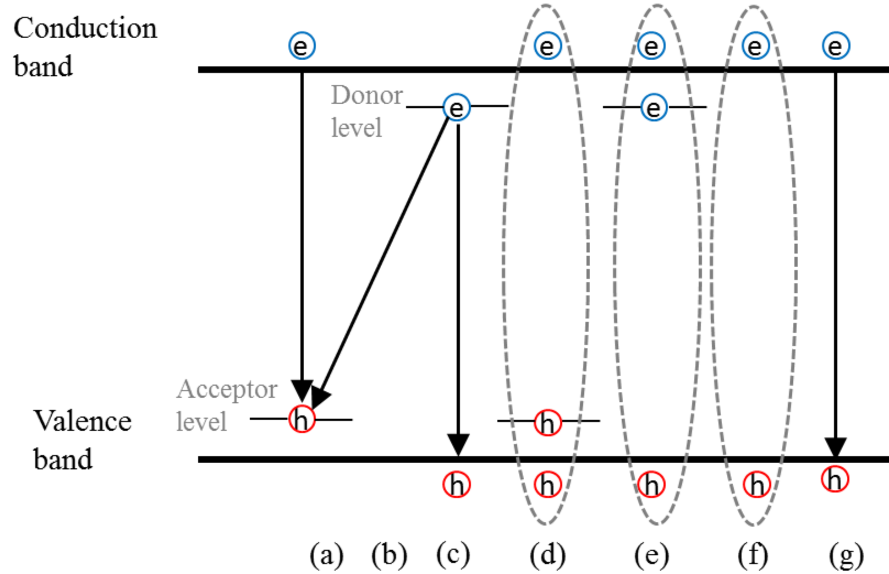

Figure 2.6: Schematic of the various radiative recombination processes in semiconductors. The emissions shown are: (a) free-to-bound (b) donor-acceptor pair (c) bound-to-free (d) neutral acceptor bound exciton (e) neutral donor bound exciton (f) free exciton (g) band-to-band. *Schematic adapted from [49].*

replica peaks are evident on the lower energy side of the main emission peak. These represent the longitudinal optical (LO) phonon replicas of FEs and BEs and are a result of the Fröhlich interaction. The Fröhlich interaction is a Coulomb interaction between the electrons and the longitudinal electric field produced by the LO phonons [58].

2.3.1 Exciton Localisation

Exciton localisation is an optical property which is commonly found in ternary and quaternary III-nitrides (and other semiconductor alloys). It can be described as the trapping of excitons to a small area as a result of potential fluctuations within the alloy. This property is commonly used to explain the high luminescent efficiencies of the III-nitrides despite having large defect densities in comparison to other semiconductors. The main causes of the potential fluctuations are from compositional fluctuations, variations in quantum well (QW) width, strain inhomogeneities and phase separation [70, 71, 72]. Some of these potential inhomo-

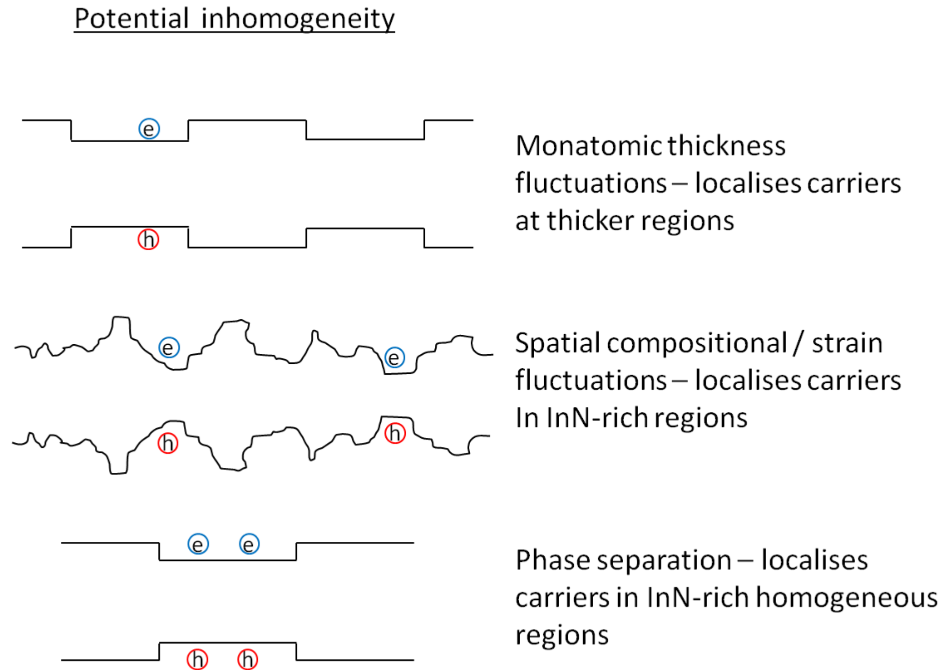

Figure 2.7: Illustration of the potential fluctuations which cause carrier localisation and Stokes-like shift. *Illustration adapted from [72].*

geneities which can lead to exciton localisation are illustrated in Figure 2.7 for InGaN.

The presence of exciton localisation within a compound or alloy can be seen in the optical spectra, whereby there is a large energy difference between the absorption energy (or bandgap energy (E_g)) and the emission energy. The emission occurs at lower energy in comparison to the absorption (or E_g) due to the excitons moving to become trapped in local potential minima as indicated in Figure 2.7. This is often referred to as the Stokes' shift.

2.4 Growth of III-Nitride Structures

This section provides information on challenges associated with growing III-nitrides and the common structures used for the study and application of these materials. The growth method used for the samples studied throughout this thesis and discussed here is metal-organic chemical vapour deposition (MOCVD). This technique was used at both Tyndall National Institute and University of Cambridge to grow the studied samples. Details of the MOCVD growth technique, with comparisons to molecular beam epitaxy (MBE), are given in Chapter 3.

2.4.1 Challenges of Growth

Many challenges arise when in pursuit of high quality materials such as III-nitride compounds and alloys. The growth challenges are a major factor in the development of electrical and optoelectronic devices, and require a great deal of research and understanding if they are to become commercial products. As discussed in Chapter 1, a high quality, high efficiency blue InGaN LED was achieved by developing nucleation layer technology and overcoming the p-doping problem. These blue (and white) LEDs are now widely available on the commercial market.

However issues are still apparent in the growth of InN containing alloys, in order to achieve high quality layers, due to the low thermal stability of InN [73]. This requires careful balancing of all the MOCVD growth parameters such as temperature, precursor flow, carrier gas flow, pressure and growth rate, which can vary depending on reactor. A universal outcome is that the InN content within InGaN (and InAlN) can be controlled by the growth temperature, if within the range viable for InN incorporation, regardless of the MOCVD reactor. High quality, high InN containing InGaN layers are difficult to achieve due to the difficulty in breaking the strong bond of nitrogen at low temperatures. As the temperature is reduced to incorporate more InN, the ammonia (NH_3) used as the N source insufficiently decomposes [57, 74]. This leads to phase separation and often In or Ga droplets on the surface. Increased growth rate and a large ammonia flow have been reported to help counteract these issues [73, 75]. The choice of carrier gas for the metal precursors, usually hydrogen, nitrogen or a mixture of

the two, is also important. Nitrogen is often the preferred gas when growing InN containing alloys, whereas hydrogen is commonly used for GaN growth. Nitrogen has the benefit in that it aids the dissociation of ammonia, unlike hydrogen, while hydrogen has been reported to have etching effects on InN containing alloys [73]. Adding small amounts of hydrogen to the predominant nitrogen carrier gas has been seen to improve crystal quality of InGaN when compared with pure nitrogen [76]. An investigation of the influences of adding hydrogen is presented in Chapter 4.

Achieving high quality InAlN films has proven to be very difficult in comparison to the ternaries InGaN and AlGaN, which is another reason why it is the least studied out of the three. Like InGaN, the most common technique and the one used throughout this thesis to grow InAlN is MOCVD. The main issues associated with InAlN growth are the large differences between the InN and AlN binaries including; growth temperature (~1100°C for AlN and ~600°C for InN), the preferred V/III ratios, and the length and energy of their covalent bonds [75]. These factors lead to a decrease in the diffusion length of the Al adatoms, indium surface segregation and phase separation. Therefore growing InAlN at intermediate temperatures can result in poor crystalline quality and surface morphology [77]. The most common surface feature reported by groups growing InAlN layers by MOCVD, regardless the template, are hillocks. These features, illustrated in Figure 2.8, are not fully understood and require further investigations as to their origin and influence on the optical properties. Cracking is also common when growing InAlN below the lattice match point on GaN due to tensile strain.

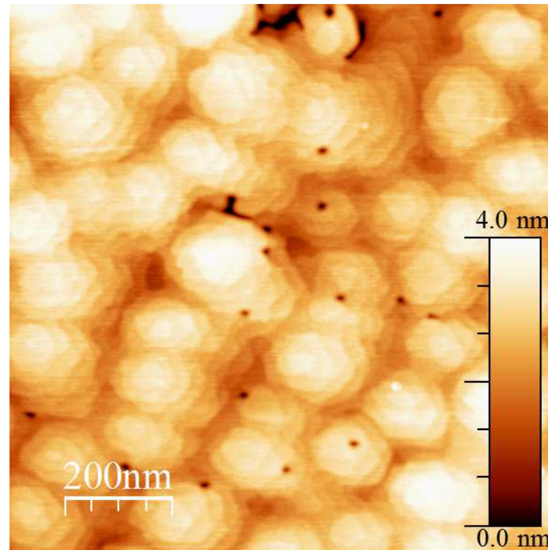

Figure 2.8: AFM image of an InAlN layer showing hillock features emerging on the surface. The colour scale gives the vertical height in nanometres. *Image taken by collaborators at Tyndall National Institute.*

2.4.2 Substrates

In heteroepitaxial growth the choice of substrate is important for the quality of material as a large mismatch in crystal lattice spacing can affect the structural, electrical and optical properties of the film. Homoepitaxy is uncommon due to the lack of commercially available bulk single crystal GaN substrates. The most common substrate used for growth of III-nitrides is sapphire (Al_2O_3) due to the availability of good quality, large area crystals at low cost. Other frequently used substrates are silicon carbide (SiC), silicon (Si) and GaN. The lattice mismatch (%) between each of the III-N compounds and the substrates are presented in Table 2.2. Thermal expansion is also an important substrate property to consider due to the high temperatures required for MOCVD growth of III-nitrides. Different thermal expansion coefficients between the III-nitride material and substrate can result in strain due to the changes in lattice constant with temperature. This is important when the sample is cooled as it can cause wafer bowing, cracking, structural defects and piezoelectric fields, resulting in poor quality material and changes in optical properties. The thermal expansion coefficients for the III-nitrides are given in Table 2.2.

	Lattice mismatch (%)				Thermal expansion coefficient	
	Sapphire	SiC	GaN	Si	Δa/a ($\times 10^{-6}$K^{-1})	Δc/c ($\times 10^{-6}$K^{-1})
AlN	12.5	1.0	-2.4	74.6	4.2	5.3
GaN	14.8	3.3	–	70.3	5.59	3.17
InN	25.4	14.0	10.6	53.1	5.7	3.7
Sapphire					7.5	8.5
SiC					4.2	4.68
Si					3.59	3.59

Table 2.2: Lattice mismatch between each of the III-N and commonly used substrates grown c-plane (0001) and the thermal expansion coefficients for the III-N [48, 49].

When the lattice constant of the III-nitride binary (or alloy) is smaller than that of the substrate the layer is under compressive strain and tensile when the opposite. This is denoted by the sign of the strain value (+ = tensile) as calculated for a and c parameters using:

$$\epsilon_a = \frac{a_s - a_0}{a_0} \tag{2.6}$$

$$\epsilon_c = \frac{c_s - c_0}{c_0} \tag{2.7}$$

where a_s and c_s are the measured lattice parameters of the sample or layer under study, and a_0 and c_0 are the lattice parameters of the substrate, under layer or reference. For example when growing c-plane (0001) GaN on sapphire it induces a large compressive strain due to sapphire having a much larger a_0 lattice parameter. The strain is reduced significantly when growing on closer matched substrates like SiC.

2.4.3 Epilayers and Quantum Wells

For studying the various properties of any III-nitride material a simple epilayer is grown with often a buffer and nucleation layer between the thin nitride film and substrate. GaN and AlN are the most common low temperature buffers used for nucleation of III-nitride films as developed by Nakamura, Amano and Akasaki (discussed in Chapter 1). A schematic of an InGaN epilayer sample structure is

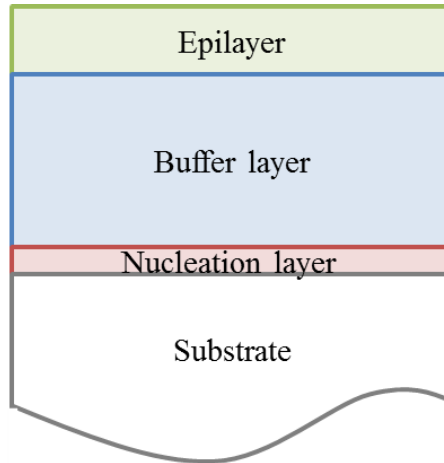

Figure 2.9: Schematic of an epilayer structure with buffer layer, nucleation layer and substrate indicated.

shown in Figure 2.9. The nucleation layer aids in the lateral growth of the GaN or AlN, reducing strain, decreasing defect densities and improving crystal quality. A thick GaN or AlN buffer layer is grown at higher temperature to further improve the crystal quality and provide a suitable template for growth of the epilayer. This thick buffer layer aids in the relief of strain as the material relaxes with increasing growth thickness.

Heterostructures are advantageous in improving optoelectronic device performance due to quantum confinement. Engineering the band structure by growing a lower bandgap alloy between two higher bandgap layers such as GaN/InGaN/GaN produces a quantum well (QW) structure. This helps in confining the electrons and holes in 2D, increasing electron and hole wave function overlap, improving radiative recombination as shown in Figure 2.10(a). Implications arise due to differences in composition, lattice parameter and spontaneous polarisation between the GaN and InGaN, which results in induced electric fields and piezoelectric polarisation. These internal electric fields have a negative influence on the optical properties. This is known as quantum confined Stark effect (QCSE). The electric fields cause the bands to tilt, spatially separating the electron and hole wave functions causing a reduction in radiative recombination efficiency as the wave functions are now situated in triangular wells. This is illustrated in Figure

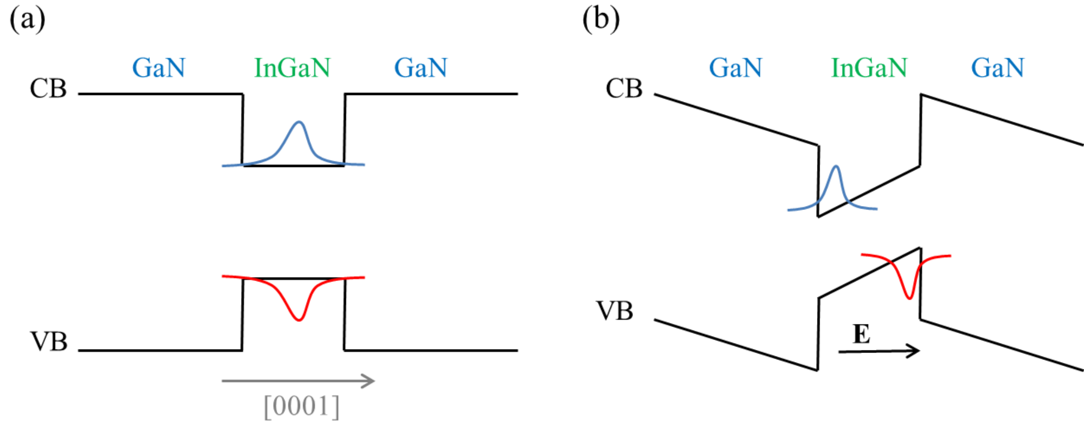

Figure 2.10: (a) QW band structure illustrating quantum confinement with the growth axis [0001] along the horizontal direction. (b) Schematic of the band tilting of a QW structure due to an internal electric field. Electron and hole wave functions are shown with spatial separation indicating the lack of overlap of the charge carriers and reduction in radiative efficiency.

2.10(b) for a c-plane (polar) QW structure. The QCSE causes a red-shift (lower energy shift) in the emission compared to the non piezoelectric condition due to the lower energy transitions between the electrons and holes. The probability of radiative recombination is further reduced with increasing well width as the wave functions separate further. An increase in charge carrier density through photoexcitation (or increased current) can counter the QCSE and result in a blue-shift (higher energy shift) in the emission peak [78]. This is known as the screening effect whereby the internal piezoelectric field is cancelled out by the field generated due to Coulomb repulsion of the charge carriers [69].

Transistor-like devices such as HFETs and HEMTs have utilised the carrier confinement in the triangular wells at the heterojunctions of AlGaN/GaN and InAlN/GaN structures to obtain a two-dimensional electron gas (2DEG). This electron channel allows increased carrier density, increased electron mobility and therefore increased current capabilities, making these heterostructures suitable for high power devices.

For device purposes the buffer layer is often grown with the incorporation of dopants to produce an n-type layer. Silicon (Si) is the most commonly used n-dopant for GaN (and AlN). This allows easy control over the doping levels.

Since as-grown GaN is unintentionally n-type using Si as a donor allows carrier densities to be increased from around 10^{15}–10^{16} cm^{-3} to 10^{17}–10^{19} cm^{-3} [49]. For p-type doping Mg is most commonly used. As was discussed in Chapter 1 p-type doping is more difficult with the need for post growth activation of the Mg in order to achieve desired carrier densities. The p-layer is grown as a thick capping layer after the growth of the thin QWs used as the active region in devices.

2.4.4 LEDs and HEMTs

The basis of the LED is the p-n junction. As described previously this is achieved by sandwiching an active region, usually a series of QWs, between n-type and p-type material. Contacts are made to the n and p layers through various fabrication processes in order to create a device. This allows electrical measurements to be made, although no electrical measurements were performed in this investigation. A schematic of an LED is shown in Figure 2.11.

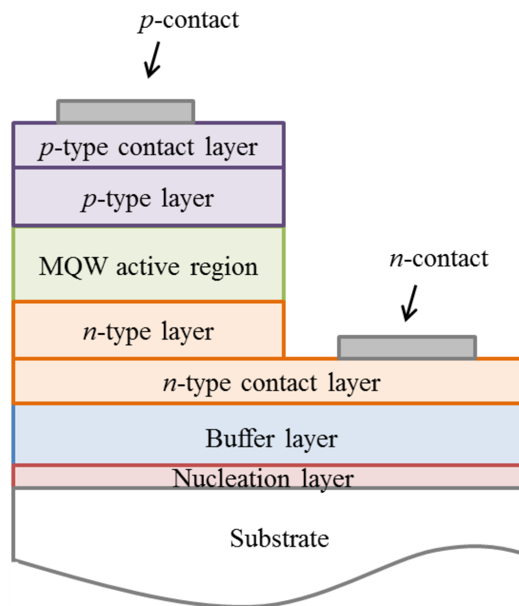

Figure 2.11: Schematic structure of a MQW LED showing the active region between the n and p layers.

Another device which is associated with III-nitride alloys is the high electron mobility transistor (HEMT). This is mentioned throughout the thesis as an application of InAlN. The structure is shown in Figure 2.12 illustrating the 2-dimensional electron gas (2DEG) induced in the channel layer (usually undoped GaN) at the interface of the barrier layer (InAlN). The 2DEG allows the flow of high current needed for high power electronics and is achieved by the large differences in polarisation between the materials. Again no electrical measurements were performed in this thesis.

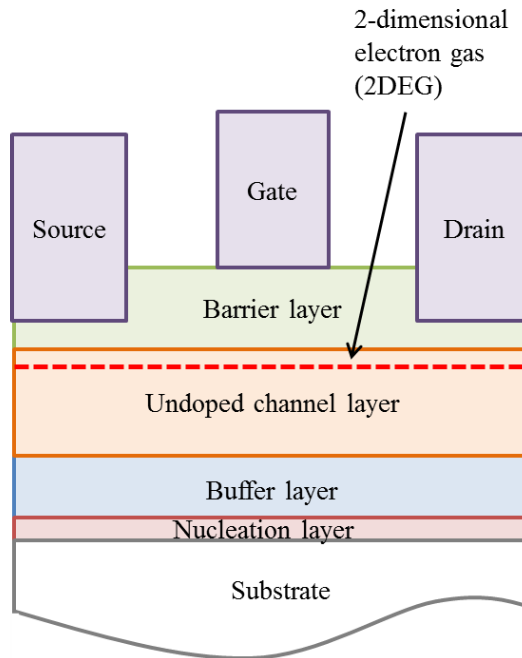

Figure 2.12: Schematic structure of a simple HEMT showing the 2DEG region creasted between the channel and barrier layers.

Chapter 3

Growth and Experimental Techniques

3.1 Introduction

This chapter contains information on the growth process for all the samples studied and experimental methods used throughout this study. The principles of the structural, compositional and luminescence techniques are given with details of the specific systems used. The techniques include secondary electron (SE) imaging, wavelength dispersive x-ray (WDX) spectroscopy, cathodoluminescence (CL) spectroscopy (and imaging), and photoluminescence (PL) spectroscopy. The thesis also includes analysis of data provided by collaborators using complementary techniques, including Rutherford backscattering spectrometry (RBS), x-ray diffraction (XRD) and atomic force microscopy (AFM). A brief description of these techniques will be presented in this chapter.

3.2 Growth

Metalorganic vapour phase epitaxy (MOVPE), also commonly known as metalorganic chemical vapour deposition (MOCVD), is the main growth method used by the University of Cambridge and Tyndall National Institute to grow all the epilayer and LED samples featured in this thesis. Both groups use closed coupled showerhead designed MOCVD reactors. A photo of the 3×2" AIXTRON close

coupled showerhead MOCVD reactor used at Tyndall is shown in Figure 3.1. The MOCVD technique is often the preferred method for growth of III-V crystalline materials over other techniques such as molecular beam epitaxy (MBE) due to its faster growth rates, its capability to grow large areas and its ability to produce good quality layers [57, 73, 74]. These factors are the reason it is the leading growth method when manufacturing materials for commercial products like LEDs, solar cells, HEMTs etc [50, 75]. As stated above MBE is another technique which is also commonly used to grow nitride materials, including cubic type structures [79, 80, 81, 82]. It can produce layers with a high degree of uniformity and deposition precision due to its use of highly directional elemental beams. The use of a reflection high-energy electron diffraction (RHEED) gun allows accurate in-situ monitoring of the growth [83, 84]. Also as the system is under ultra high vacuum (UHV) contamination is greatly reduced in comparison to MOCVD. The difficulty arises in obtaining a suitable nitrogen source due to the low growth temperatures as the N-N bond in molecular nitrogen is very strong [48]. Plasma-assisted methods such as radio-frequency (RF) and electron-cyclotron resonance (ECR) are used to produce a supply of active nitrogen.

Figure 3.1: MOCVD reactor used at Tyndall National Institute. This is an 3×2" AIXTRON close-coupled showerhead MOCVD reactor. *Image taken from http://www.tyndall.ie/content/nitride-materials-0.*

Unlike MBE, which is a physical deposition process, MOCVD uses a gas phase chemical reaction when growing crystalline layers [85]. In the reactors used in this study the group III gases are transported from the precursor bubblers into the chamber, via the showerhead, by using a carrier gas such as nitrogen (N_2) or hydrogen (H_2). The precursors used for the source materials throughout this thesis are trimethylgallium (TMGa), trimethylindium (TMIn) and trimethylaluminium (TMAl). The group V (nitrogen) is supplied by an ammonia (NH_3) source which is also injected into the reactor chamber via the showerhead. The showerhead design, as shown in Figure 3.2, consists of a large number of small gas inlet holes allowing the gases to be distributed evenly resulting in a more uniform growth.

The substrate wafer is placed on a heated susceptor directly under the incoming gas shower. A chemical reaction occurs between the injected gases in the chamber resulting in precursor decomposition as shown in Equation 3.1 for GaN [86]. This allows adsorption of the III-nitride materials on the exposed wafer surface.

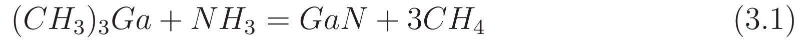

$$(CH_3)_3Ga + NH_3 = GaN + 3CH_4 \tag{3.1}$$

Various factors have to be taken into consideration when growing semiconductor layers including temperature, ratio of III:V materials and reactor pressure. A careful balance between these variables is required in order to obtain good quality layers. For example when growing InGaN a high temperature is needed to grow GaN (~1100°C) whereas lower temperatures are more suitable for InN growth (400–650°C). Varying the temperature allows control of the InN incorporation. Choice of substrate is also an important factor as large lattice or thermal mismatches can reduce the quality of the resulting compound or alloy [74, 75]. Common substrates used for growth of nitride based materials are sapphire (Al_2O_3), silicon (Si), silicon carbide (SiC), bulk GaN and other III-N templates. In this work the main substrate used is sapphire.

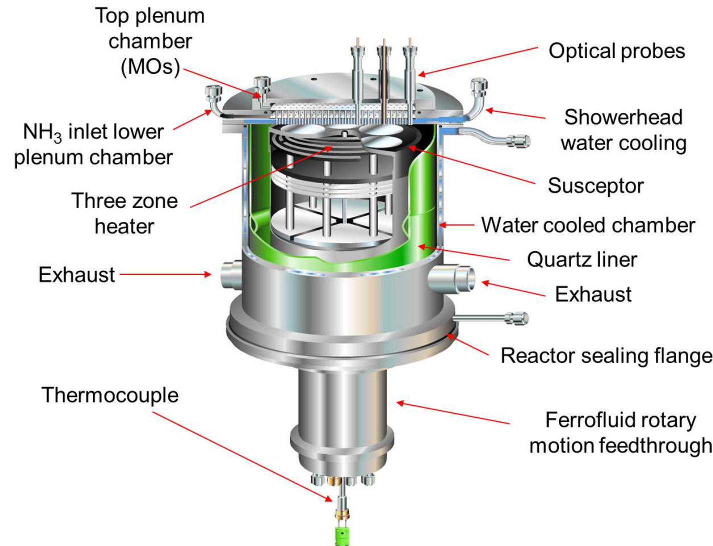

Figure 3.2: Close up schematic of an MOCVD showerhead reactor. *Image credit to Thomas Swan Scientific Equipment Ltd - now AIXTRON.*

3.3 Scanning Electron Microscopes

Scanning electron microscopes (SEMs) operate similarly to conventional optical microscopes by allowing objects to be seen that are normally invisible to the human eye. They differ by using energetic electrons as a source instead of light. This allows the resolution to be pushed beyond the diffraction limit of visible light with the best resolution down to approximately a nanometre [87]. This makes them very useful for looking at features of materials on a sub-micron scale.

The SEM comprises of an electron gun where the electrons are produced using a filament, either thermionically or by a large electric field. The thermionic based electron source uses either a tungsten hairpin made from tungsten wire or a piece of lanthanum hexboride (LaB_6) crystal. The electron probe microanalyser (EPMA) used for measurements within this thesis uses the tungsten hairpin design which is cheap and easily replaceable. This design results in higher currents in comparison to an electric field emission gun, which is desirable when performing microanalysis [89]. The field emission gun (FEG) SEM source uses a single piece of tungsten crystal shaped to a fine point of <100 nm which can produce a small spot size of approximately 1 nm resulting in high quality imaging [90]. The FEGSEM used for measurements within this thesis is a FEI Quanta 250 environ-

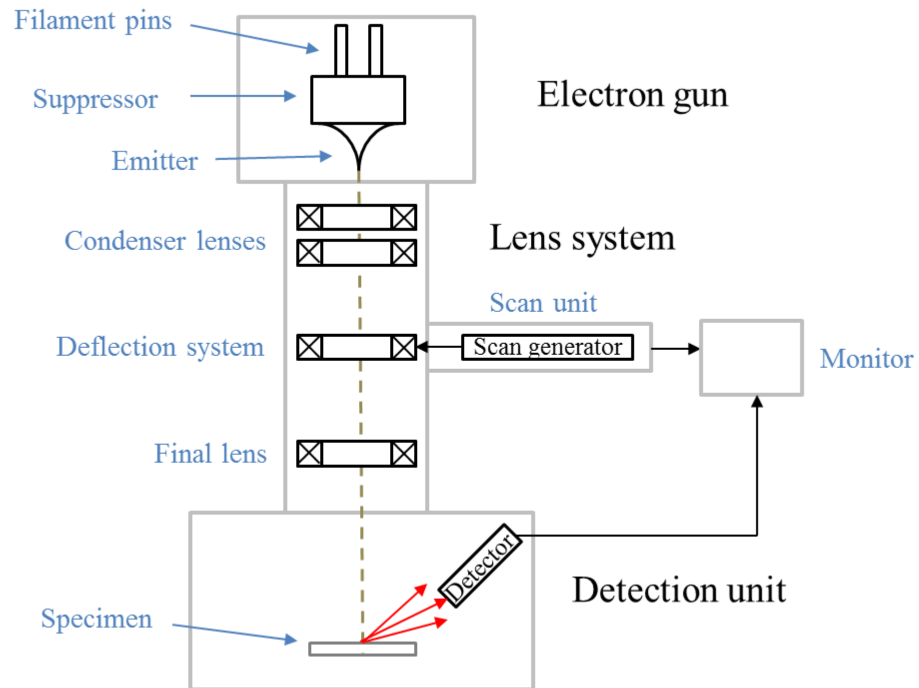

Figure 3.3: Schematic of a FEI Quanta ESEM. *Image adapted from [88].*

mental SEM (ESEM). The operating principles of both the EPMA and FEGSEM are the same. The electrons are accelerated from the tungsten cathode to the anode and down the column, where the energetic electron beam is controlled by electromagnetic lenses within the column. Several lenses and apertures are used in order to produce a small focused beam spot on to the sample or object within the chamber. A schematic of the FEI Quanta ESEM is shown in Figure 3.3 with the components of the SEM indicated. An image is generated by using a set of scanning coils to deflect the beam and raster over a surface area allowing a signal to be detected at each point. This allows the SEM to resolve very small features and to have a large depth of field. The electron gun, column and chamber are all held under high vacuum to protect the filament, prevent contamination and reduce scattering, allowing electrons to reach the specimen and detectors.

When the beam of electrons impinges the sample surface several interaction processes occur resulting in a range of signals such as secondary electrons (SEs), backscattered electrons (BSEs), characteristic x-rays, bremsstrahlung x-rays, Auger electrons, transmitted electrons, cathodoluminescence (CL), and

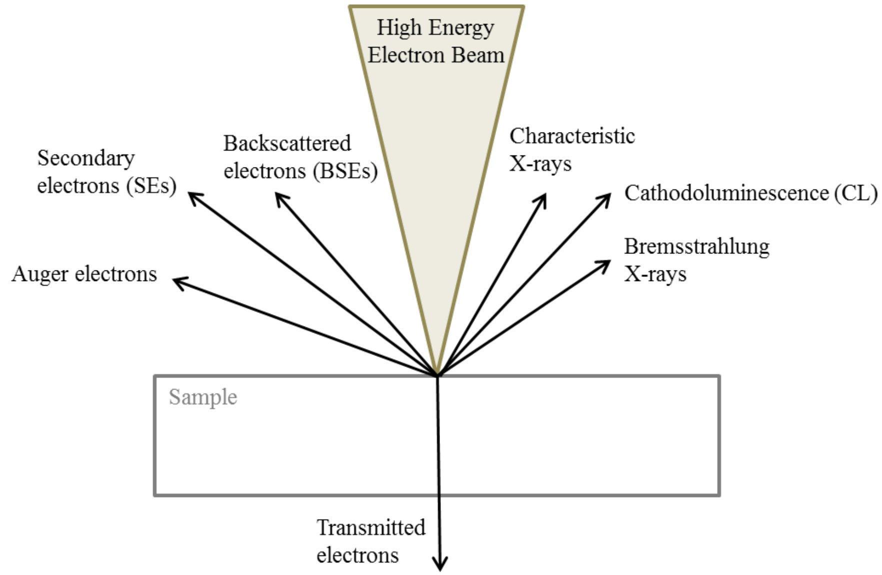

Figure 3.4: Scattering effects from impinging high energy electron beam.

many more. The main electron-specimen interactions studied in this work are SEs and BSEs for imaging, characteristic x-rays for wavelength dispersive x-ray (WDX) analysis, and CL for optical spectroscopy.

SEs are generated through an inelastic scattering process whereby the beam of energetic electrons interacts with loosely bound outer shell electrons. Inelastic scattering can be described by the semi-empirical Bethe expression [91] for the mean rate of energy loss for distance S travelled in a solid as

$$\frac{dE}{dS} = -2\pi e^4 N_A \frac{\rho Z}{EA} ln\left(\frac{1.166E}{J}\right) \tag{3.2}$$

$$J = (9.76Z + 58.5Z^{-0.19})10^{-3} \tag{3.3}$$

where e is electronic charge, N_A is Avogadro's number, ρ is density, A is atomic weight in g/mol, E is the mean electron energy in keV and J is the mean ionisation potential in keV as expressed in Equation 3.3 [91]. If enough kinetic energy is transferred from the incident electron beam the SEs will move through the specimen and will either lose energy through other interactions or reach the surface. The SEs which reach the surface will be ejected if they have enough energy to overcome the surface barrier energy. Therefore SEs are very surface

sensitive making them ideal for imaging surface features. The emitted SEs have characteristic energies of < 50eV, unlike BSEs (see below) which have energies > 50eV [92]. The most common detector used for SE signal is an Everhart-Thornley (E-T) detector [93]. It is located inside the SEM chamber at an angle to the specimen and consists of a scintillator with a Faraday cage, and an attached photomultiplier tube. The SEs are attracted to the positively biased Faraday cage and accelerated towards the more highly positively biased voltage scintillator where photons are produced. The photons are guided towards the photomultiplier where the signal is then amplified and detected. The SE signal will increase if the sample is tilted towards the E-T detector as more SEs become in direct line with the detector. This is also the case for BSE signal (see below).

BSEs are produced through elastic scattering which can be expressed using the Rutherford scattering cross section for an event exceeding a specified angle ϕ_0,

$$Q(> \phi_0) = 1.62 \times 10^{-20} \frac{Z^2}{E^2} cot^2 \frac{\phi_0}{2} \tag{3.4}$$

where Z is atomic number and E is the electron energy in keV [90]. Most electrons are backscattered into the specimen as the average deviation per interaction is approximately 2°–5° so only a small number of the impinging electrons make their way back out. This is illustrated in Figure 3.5 by the simulated BSE trajectories shown in red. BSEs have a strong positive dependence on atomic number and inverse dependence on electron energy. This makes BSEs ideal for imaging topography and compositional variation. BSEs can also be detected using a E-T detector when operating in negative bias; however, only BSEs in direct line with the detector will be collected which makes the ETD inefficient. Other dedicated BSE detectors include scintillator backscatter detectors and solid-state diode detectors which improve signal by increasing the collection angle.

The beam penetration volume (also known as interaction volume) is an important factor to consider when using SEMs for imaging and other techniques. Properties such as beam energy, sample composition and surface charging effects can alter the volume of beam penetration. The penetration has a strong dependence on beam energy as shown by the Kanaya-Okayama range equation (3.6) where E_b is beam energy in keV, A is the atomic weight in g/mol, ρ is the density in g/cm^3 and Z is the atomic number [90, 95]. This is a more general expression

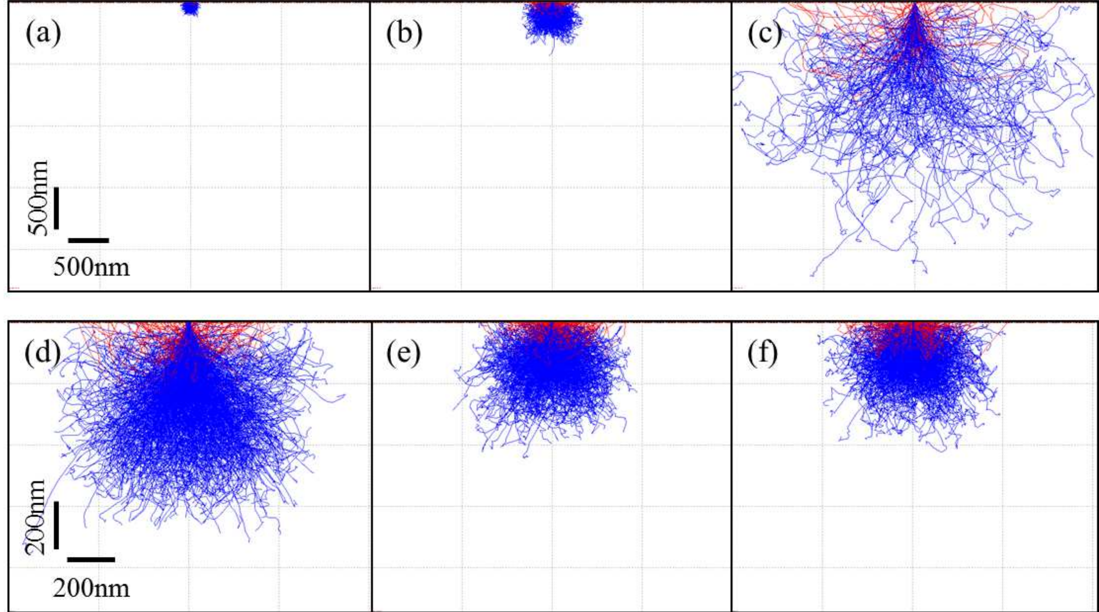

Figure 3.5: Beam penetration volume of interacting electrons for (a) 5kV (b) 10kV (c) 30kV beam voltages in GaN, and (d) AlN (e) GaN (f) InN for 10kV beam voltage. BSE trajectories are illustrated in red. These figures were generated using Casino Monte Carlo electron trajectory simulation software [94].

of the Gruen range equation (3.5) where k is atomic number dependent and a function of energy, and α depends on atomic number and E_b [91].

$$R_e = \left(\frac{k}{\rho}\right) E_b^{\alpha} \tag{3.5}$$

$$R_e = \left(\frac{0.0276A}{\rho Z^{0.889}}\right) E_b^{1.67} \tag{3.6}$$

The penetration volume for different beam energies is illustrated in Figure 3.5(a)–(c) by the individual electron trajectories within GaN material simulated using Casino Monte Carlo electron trajectory simulation software [94]. All Monte Carlo electron trajectory simulations presented throughout this thesis are generated using Casino software. Figure 3.5(a)–(c) show an increase in interaction volume with increasing beam energy for the same number of simulated electrons. The opposite effect occurs for increasing atomic number and density when the beam energy is fixed as more elastic scattering events occur. This is shown in Fig-

ure 3.5(d)–(f) for increasing atomic number III-nitride compounds with the BSE trajectories shown in red. As well as the interaction volume the main contributing factor in achieving high resolution images (∼1 nm) is the diameter of the beam at the sample surface. Therefore the beam should be focused and the beam current should be kept low to reduce beam spreading in order to gain high resolution. Other techniques such as WDX and CL require differing beam properties as will be discussed in the subsequent sections.

For all SEM based techniques samples are grounded to the metal sample holder by using silver paint in order to aid with current flow. Insulating samples require an additional conductive coating (e.g. carbon) to alleviate charging effects at the surface and further improve current flow through the sample. The coating is not necessary for the environmental SEM where the option of low vacuum is available.

3.4 Structural and Composition Characterisation Techniques

In this work several structural and composition techniques were used to investigate various semiconductor alloys including InGaN, InAlGaN and InAlN. A detailed description of each technique will be given in this section, including those used by collaborating groups. There are many advantages to using various techniques and this will be highlighted within the following subsections.

3.4.1 Wavelength Dispersive X-ray Spectroscopy

Wavelength dispersive x-ray (WDX) spectroscopy measurements used throughout this thesis are performed on a modified Cameca SX100 electron probe microanalyser (EPMA). The EPMA is equipped with 3 wavelength dispersive spectrometers used for elemental x-ray detection as shown in the schematic in Figure 3.6. The EPMA is also equipped with a home built cathodoluminescence (CL) detection system which will be further discussed in section 3.5.1. WDX has many advantages over other compositional characterisation techniques in that it is non-destructive, can be used for high resolution spatial mapping, and is

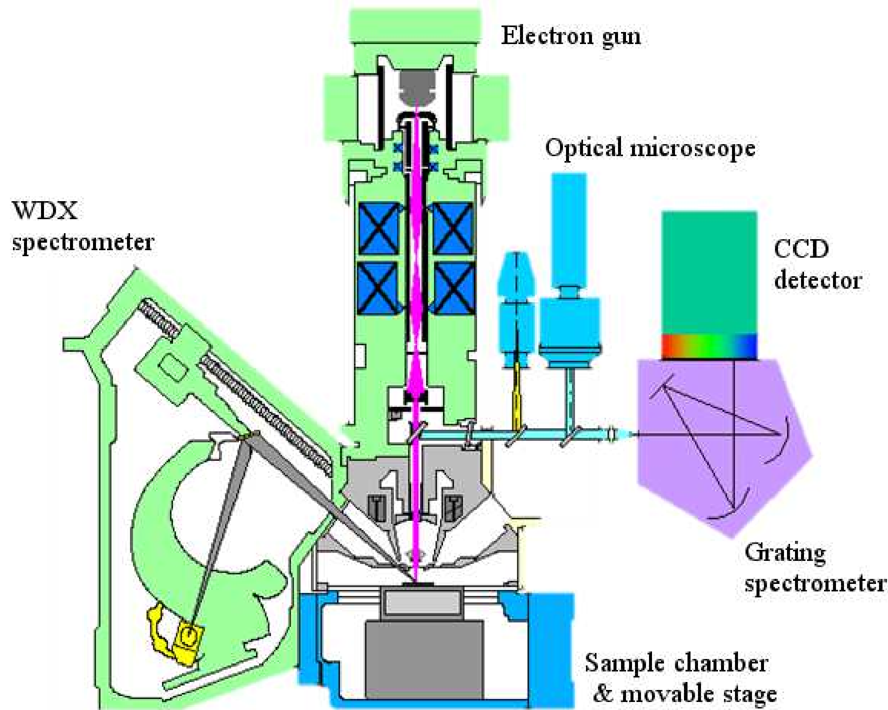

Figure 3.6: Schematic of Cameca SX100 EPMA with attached spectrograph for CL measurements. *Edited image, original image credit to Cameca.*

cheaper and more widely available [96]. Also the use of wavelength dispersive spectrometers instead of a single Si(Li) x-ray detector, as in energy dispersive x-ray (EDX) spectroscopy, provides finer spectral resolution and improved peak-to-background. This minimizes the possibility of peak overlap which improves element determination. Another advantage of using WDX over EDX is the reduction in spectral artefacts which can lead to incorrect analysis [97]. Also it can be used in conjunction with other SEM products such as imaging and CL to gain deeper understanding of the material under study [76].

The EPMA uses the same principles as a normal operating SEM (see section 3.3). The energetic electron beam bombards the sample with accelerated electrons resulting in several scattering events, one of which is the generation of characteristic x-rays. These x-rays are detected by the WDX spectrometers. The spectrometers work on the principle of Bragg's law (Equation 3.7), where d corresponds to the lattice spacing, n is the diffraction order, λ is the x-ray wavelength

WDX crystal	2d (Å)	X-ray range (keV)	X-rays dectected
TAP (thalium acid phthalate)	25.76	0.581–2.168	Al K_α, Ga L_α
PET (pentaerythritol)	8.75	1.699–6.273	In L_α
PC1 (synthetic pseudocrystal)	59.29	0.255–0.947	N K_α, O K_α

Table 3.1: Details of the WDX crystals including their x-ray energy range and the main characteristic x-ray lines detected in this study.

and θ is the angle between in incoming and diffracted x-rays. Different diffracting crystals are used to detect x-rays of varying energy [89].

$$n\lambda = 2d \sin\theta \tag{3.7}$$

The angle θ between the sample, crystal and detector is always fixed by having the crystal and detector on a rotating focusing circle known as the Rowland circle, allowing the x-rays with characteristic wavelengths to be detected as shown in Figure 3.7 [89]. Two of the spectrometers within the EPMA are positioned vertically as illustrated in Figure 3.7 and one is orientated horizontally. The horizontally positioned spectrometer is advantageous for rougher samples with varying heights as the Rowland circle is less sensitive to movement along the z-axis in this orientation [90]. Each of the spectrometers contains several diffracting crystals allowing most elements to be detected (Z>4). The choice of crystal is important as it is advisable to opt for an energy/wavelength range measuring the K_α (Z<30) or L_α (Z>30) lines as these are usually the lines with highest intensity [98]. The crystals used for the work within this thesis are TAP (thalium acid phthalate), PET (pentaerythritol) and PC1 (synthetic pseudocrystal). PC1 is used for detecting the lighter elements, TAP is used for middle range elements and PET for heavier elements. The crystal details are provided in Table 3.1.

Qualitative measurements can be performed for elemental detection. Each diffracting crystal scans through a full range and an x-ray spectrum is generated, with the peak counts relating to certain characteristic x-ray lines. Once the elements are known quantitative measurements can be performed. The crystals are set to a specific angle according to the x-ray energy of the element that is

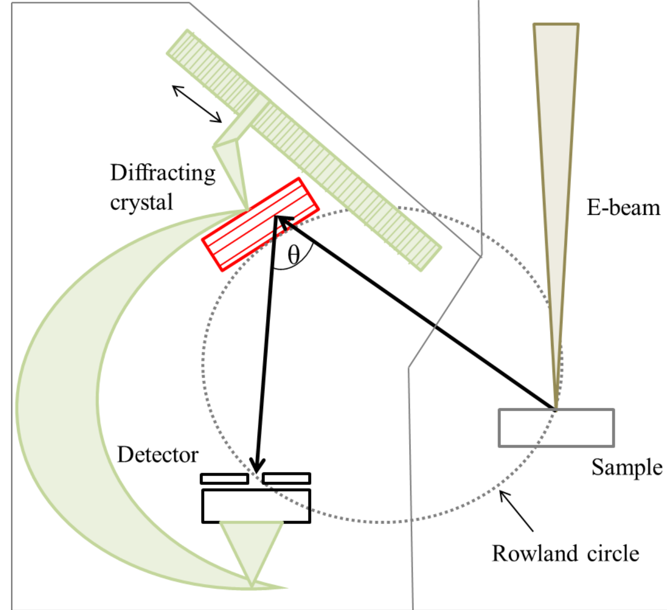

Figure 3.7: Schematic of WDX spectrometer operation with the x-rays detected from the rotating diffraction crystal that satisfy Bragg's law. Both detector and crystal rotate together and are fixed on the focusing Rowland circle to detect a broad spectrum of x-rays.

being measured. For this measurement a comparison with a known standard is required. The choice of standard is important for accurate analysis. It should be similar to the measuring sample in terms of atomic number, homogeneity and composition if possible [90]. Also it should be chemically and thermally stable. The standards used for materials studied in this work are GaN, AlN, InP and MgO. The intensity of the signal from the sample (I_x) is compared with the intensity of the chosen standard (I_{std}) to obtain the k-ratio (k-ratio=I_x/I_{std}). This k-ratio is then converted to a weight percent through an iterative ZAF matrix correction routine for each of the elements measured as shown by Equation 3.8, where C_x and C_{std} are the weight fractions of the element of interest in the sample and standard respectively [90]. This equation is applied separately for each element measured.

$$\frac{C_x}{C_{std}} = [ZAF]\frac{I_x}{I_{std}} = [ZAF]k \tag{3.8}$$

The factors that the routine corrects for are atomic number (Z), absorp-

tion (A) and fluorescence (F). The atomic number factor takes into account the backscattering and stopping power effects that each element has on the impinging beam of electrons. The absorption factor corrects for the x-rays that are absorbed within the sample before reaching the surface. This effect is usually the biggest factor and increases with increasing beam voltage as the electron beam penetrated deeper into the sample. The fluorescence factor makes adjustments for the lower energy characteristic x-rays that have been emitted indirectly following the absorption of higher energy x-rays from other elements within the sample. As the chances of secondary fluorescence occurring is low the fluorescence factor is usually the least important in the calculation of composition.

The sample is situated on a high precision movable scanning stage and WDX mapping can be used to gain spatial information on element distribution within a specimen. For the mapping in this work the spectrometers are set as in quantitative measurements but this time only raw counts are measured and no standard is required. The WDX map is built up pixel by pixel, as the beam rasters over the surface and can be measured simultaneously with SE, BSE or CL images/maps. Fully quantifiable maps can be obtained but this requires a complete quantitative analysis at each pixel which can be both difficult and time consuming [90].

WDX spectroscopy is mostly used for measuring thick layers or bulk materials but it can also be used to study thin films with the aid of layers analysis software [99, 100]. This is most relevant for thin layers that have heavier elements as a high beam voltage is required to excite the x-rays but results in increased penetration depth. For example the In containing thin films studied in this thesis require the use of the layers analysis software as the energy of the In L_α x-ray is 3.29 keV and requires a higher beam energy for excitation. This results in a fairly large interaction volume, generating x-rays from the underlying buffer or substrate. The program simulates k-ratios by altering weight percent, density and thickness of each of the layers, and an iterative process is used to obtain a best fit to the measured quantitative data. Data over a range of beam voltages is required to generate an accurate fit by increasing the number of data points.

Monte Carlo electron trajectory simulations (Casino software) provide information on beam interaction volume, energy deposition and penetration depth, which is useful when performing WDX thin film measurements [94]. The simulation requires the input of composition and density of each layer. It will show if

the beam is contained within the layer of study or has penetrated into the underlying layer for a given beam voltage. This is crucial as a measurement performed where the beam has penetrated into the under layer (and without use of the layers analysis software) will result in errors in the composition. An example simulation of a 5 keV electron beam probing 100 nm of GaN on sapphire (Al_2O_3) is shown in Figure 3.8(a). The beam penetrates into the underlying sapphire with 90 % of the energy deposited within approximately 100 nm as shown in Figure 3.8(b).

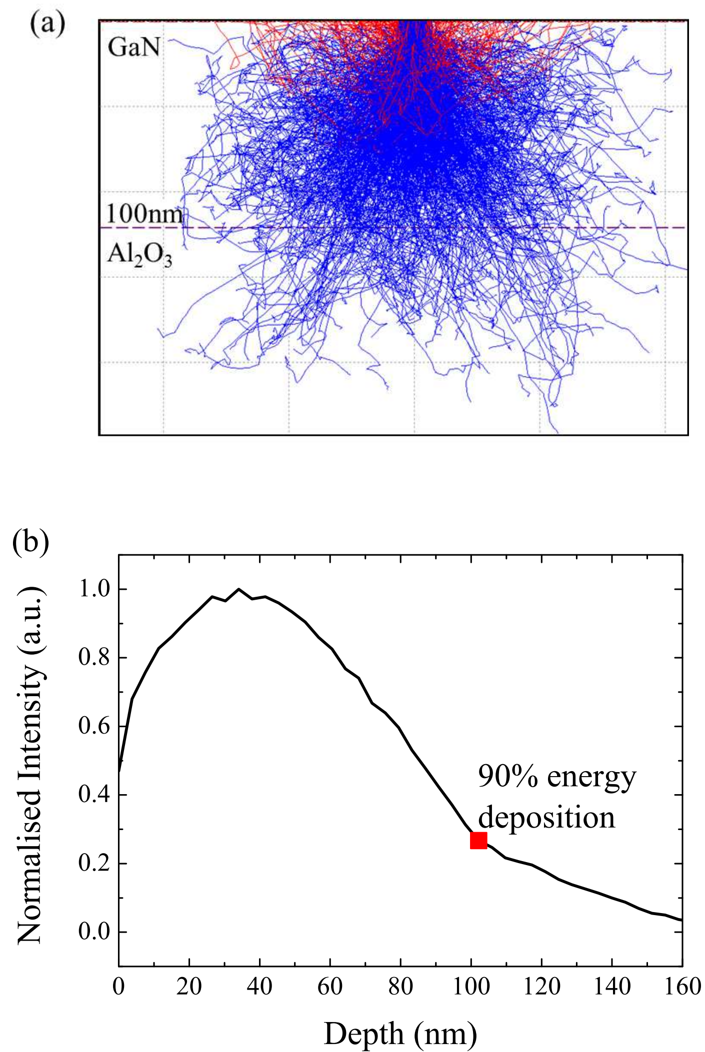

Figure 3.8: (a) Electron trajectory simulation of a 5 keV beam penetrating 100 nm of GaN on sapphire. (b) 90 % energy deposited within approximately 100 nm.

3.4.2 Rutherford Backscattering Spectrometry, X-ray Diffraction and Atomic Force Microscopy

Rutherford backscattering spectrometry (RBS) is another widely used analysis technique for compositional determination and depth profiling of individual elements within thin film materials. This technique uses a high energy collimated beam of ions (MeV range) to bombard a target or sample in order to produce elastic collisions with nuclei of the constituent atoms [101]. In this work the beam of ions are He^+ but often lithium ions and protons are used. The ions that are backscattered are detected using an energy sensitive solid state detector. The position of the detector is important for optimum detection of the backscattered ions and for varying the type of information yielded by the measurement. A large angle is used for composition and depth profiling whereas a small grazing angle allows for structural measurements such as minimum yield.

Unlike WDX, RBS does not require standards as the composition (and thickness) is determined from the direct result of the intensity of the backscattered He^+ ions at different energies. Heavy elements such as In will result in the backscattered ions having higher energy compared to lighter elements such as Al. The depth at which the ions are backscattered will also influence the detected signal as ions that are backscattered further into the sample will result in energy loss on escape. This results in an energy distribution with varying intensities as shown in Figure 3.9. A simulated fitting routine is used to fit the spectrum in order to determine the composition and thickness of the layer under study as illustrated by the red line in Figure 3.9 [102]. The thickness value requires a known density, therefore a source of error can occur in the assumptions of the layer density [103]. The RBS measurements are performed by collaborators Katharina Lorenz, Eduardo Alves and Jorge Sabino at IPFN, Instituto Superior Técnico, Portugal, and the fitting routine used is 'NDF' code [104].

RBS can also be used for structural analysis of samples through minimum yield measurements [35]. With the detector positioned parallel with respect to a chosen crystal plane of the sample the collimated ion beam can be used to create channelling effects. The atoms that are displaced from the lattice plane will cause the He^+ ions to be backscattered increasing the signal. The signal generated from this is known as an aligned spectrum and the signal generated

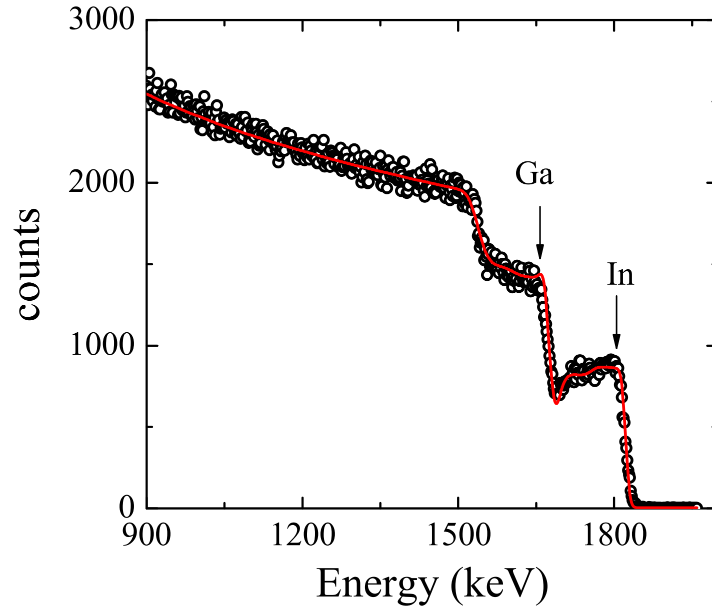

Figure 3.9: Example of an RBS spectrum using a 2 MeV He^+ ion beam to probe an InGaN layer. The elements at the surface are indicated by the arrows.

from an RBS measurement which is not aligned to a specific crystal plane is known as a random spectrum. The minimum yield is calculated as the ratio of the aligned counts to the random counts (Equation 3.9) over the same energy range (i.e. each element) within the spectra as shown for Ga and In in Figure 3.10. The more defects a sample has the higher aligned counts which results in an increased minimum yield value.

$$\chi_{min} = I_{aligned}/I_{random} \tag{3.9}$$

X-ray diffraction (XRD) is another widely used technique for material characterisation and is measured using a diffractometer. XRD is commonly used to gain information on composition, thickness, and material structure [105]. This technique is non-destructive as it uses x-rays (usually Cu K_α) to probe the surface of the material under study. The Cu K_α x-ray source is generated by bombarding a Cu target with electrons in an evacuated tube. The x-rays that are diffracted from the material are measured by a detector. Constructive interference occurs

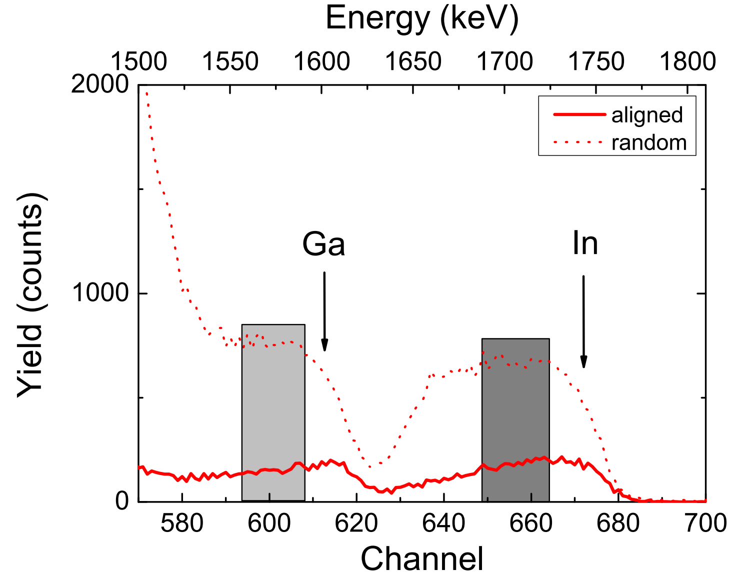

Figure 3.10: Example of aligned and random spectra for Ga and In used for minimum yield calculations. The energy range regions are shown in grey.

when Bragg's law (Equation 3.7) is satisfied and the crystal lattice plane spacing is equal to $n\lambda$ as shown in Figure 3.11(a). For XRD measurements the sample is placed on a goniometer. Both the sample and detector have variable positions in order to scan and measure angle 2θ (Figure 3.11(b)). When the sample is positioned with the source and detector at the same angle with respect to the sample surface (i.e when 2θ=2ω) it is known as a symmetric reflection. This allows c lattice parameter, composition and thickness information to be gained. When the sample is tilted (i.e when $2\theta \neq 2\omega$) this is an asymmetric reflection which provides both lattice parameter (a and c) and relaxation information for hetero-layer samples [106]. This reflection allows reciprocal space maps to be obtained.

Several scanning modes are available to gain particular information about the sample. In this work the scanning mode used is the $\omega - 2\theta$ scan for both symmetric and asymmetric geometries. An example of an $\omega - 2\theta$ scan is shown in Figure 3.12 for InAlGaN epilayer on thick GaN. The sharp peak around 17.15° arises from the thick GaN underlayer and the broad peak around 17.65° arises from the InAlGaN epilayer. The fringes across the scan are known as Pendellösung fringes with the spacing between them relating to the layer thickness. The thickness and

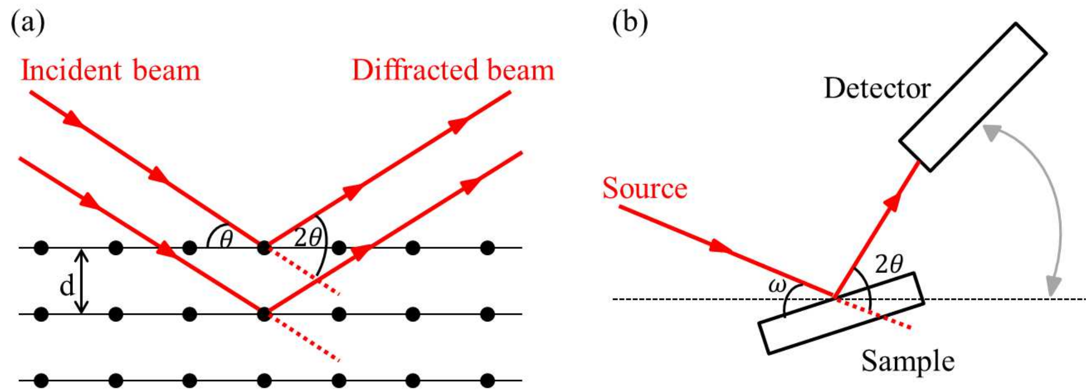

Figure 3.11: (a) Schematic of x-ray diffraction with the diffracted beam satisfying Bragg's law. (b) Geometry of source, sample and detector showing variation in positions for sample and detector.

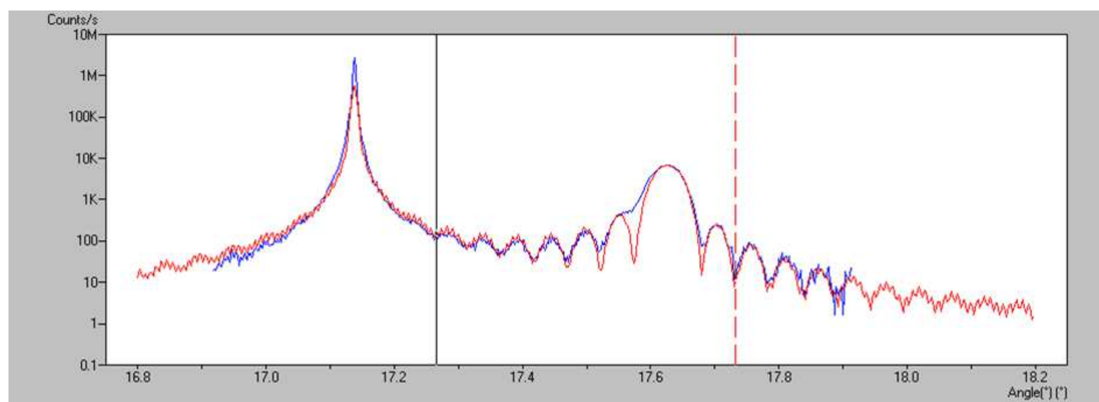

Figure 3.12: A high resolution [0002] $\omega - 2\theta$ XRD scan of an InAlGaN layer on thick GaN showing measured (blue line) and fitted (red line) data. The sharp peak represents the GaN and the broad peak is from the InAlGaN layer.

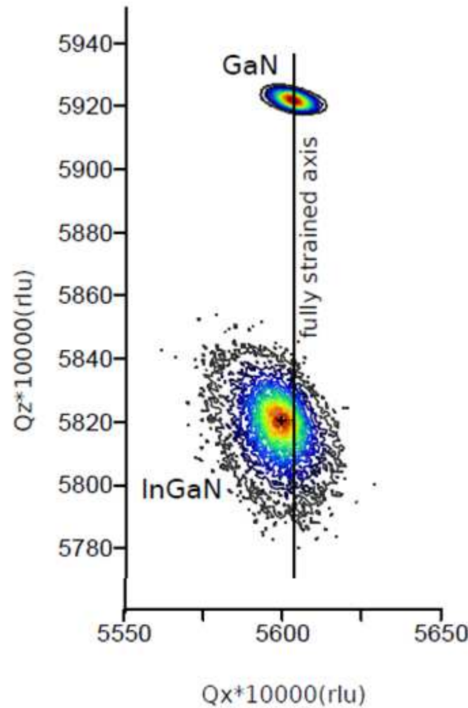

Figure 3.13: Reciprocal space map of an InGaN epilayer on GaN showing the GaN and InGaN satellites. This map shows the InGaN layer lying close to the fully strained axis illustrating there is very little strain. The fully relaxed axis (not shown) extends from the GaN satellite at a calculated angle w.r.t. the fully strained axis.

composition values are determined by varying these parameters to fit the peak positions and fringe spacing using x-ray simulation software. The strain state can also be varied to return the optimum fit, giving also the c lattice parameter value.

To obtain reciprocal space maps (RSMs) several $\omega - 2\theta$ scans are taken at varying ω angles to build up the RSM intensity image. An example RSM of an InGaN epilayer on GaN is shown in Figure 3.13 with the corresponding InGaN and GaN satellites indicated. The fully strained axis is also displayed in the figure indicating in this case a small degree of lattice mismatch between the two layers. The position of the satellites relative to the fully strained and fully relaxed axes in the RSM show the degree of strain. The fully relaxed axis lies at an angle with respect to the fully strained axis (not shown in Figure). The a and c lattice

parameters for each of the layers can be calculated from the Q_x and $Q_y(Q_z)$ values by using Equations 3.10 and 3.11. Q_x and Q_y are the RSM co-ordinates of the corresponding satellite of each layer (e.g. InGaN and GaN), λ is the wavelength of the x-rays (1.54 Å for Cu) and h and l are the Miller indices of the scan. The amount of strain and whether the layer is under tensile or compressive strain can be determined by using Equations 3.12 and 3.13. Subscript x represents the measured or calculated value and subscript 0 is the strain free value. A positive (negative) value indicates tensile (compressive) strain. The XRD measurements were carried out by collaborators at both University of Cambridge and Tyndall National Institute, Cork.

$$a = \frac{1}{Q_x}\frac{\lambda}{\sqrt{3}}h \tag{3.10}$$

$$c = \frac{1}{Q_y}\frac{\lambda}{2}l \tag{3.11}$$

$$\epsilon_a = \frac{a_x - a_0}{a_0} \tag{3.12}$$

$$\epsilon_c = \frac{c_x - c_0}{c_0} \tag{3.13}$$

Atomic force microscopy (AFM) is another characterisation tool used for studying materials. It is a surface imaging technique which provides information on sample quality, such as surface roughness, grain boundaries and defects. This type of microscopy uses a sharp tip on a cantilever to scan over a samples surface; when the tip comes into close proximity of the surface it deflects due to the forces between the tip and surface. The deflections, both vertically and laterally, of the cantilever are monitored through the use of reflected laser light and are detected using a position sensitive photodetector. Scanning the tip over an area allows for a 3D data set to be obtained. The z-axis, related to the deflections from the sample surface, is usually given as a scale bar on the AFM image. The resolution of the AFM is limited by the size of the tip, which is on the orders of nanometers laterally and angstroms vertically, giving it the ability to resolve on an atomic scale [107]. Several different modes of operation are available in an AFM including contact mode, tapping mode and non-contact mode. The AFM images acquired in this thesis are taken under tapping mode conditions. In

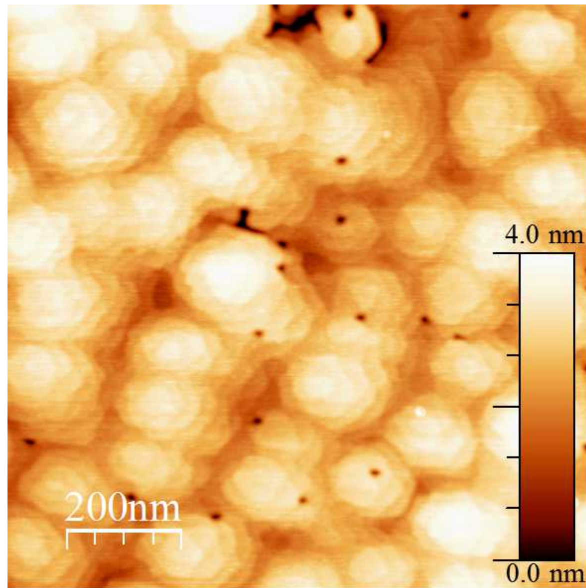

Figure 3.14: An example AFM image of an InAlN layer showing hillock structure. The colour scale gives the vertical height in nanometres. *Image taken at Tyndall National Institute.*

tapping mode the cantilever oscillates up and down, and when it comes in close contact with the surface the amplitude of the oscillation reduces. This limits the contact between the tip and the surface, reducing damage to both the tip and the surface when compared to contact mode. An example of an AFM image is shown in Figure 3.14. The AFM images were taken by collaborators at both University of Cambridge and Tyndall National Institute, Cork.

3.5 Optical Characterisation Techniques

This section introduces the optical characterisation techniques used throughout this thesis. These include cathodoluminescence (CL) and photoluminescence (PL), both of which are used as mapping techniques to provide additional spatial luminescence information of the material under study. The following subsections will give details on the set ups used for the CL and PL experiments.

3.5.1 Cathodoluminescence

Cathodoluminescence (CL) is the emission of photons after excitation by a high energy electron beam, and is one of the inelastic scattering mechanisms occurring in an SEM. This makes it very useful as a micro-characterisation tool for luminescent materials such as semiconductors and insulators as it can be measured simultaneously with other products of electron bombardment. The impinging high energy electron beam is of several orders of magnitude greater than the bandgap energy of the luminescent material so photons can be produced from UV to infrared regions of the electromagnetic spectrum. This makes it useful for characterising a wide range of materials unlike photoluminescence which uses selective photoexcitation.

CL occurs due to electron beam excitation promoting electrons from the valence band to the conduction band, after first losing energy through impact ionisation. This creates electron-hole pairs which leads to radiative recombination, producing photons characteristic of the luminescent material [91]. The generation volume follows similar behaviour to the penetration volume as described in section 3.3 in that it is dependent on the atomic number. The density of carriers generated within the excitation volume can be of several orders of magnitude greater than those generated using PL. For example a single 20 keV electron can generate thousands of electron-hole pairs whereas a photon can only generate one electron-hole pair. As the excitation volume increases with increasing beam energy the generation rate reduces nonlinearly. This can be expressed by the depth-dose function determined by Everhart and Hoff (Equation 3.14), where y is the depth divided by the Gruen range ($y = z/R_e$) [108].

$$g(z) = 0.60 + 6.21y - 12.40y^2 + 5.69y^3 \tag{3.14}$$

The depth-dose function represents the number of electron-hole pairs generated by one electron of energy E per unit depth and per unit time. An example of the depth-dose curves for GaN is shown in Figure 3.15 for beam voltages 3 keV, 5 keV, 10 keV and 20 keV. The generated electron-hole pairs can diffuse before recombining to produce photons. This results in a larger CL signal volume compared to the generation volume. Not all of this signal is emitted from the semiconductor material due to reflection and absorption within the sample.

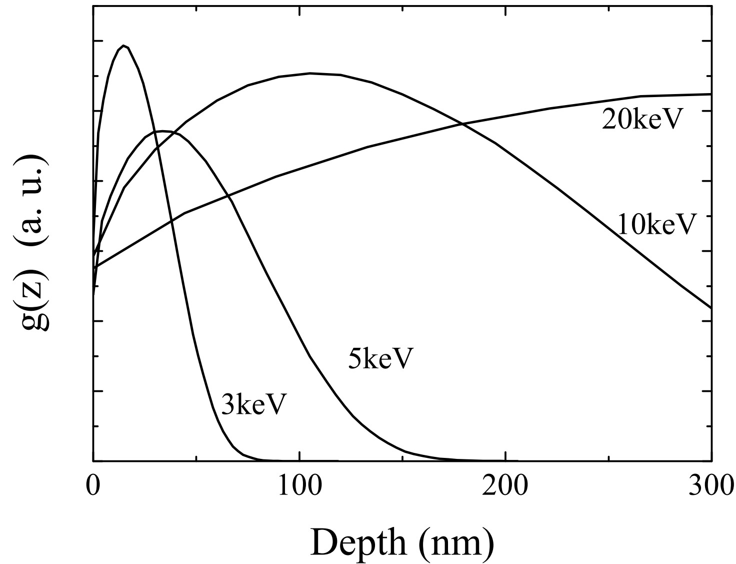

Figure 3.15: An example of the depth-dose curves for GaN for varying beam energy.

Other loss mechanisms and altering effects include non-radiative recombination, defects, presence of electric fields and temperature.

Understanding the penetration and generation volumes as well as beam spot size and carrier diffusion is important for CL analysis, especially for high resolution CL mapping. High resolution CL can be achieved down to the nm scale by using low beam currents and low beam voltages [109, 110]. As was discussed in section 3.3 a high beam voltage results in larger penetration volumes. This will reduce the resolution due to lateral spreading of the beam within the sample [111]. An example of this increase in penetration volume and lateral spread with increasing beam voltage was illustrated by the Monte Carlo simulations within GaN in Figure 3.5.

Both the EPMA and the FEGSEM have been modified in order to perform room temperature CL mapping [112, 109]. In the EPMA the CL emission follows the same path as the optical microscope which is coaxial with the electron beam through a light-collecting reflecting objective. The light then hits a mirror and is focused to an image plane at the entrance slit of an attached Oriel Instruments 1/8m spectrograph. An Andor charge-coupled device (CCD) (model no. DU420-

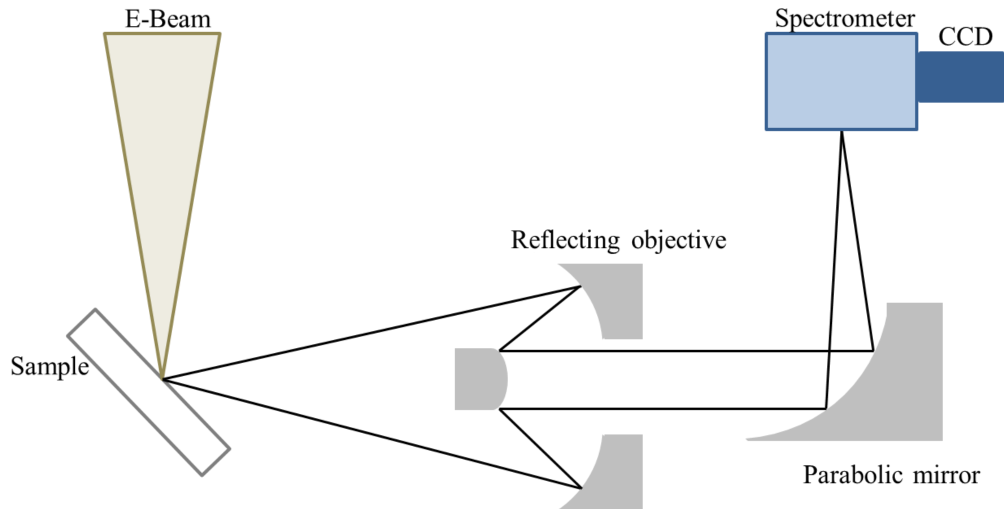

Figure 3.16: Schematic of CL system on the FEGSEMs.

BU) is used for detection as shown in Figure 3.6. The entry slit and diffraction grating on the spectrometer can be changed for increased flexibility in detection. The slits used with this spectrograph for both CL and PL experiments include 25μm, 50μm, and 100μm. The gratings used are 400 l/mm, 1200 l/mm, and 2400 l/mm ruled gratings with 350 nm and 500 nm blazing.

The CL system on the FEGSEMs differs from that on the EPMA, with the light collection at right angles to the incoming electron beam path as shown in Figure 3.16 [109]. The sample is positioned on the 45° holder and the light emission is collected by the reflecting objective. It is then focused at the spectrometer entrance by the parabolic mirror. A quartz window is put in place after the reflecting objective to ensure the vacuum is contained. The spectrograph used is the same as the EPMA set up but the CCD is an Andor Newton EM (Electron Multiplying) (model no. DU970N-UVB) which is capable of detecting high energy (up to ~6.5eV) UV emission due to a reduction in noise for small signals.

The response curves for each of the CCDs used for the CL detection are presented in Figure 3.17. All of the CCDs used for CL (and PL) are silicon based covering the visible spectrum and parts of the UV and infrared. The CCDs on the SEMs are back-illuminated design resulting in high peak quantum efficiencies.

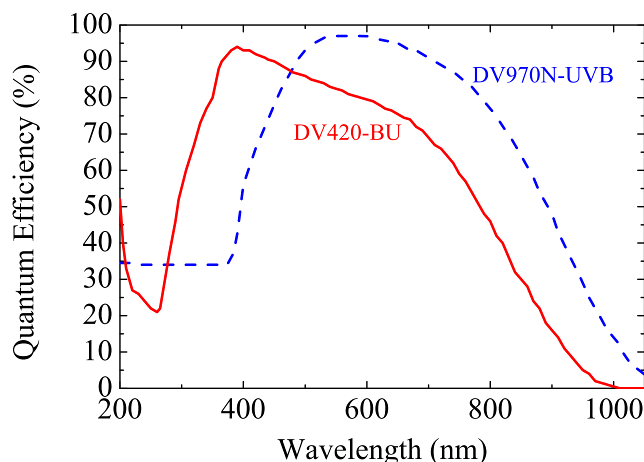

Figure 3.17: Response curves for each of the CCDs used for CL experiments throughout this thesis. DV970N-UVB used on the ESEM and DV420-BU used on the EPMA.

The CCD response has been applied to the CL spectra in Chapter 4, taken on the EPMA using DV420-BU CCD, as there is a variation in quantum efficiency (QE) over the wide range of luminescence measured. For the CL spectra presented in Chapters 5 and 6 taken on the ESEM using DV970N-UVB CCD the response has not been applied due to the wavelength range being studied. The luminescence is all in the range 270-400 nm for the samples studied in these Chapters and the response has little or no change in the region 200–400 nm as shown in Figure 3.17.

CL mapping is achieved by scanning the beam or the stage and collecting the light at each step over the mapped area (same principle as discussed for the WDX mapping). An image is produced as the light collection at each step relates to a pixel. A photomultiplier and detector set up results in a panchromatic image of emission intensity, and a monochromator allows an intensity image of single wavelength to be produced. By using a spectrometer and a 1024-channel CCD (1600-channel for EMCCD) more information can be stored and hyperspectral imaging can be achieved. This means that an individual spectrum can be recorded for each pixel as the beam is scanned over the designated area of a particular sample. This allows a 3D data set to build up of x, y, and λ as illustrated in Figure 3.18.

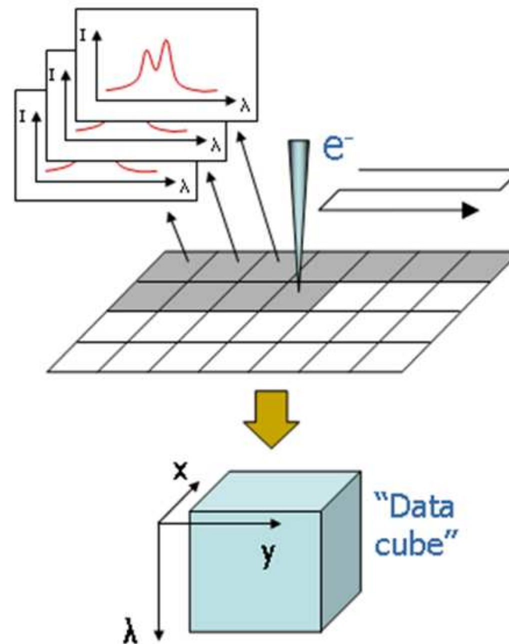

Figure 3.18: Schematic of hyperspectral imaging. *Images courtesy of Dr. Paul R. Edwards.*

From this hyperspectral CL image parameters such as integrated and peak intensity, centroid, peak emission energy, and full width half maximum (FWHM) can be analysed. An example of a CL integrated intensity and centroid map of an InGaN epilayer sample is shown in Figures 3.19(a) and 3.19(b). The spectrum corresponding to the highlighted pixel in both maps is also presented in Figure 3.19(c). Analysis software known as *Cathodoluminescence Hyperspectral Imaging and Manipulation Program* (*CHIMP*) created and developed by Dr. Paul R. Edwards controls the image acquisition process, and is also used for analysis such as peak fitting, parameter correlations, and statistics. Performing this type of CL mapping in conjunction with SE imaging and WDX mapping allows these parameters to be related to surface position and composition.

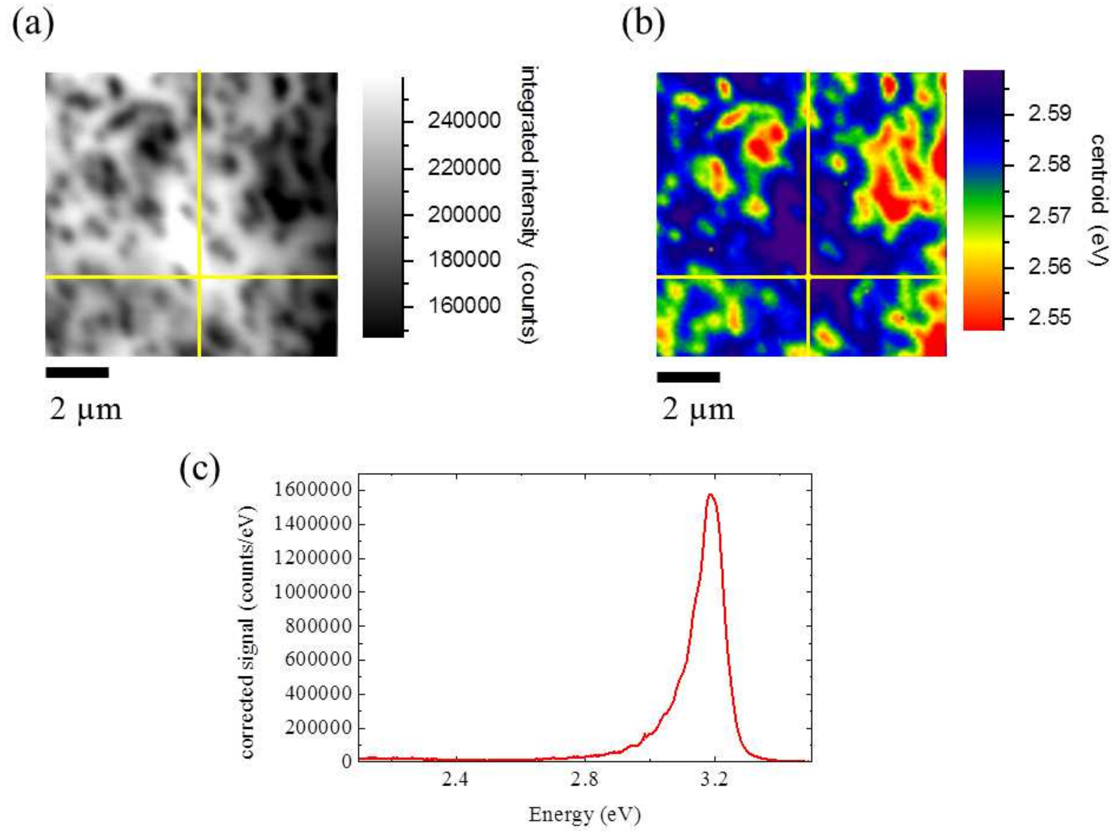

Figure 3.19: Example of a CL (a) integrated intensity and (b) centroid map with (c) spectrum, corresponding to the highlighted pixel in both maps, of an InGaN epilayer.

3.5.2 Photoluminescence

Photoluminescence is the emission of photons after photoexcitation. In semiconductors the excitation source energy needs to be greater than the bandgap of the material in order for photoluminescence to occur. This excitation provides enough energy to excite a valence band electron to the conduction band resulting in an electron-hole pair which after some time recombine to produce photons with energy equal to the bandgap energy. Other radiative and non-radiative processes can also occur after the excitation of an electron as was discussed in Chapter 2. An emission spectrum of these radiative processes is generated with varying

intensities over an energy range defined by the spectrometer. This ability for selective photoexcitation makes it a useful spectroscopic technique for studying semiconductor materials, for example it has the ability to excite a quantum well (QW) without exciting the barriers.

Probing such materials with light can result in photons being absorbed as they propagate through the material. This is both material and photon energy dependent, with each semiconductor having an associated absorption coefficient which varies with photon energy [113]. The intensity of the incident light decreases exponentially with depth through the material as described by the Beer-Lambert law. This is illustrated in Equation 3.15 where I_{v0} is the initial photon intensity, α is the absorption coefficient, and x is the distance. A high absorption coefficient results in a rapid decrease in intensity. For example a 325 nm laser probing GaN, with an absorption coefficient of $\sim 1.2\times10^5$ cm^{-1} [114], results in 90 % of the initial intensity being absorbed within ~200 nm.

$$I_v(x) = I_{v0}e^{-\alpha x} \tag{3.15}$$

The PL set up used for work within this thesis is illustrated by the schematic diagram in Figure 3.20. This home built system adopts a microscope design allowing the sample surface to be imaged. The Kimmon Koha 17 mW 325 nm HeCd laser (model no. IK3151R-E) (or the CrystaLaser 120 mW 405 nm diode laser) is guided through a periscope by mirrors towards a Thorlabs UV 20× beam expander (model no. ELU-25-20X-351). The laser light passes through a Pellin Broca prism before the periscope in order to remove any unwanted plasma lines. The beam expander is used to help obtain a spot size of <2μm by filling the objective. The expanded beam hits a dichroic filter which reflects the laser light towards a Newport 15× NA 0.4 reflecting objective while still allowing longer wavelength light to pass through towards the camera. The expanded beam fills the entrance aperture of the reflecting objective which focuses the light to a small spot on the sample surface. The light emission from the sample is collected by the same objective and focused to the entrance of an Oriel Instruments MS125 1/8m spectrograph (same as EPMA-CL system) and Andor CCD (model no. DV420-OE) using a lens, passing through a longpass filter to remove the unwanted laser line from the detected spectrum. The dichroic and longpass filters are

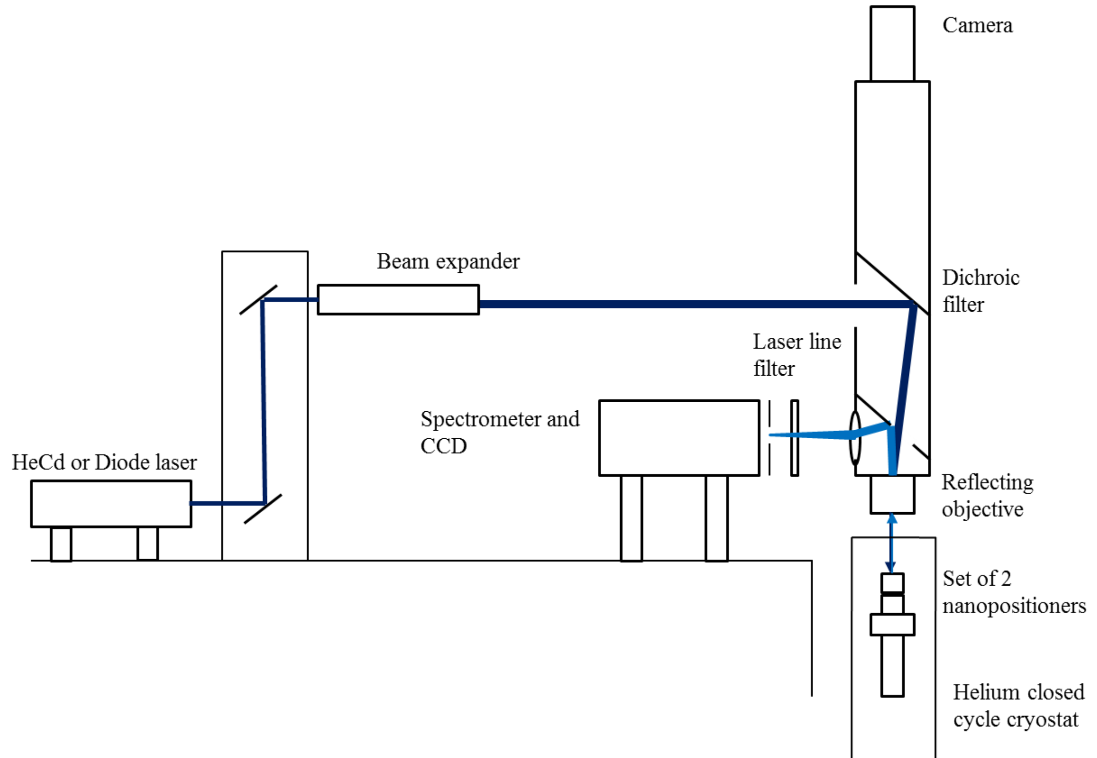

Figure 3.20: Schematic of the side view of the PL set up showing the microscope design. Both HeCd and diode lasers can be used in this set up by the input of a magnetic mirror.

interchangeable depending on excitation source used.

The full system response for the set up using the HeCd laser is shown in Figure 3.21, with appropriate longpass filter, spectrometer grating option 1200 l/mm (350 nm blazed) and 25 µm slit. This system response takes into account all the collection optics including the reflecting objective, lenses, filters, spectrometer and CCD. It is used to calibrate all the point PL spectra taken under these conditions throughout this thesis. The response spectrum was determined by using a 3.5V/200mA tungsten filament bulb. The bulb was measured using an integrating sphere to obtain the colour temperature (CCT). From this a blackbody curve, mimicking that of the bulb, was generated to cover the wavelength range of the detector on the PL system. This blackbody spectrum, equivalent to that of the tungsten bulb, was then compared with the spectrum of the bulb measured on the PL system to produce the response.

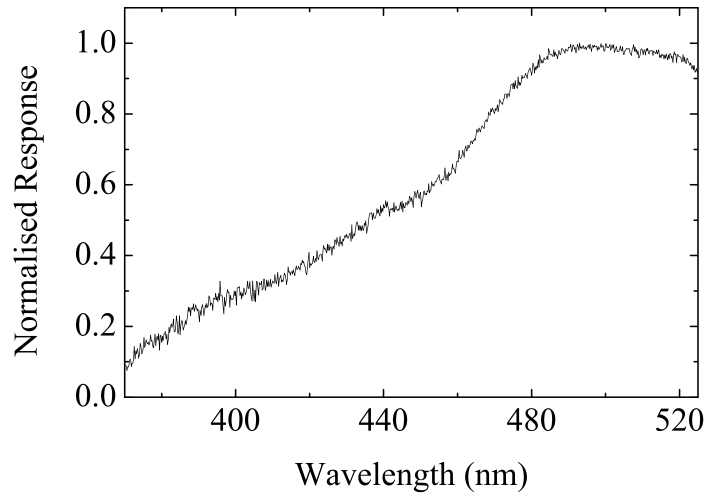

Figure 3.21: Full system response of the PL set up shown in Figure 3.20 for grating option 1200 l/mm, 350 nm blazed and 25 μm slit. Spectrometer, CCD, filters and lenses all accounted for.

The system also has the advantage of performing PL mapping due to the addition of a pair of Attocube ANPx101 nanopositioners. These act as a scanning stage in which the sample can be moved. These are controlled through an adapted version of the CHIMP software that is used for CL mapping. More details of PL mapping will be given in Chapter 7. Low temperature PL can also be performed by the aid of the closed-cycle helium cryostat. The sample (and positioners) are located at the end of a coldhead within the cryostat, which is under high vacuum. The temperature can be cooled down to ∼18K.

Chapter 4

Composition and Luminescence Studies of InGaN epilayers

4.1 Introduction

Research on III-nitride materials for use in optoelectronic devices has advanced in recent years, with the emergence of high efficiency blue light-emitting diodes (LEDs) and laser diodes (LDs), but achieving highly efficient nitride-based green LEDs still poses problems. The most common alloy used for achieving green emission is $In_xGa_{1-x}N$ (henceforth referred to as InGaN), but the drop in efficiency with increasing InN fraction is a problem and is still not fully understood. It is well known that the reduction in growth temperature allows the increase of the InN fraction within the alloy, shifting the wavelength into the green [115], but the ammonia used to provide nitrogen during growth is difficult to dissociate at these lower temperatures, resulting in a reduced InGaN layer quality. Other issues to consider that could impact the layer quality when lowering the growth temperature are low surface mobility, impurity incorporation and structural defects. Incorporating large InN fractions can also lead to strain-induced phase separation producing layers with spatially inhomogeneous luminescence [116]. The challenge still remains to obtain high InN fractions within InGaN alloys while maintaining sample quality and luminescence homogeneity, especially for relatively thick layers (>50 nm). The addition of small amounts of hydrogen carrier gas during growth has been seen to improve the sample quality but at the expense of a

reduction in the InN incorporation [117, 118, 119, 120].

This chapter describes the characterisation of a set of 160-nm thick InGaN epilayers in order to determine the effect of adding small amounts of hydrogen to the gas flow, during growth at lower temperatures, on the composition and luminescence properties of the material. The composition was measured using wavelength dispersive x-ray (WDX) spectroscopy and compared with x-ray diffraction (XRD) data measured at the University of Cambridge and Rutherford backscattering spectrometry (RBS) data from IPFN, Intituto Superior Técnico, Portugal. The luminescence properties were explored using cathodoluminescence (CL) hyperspectral imaging, in which the sample is rastered under an electron beam using a precision scanning stage and the emission spectrum recorded at each point to build up a multidimensional luminescence dataset (see Section 3.5.1) [111, 121]. In addition secondary electron (SE) and atomic force microscopy (AFM) imaging was performed to investigate surface quality. The AFM images were measured at the University of Cambridge.

4.2 Sample and Experimental Details

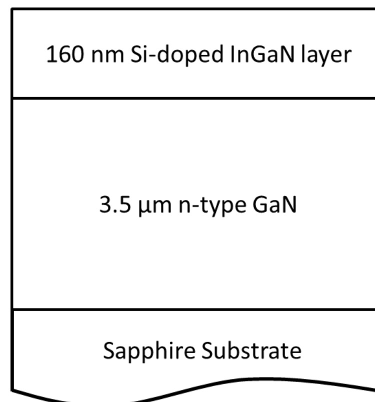

Figure 4.1: Simple schematic of InGaN epilayer on thick GaN.

Sample	Growth Temperature (°C)	Hydrogen Flow Rate (sccm)
A00	750	0
B00	725	0
C00	710	0
C50	710	50
C100	710	100
D00	680	0
D100	680	100
D200	680	200

Table 4.1: Growth temperature and hydrogen carrier gas flow rate for each InGaN sample.

A series of thick InGaN epilayer samples were grown on c-plane GaN/sapphire substrates (Figure 4.1) using a Thomas Swan 6×2-inch close-coupled showerhead metalorganic vapour phase epitaxy (MOVPE) reactor by Menno Kappers at the University of Cambridge. Trimethylindium (TMIn), trimethylgallium (TMGa) and ammonia (NH_3) were used as source materials. The GaN epilayer templates were grown 3.5 μm thick on c-plane sapphire at 1020°C. Further information on template growth can be found elsewhere [122]. The threading dislocation density of the GaN template was about 5×10^8 cm^{-2} as measured by counting the pit density in AFM images after the sample surface was subjected to treatment with silane and ammonia [123]. For the InGaN deposition the main carrier gas used was nitrogen with small quantities of hydrogen (up to 200 sccm (standard cubic centimeters)) added for certain layers, while using TMIn flow of 23.0 μmol/min, a TMGa flow of 11.2 μmol/min and an ammonia flow of 446 mmol/min at a reactor pressure of 300 Torr. The samples were grown with an InGaN layer of nominal thickness 160 nm and with target InN fractions varying from 5 % to 20 %, which was achieved by varying growth temperature and hydrogen flow rate, as shown in Table 4.1. The temperatures quoted are the susceptor temperature measured using a pyrometer calibrated against a black body source. Based on the layer thicknesses determined by XRD and RBS, the InGaN growth rate varied between approximately 1.6 and 1.9 nm/min depending on the alloy composition.

In this work the WDX composition and CL measurements were carried out

on a modified Cameca SX100 electron probe micro-analyser (EPMA) with an attached spectrograph as was described in Chapter 3. The XRD data was measured using a Philips X'Pert MRD diffractometer. The RBS measurements were performed using 1.5 and 2 MeV He^+ ions and both spectra were fitted simultaneously to a two-layer model using the RBS analysis code "NDF" [124]. AFM measurements were performed in tapping mode using a Digital Instruments Nanoscope Dimension 3100 microscope, and the data were analysed using the WSXM software package [125].

4.3 Surface Quality

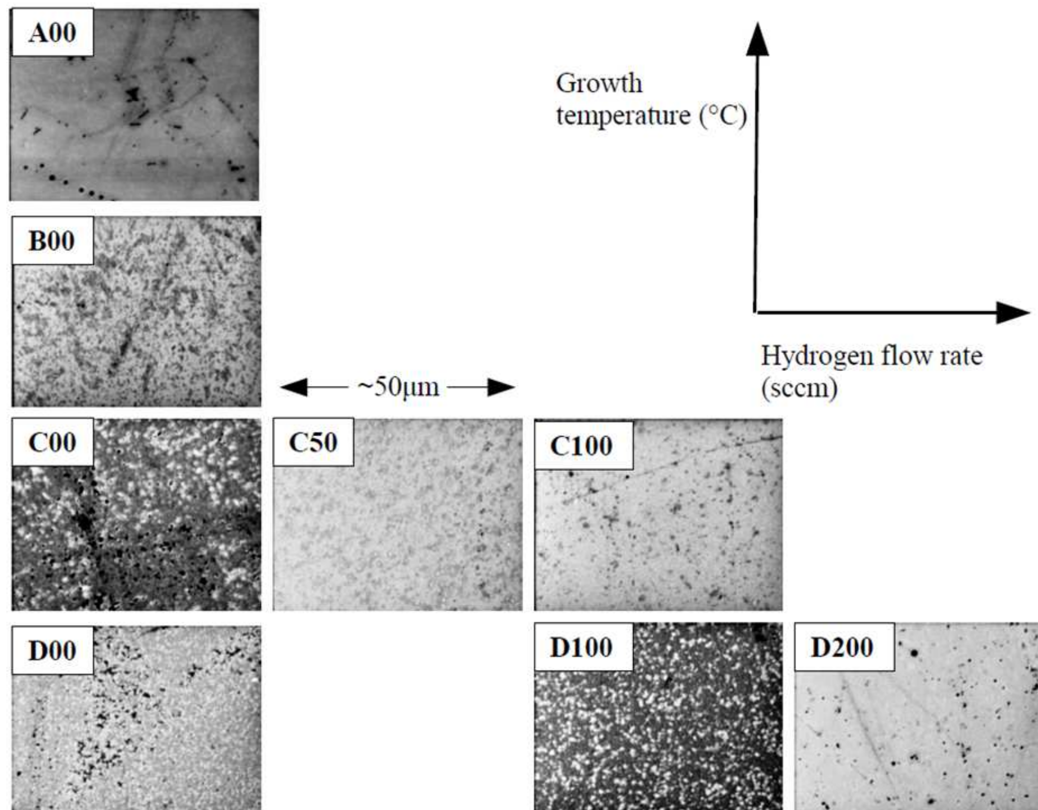

Figure 4.2: Secondary electron images showing variations in surface quality with change in growth temperature and hydrogen flow rate, indicated by the key in the top right of the figure.

The surface quality of each of the InGaN samples were investigated to see how the change in growth parameters influences the resultant material quality. Secondary electron (SE) images were taken using a Cameca SX100 electron probe micro-analyser (EPMA) to gain information on the changes in surface quality over the sample set. SE images of 50 μm wide regions are shown in Figure 4.2, and illustrate that the surface quality worsens with decreasing growth temperature but improves with increasing hydrogen flow rate for samples grown at the same temperature. This is indicated by the key in the top right of the figure. Looking at the SE images we can conclude that the outer diagonal (A00, C100 and D200) represents the better quality samples with fewer surface imperfections across the image. Samples C00, D00 and D100 are of lower quality with large variations in contrast across the image which gives an indication of surface roughening. For samples C00 and D00 in particular the reduction in the temperature has had severe effects on the sample quality with large holes appearing on the surface. These images are compared with the results of higher resolution atomic force microscopy (AFM) images measured at the University of Cambridge, as shown in Figure 4.3, to gain further insight into roughness of the sample surfaces.

The AFM images illustrate the evolution of morphology with temperature and added hydrogen flow rate used for the InGaN epilayer growth. The InGaN samples A00 and B00 show smooth surface morphology in the standard hydrogen free environment as shown in Figure 4.3 (a) and (b). The black surface pits within the images are V-defects and their density of approximately 4×10^{8} cm^{-2} in sample A00 corresponds to the threading defect density in the GaN template underneath. The additional pits seen in the surface of B00 that are arranged in a circular fashion may be trench defects which originate from inversion domains bounded by stacking mismatch boundaries formed at the GaN/InGaN interface [126, 127]. The surface morphology of the InGaN epilayers becomes worse when the InN content is increased by reducing the growth temperature. This is indicated by the variation in the AFM height scales for each of the images which are presented in Table 4.2. Figure 4.3 (c) of sample C00 shows additional island formation while the surface of D00 in Figure 4.3 (d) is covered with small round islands and mounds. Adding hydrogen during the InGaN growth at the same growth temperature improves the surface significantly, e.g. compare C100 and C50 with C00 or D200 and D100 with D00. The large clusters of islands change with added

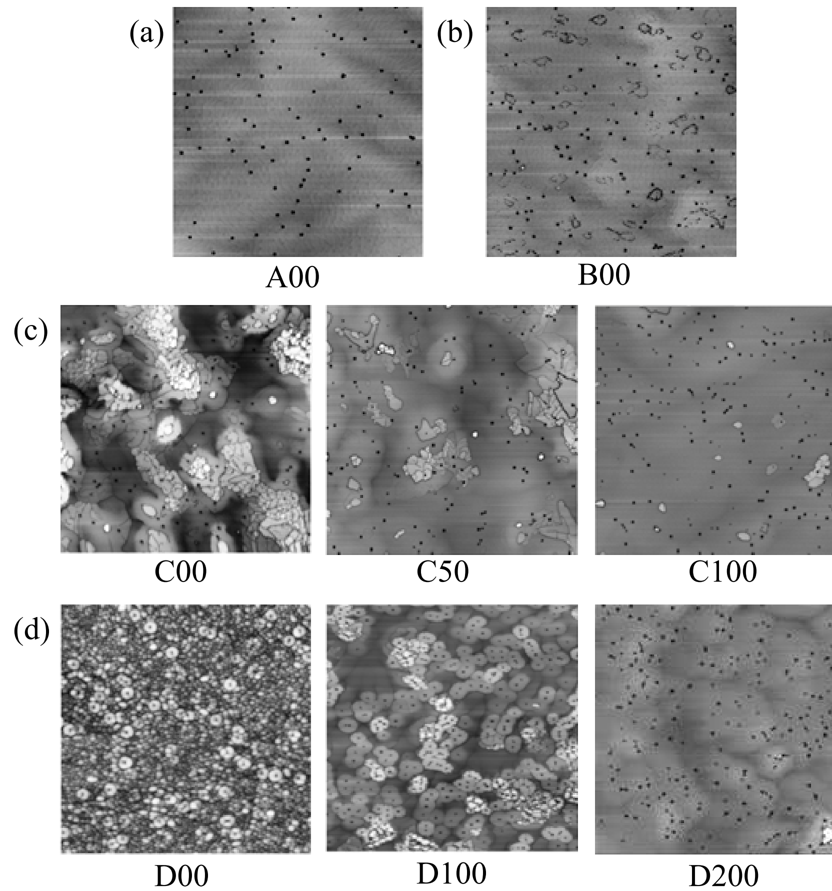

Figure 4.3: AFM images of InGaN epilayers (5 μm x 5 μm) from series A, B, C and D. The scale of each of the images are given in Table 4.2.

hydrogen flow to far fewer and smaller inclusions on the surface. The transition from a poor morphology of samples C00, D00 and D100 to the much improved surface quality of samples C100 and D200 is the same as seen in the SEM images in Figure 4.2.

Sample	AFM Scale (nm)
A00	50
B00	50
C00	80
C50	80
C100	80
D00	250
D100	250
D200	80

Table 4.2: AFM image height scales for each of the InGaN epilayer samples shown in Figure 4.3.

4.4 Compositional Characterisation

WDX spectroscopy was performed using the EPMA to obtain the InN composition of each InGaN epilayer sample. A 5 keV electron beam was used in order to contain the excitation volume within the 160 nm top layer while still exciting the In L_α lines. The composition determined by WDX was compared with XRD and RBS data as shown in Figure 4.4. Figure 4.4 displays the known trend of decreasing InN fraction with either increasing growth temperature (labelled D to A) or increasing hydrogen flow rate (labelled 00 to 200 after the equivalent flow rate in sccm). D00 has been omitted from further composition and optical investigations as it has a very weak, broad luminescence most likely due to having a very high InN content (> 30 %).

All three techniques are in agreement with this trend, but the InN fractions measured using XRD are consistently lower than those measured using WDX. This difference is attributed to a compositional gradient through the layer, with the higher InN fraction lying close to the surface. The excitation volume of the 5 keV electron beam within the InGaN layer is less than the XRD sampling volume, with XRD providing more of a bulk measurement [128]; a higher InN fraction nearer the surface will thus disproportionately influence the WDX technique. RBS measurements were performed on two of the samples to test this hypothesis by providing depth-profile information. The RBS spectra for samples

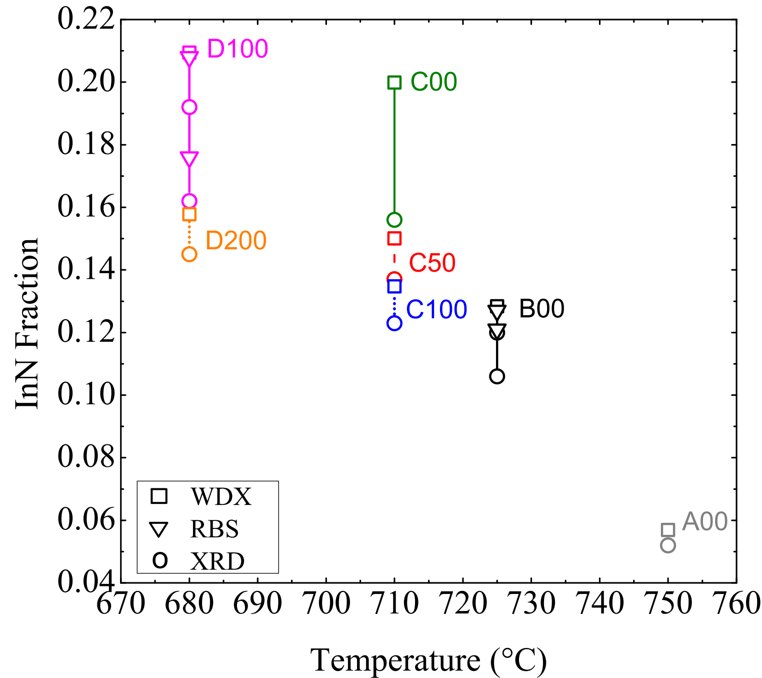

Figure 4.4: Comparison of average InN fraction for each of the InGaN samples grown at different growth temperatures and hydrogen flow rates, measured using WDX and XRD. Additionally, RBS data are shown for B00 and D100. Each technique is defined by a different symbol, and each sample is joined by a different line style. For B00 and D100 the extremes of linear fits to the XRD and RBS data are shown to highlight the compositional gradient through the InGaN layer.

B00 and D100 were each fitted using a two layer model, in which the thickness and composition of two uniform layers was varied. Two ion beam energies of 1.5 MeV and 2 MeV were used to generate 2 spectra, and both resultant spectra were fitted simultaneously to obtain more accurate results. The spectra and fits for sample D100 are shown in Figure 4.5(a). The sharp peak near 1200 keV on the 1.5 MeV spectrum is due to a combination of the Ga and In signals.

The spectra clearly show a reduction in indium counts for both epilayers as the energy reduces, with this negative slope more clearly visible in the magnified portion of the D100 trace shown in Figure 4.5(b). This confirms that there is a variation of InN content with depth within the InGaN layer, with the higher InN composition near the surface. The composition gradients are estimated by fitting the RBS data using a simple approximation of two layers of same thickness but

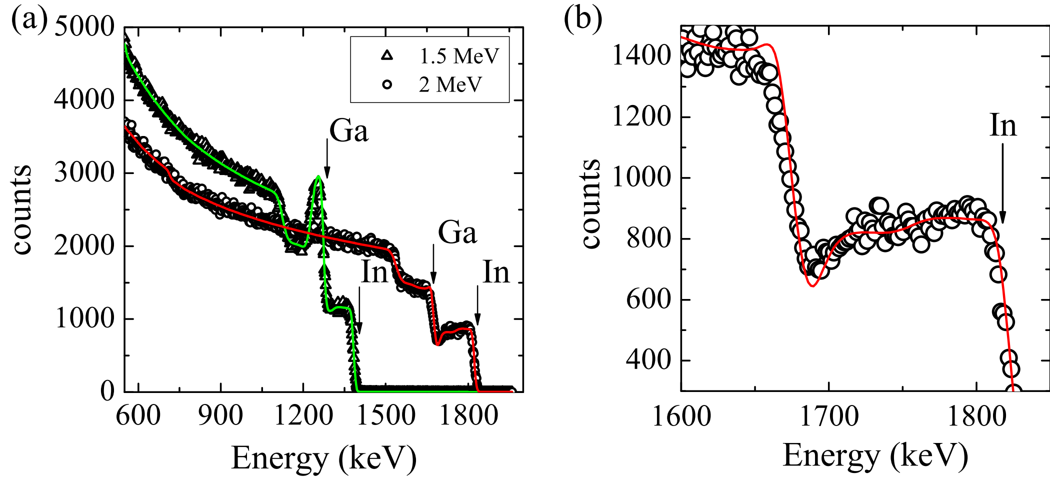

Figure 4.5: (a) RBS spectra of sample D100 measured with 1.5 MeV and 2 MeV He^+ ions and using a two layer model for the fit, indicating an indium compositional change through the InGaN layer. (b) Close up of the 2 MeV spectrum at the indium signal to highlight the gradient and two layer fit.

Sample	WDX InN %	XRD average InN %	RBS InN % (two layer model)	XRD* InN % (linear model)	RBS* InN % (linear model)
A00	5.7	5.2			
B00	12.8	11.5	12.2, 12.5	10.8–12.2	12.1–12.7
C00	20.0	15.6			
C50	15.0	13.7			
C100	13.5	12.3			
D00	31.4	21.0			
D100	21.0	17.8	18.4, 20.0	16.2–19.2	17.6–20.8
D200	15.8	14.5			

Table 4.3: InN composition of each of the InGaN samples determined by WDX and XRD, with additional gradient results from RBS and XRD two layer and linear models.

different InN fractions, as reported in Table 4.3, along with the WDX composition values. Using this RBS result as a guide the XRD measurements were further analysed on samples B00 and D100. Reciprocal space maps (RSMs), as shown in Figure 4.6, revealed broad InGaN peaks relative to the GaN template peaks. The

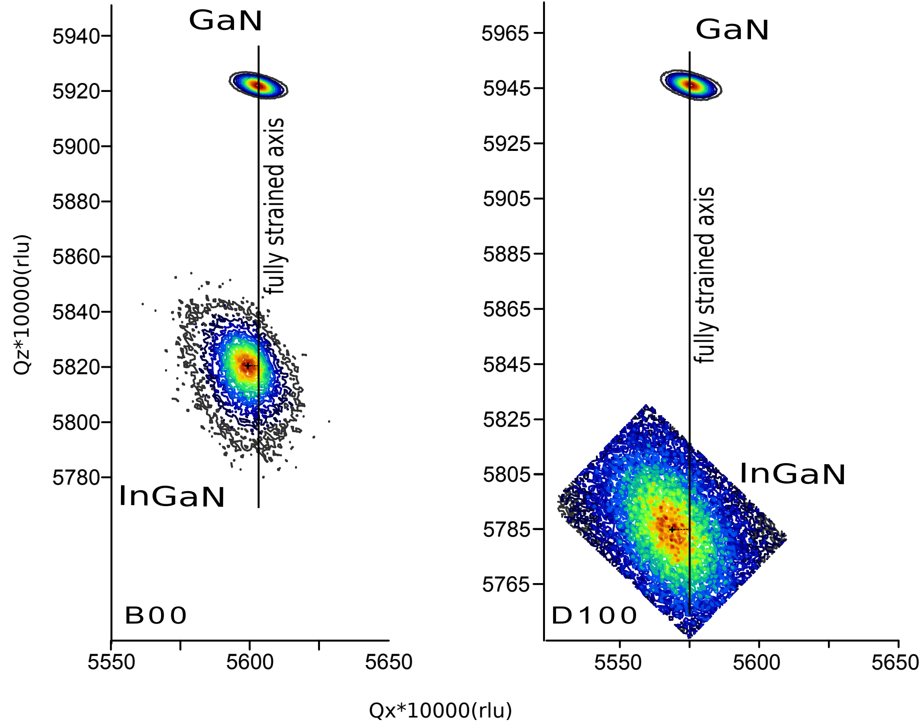

Figure 4.6: Reciprocal space maps around the 204 reflection of samples B00 (left) and D100 (right).

GaN templates are under slight in-plane compressive strain, (-1.6 and -1.7×10^{-3} for B00 and D100, respectively) due to mismatches in thermal expansion during cool down along with differences in GaN template thickness. These strain values, calculated using the a lattice parameter determined from 2θ scans, match the RSM data in Figure 4.6 after the necessary rotation correction to account for small differences in the mounting of the samples. The InGaN peak broadening is greater for sample D100, which has the higher average InN fraction, suggesting a reduced crystal quality. For both samples, the small horizontal shift of the InGaN peak with respect to the GaN peak is indicative of a partial in-plane relaxation, 2 % for sample B00 and 7 % for sample D100, but no clear evidence was found of a relaxation gradient through the film thickness [129, 130]. Thus the XRD model consisted of a single InGaN layer with a constant relaxation value but a linear variation of the InN fraction through the thickness of the film.

The XRD models found an InN gradient covering a change of 1.4 at.% (from 10.8 to 12.2 %) with a partial relaxation of 2 % for sample B00, and an InN

gradient covering a change of 3.0 at.% (from 16.2 to 19.2 %) with a partial relaxation of 7 % for sample D100. In order to make comparison between the XRD and the RBS data, the two-layer model used to interpret the RBS data was transformed into the equivalent linear variation with the weighted average InN fraction as shown in Table 4.3. The average InN fractions determined by XRD are consistently slightly lower than the RBS values: 11.5 % versus 12.4 % for sample B00 and 17.7 % versus 19.2 % for sample D100, respectively, while the change in InN fraction measured by XRD was found to be greater than the calculated RBS linear change for sample B00 (1.4 % compared with 0.6 %) but the results were comparable for sample D100 (3.0 % compared with 3.2 %). The upper and lower InN fractions which correspond to these gradients for both XRD and RBS are presented in Figure 4.4 and Table 4.3. The uncertainties associated with each of the data sets are all approximately 1 % (absolute in x) or less.

In addition to the analysis of the composition as a function of depth WDX spectral mapping was performed on samples B00 and D200 to gain information on elemental distribution within the InGaN layer. The WDX maps for samples B00 and D200 showing the In L_α, Ga L_α and N K_α signals over an area of 10×10 µm are shown in Figures 4.7(a) & (d), 4.7(b) & (e) and 4.7(c) & (f), respectively. All maps of each sample were performed simultaneously using 3 different diffracting crystals (TAP, LPET and PC1) resulting in mapping the exact same area and with the same pixel number and acquistion time (200 ms). From maps 4.7(a) and 4.7(b) a slight compositional inhomogeneity can be seen. A clear inverse correlation between the In and Ga counts is evident around x = 3 µm, y = 4 µm, whereas map 4.7(c) shows the N counts to be more evenly distributed, as expected for a III-N layer. Sample D200 maps reveals improved compositional homogeneity with no clear elemental variation over the mapped area of the In L_α and Ga L_α signals. The compositional homogeneity variation of the maps were quantified by taking the standard deviation of the x-ray intensities over the entire map. For the Ga maps of B00 and D200 the standard deviation values were 38 and 33, respectively. This is evidence that the small amounts of hydrogen within the carrier gas for D200 improves the compositional homogeneity which leads to better quality material as seen in the SE images in Figure 4.2. For quantification of the given values and an estimate of the standard deviation background counts the N maps of B00 and D200 have a standard deviation value of 8.

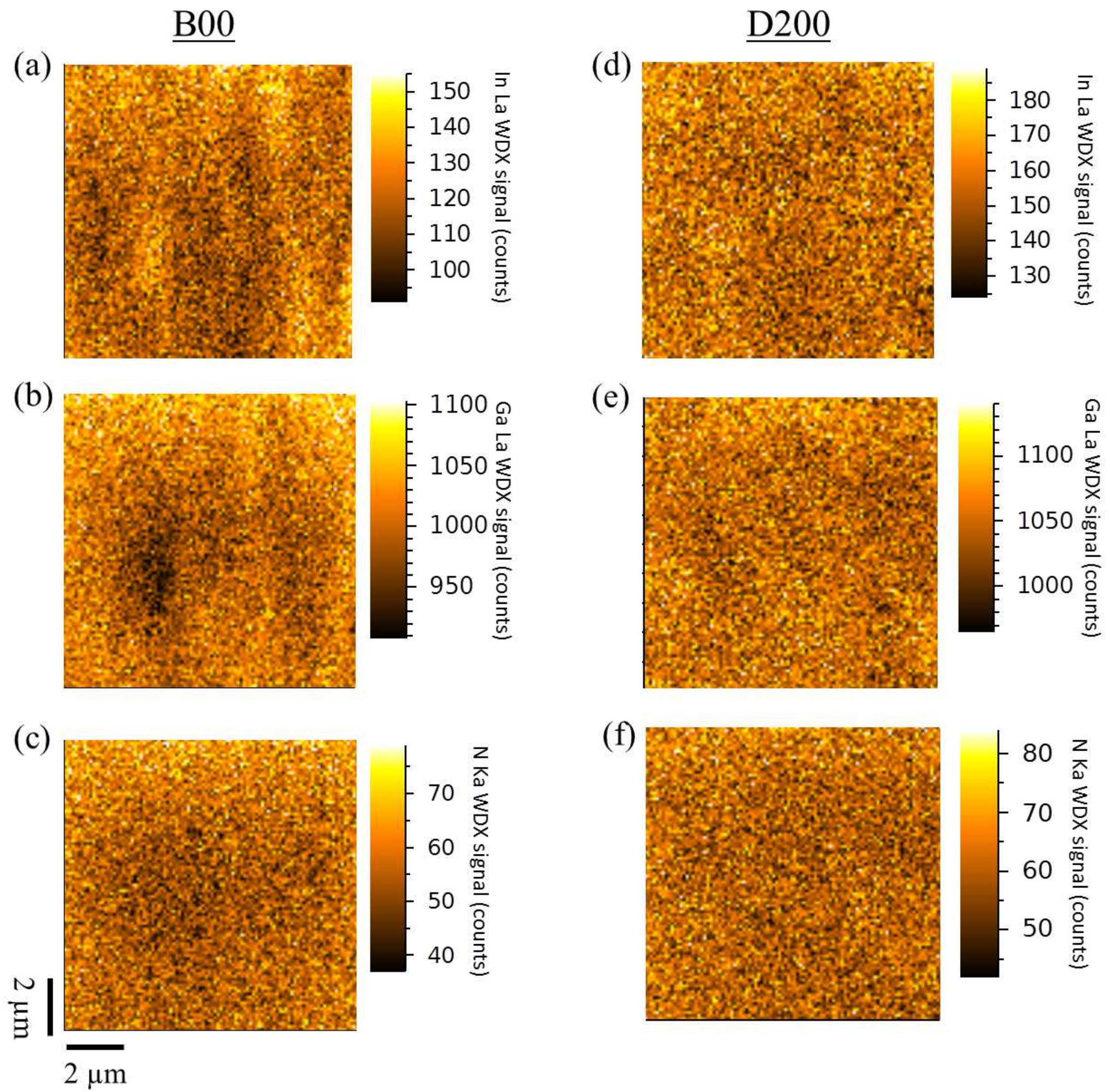

Figure 4.7: WDX maps of samples B00 and D200 showing the distribution of (a),(d) In L_α signal (b),(e) Ga L_α signal and (c),(f) N K_α signal, respectively.

4.5 Optical Characterisation

The luminescence properties of these InGaN epilayers were investigated using room temperature cathodoluminescence (CL) technique. Each sample was probed by a 6 keV electron beam and the emitted photons were collected in the home built optical collection system (see chapter 3). The measured spectra are shown in Figure 4.8(a) with the decrease in growth temperature (A-D) resulting in a decrease in intensity and peak emission energy, and an increase in full width half maximum (FWHM). Thickness (interference) fringes are evident in the spectra for all samples, while samples A00 and B00 have also pronounced low energy shoulders which can be attributed to phonon replicas.

The addition of small amounts of hydrogen results in a higher intensity and peak energy, and lower FWHM for samples grown at comparable growth temperatures. The peak energy shifts between the samples are clearer in Figure 4.8(b), where the strong negative linear trend between InN fraction and peak energy is shown [112, 131]. The FWHM is also shown to have a strong positive relationship with increasing InN content [112]. The peak energy points and peak widths were determined by Gaussian fitting of the spectra presented in 4.8(a). Comparing the peak energy and FWHM data to that reported by Martin et al. in Ref. [112] the peak energy linear dependence is in good agreement with the line of best fit having a slightly steeper gradient. The FWHM values are in reasonable agreement with the data in Ref. [112], showing similar linear trend but slightly lower absolute values. This could be due to improved epitaxial growth over time resulting in the narrower linewidths.

The better quality samples (A00, B00, C100 and D200) were further investigated by taking higher resolution cathodoluminescence (CL) hyperspectral images to see the relationship between luminescence homogeneity, growth temperature and hydrogen flow rate. The CL images shown in Figure 4.9(a) were generated by fitting a Gaussian curve to the InGaN emission peak of each spectrum in the hyperspectral image, and plotting the resultant peak energies as a function of position. An example of a fitted spectrum, taken from map B00, is shown in Figure 4.9(b). A visual comparison of luminescence homogeneity was accomplished by setting the range of the scale bars of each map to be the same, with the centre of the scale set to the mean peak energy of each individual map. In addition the

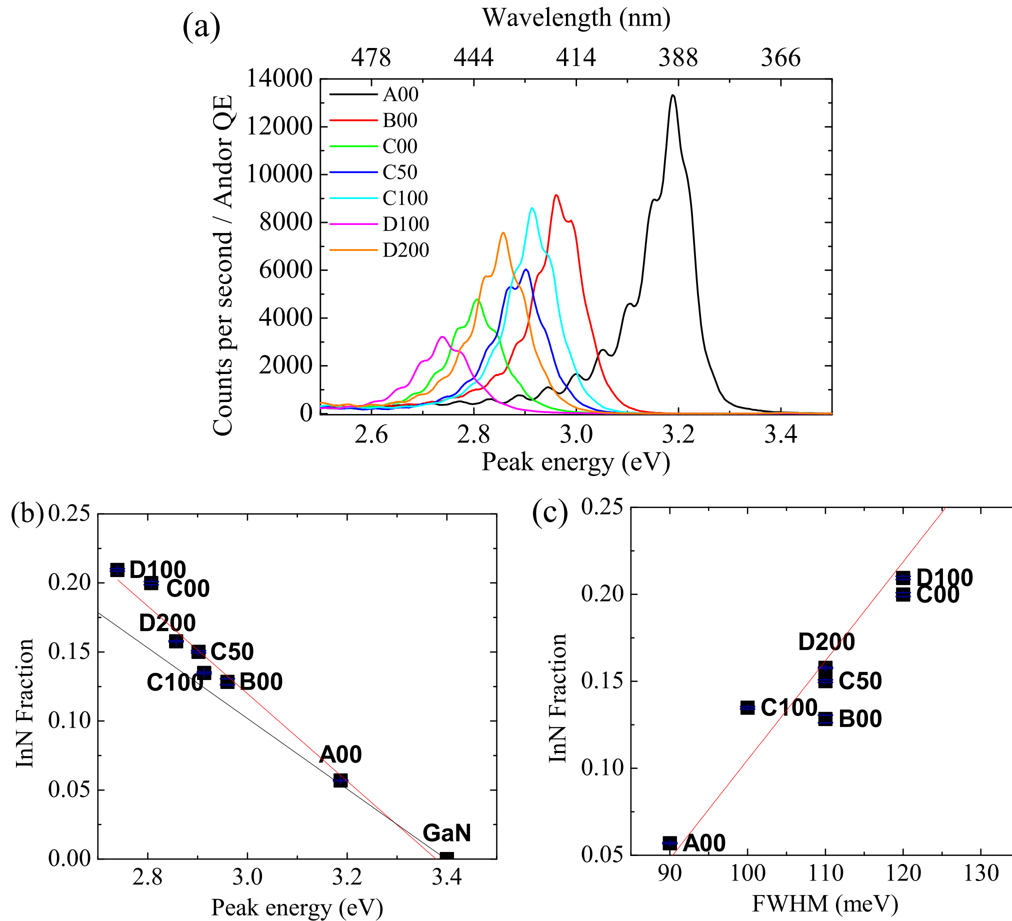

Figure 4.8: (a) Example room temperature spectrum from each of the InGaN samples. (b) Evidence of the strong negative trend between InN content and peak emission energy, with black line taken from data in Ref. [112]. (c) Strong positive relationship between InN content and FWHM.

mean maximum intensity of the CL peak of each map are shown in Figure 4.9(c), allowing a comparison of quantum efficiency to be made. The figure shows an overall decrease in mean CL intensity with decreasing growth temperature, but by a reduced rate for the samples grown with the addition of hydrogen.

The CL mapping illustrates an increase in peak centre variation with decreasing growth temperature, but this effect is reduced with the addition of hydrogen. For example the map of sample D200 (680°C, 200 sccm, 15.8 % InN) is seen to have less variation in peak centre across the map than sample B00 (725°C, 0 sccm, 12.8 %) despite its high InN fraction. In order to compare the luminescence ho-

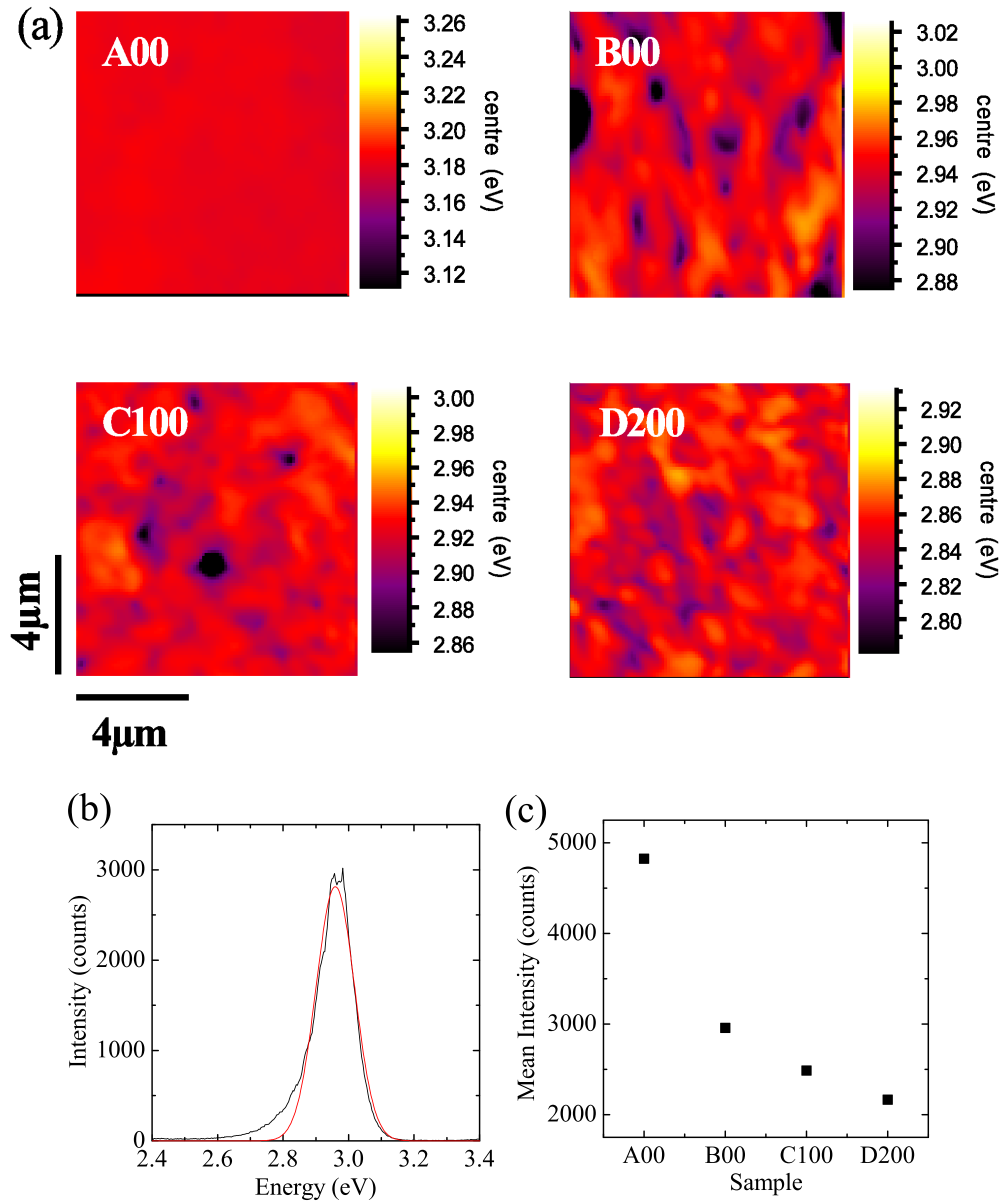

Figure 4.9: (a) Subsets of the CL hyperspectral images showing the change in peak energy centre over the mapped area of each sample. The scales of each map are centred on the mean peak energy of each sample and the range is kept constant across all maps allowing a comparison to be made. (b) A typical spectrum taken, with fit, from map B00 and (c) average peak CL intensity of each of the maps shown.

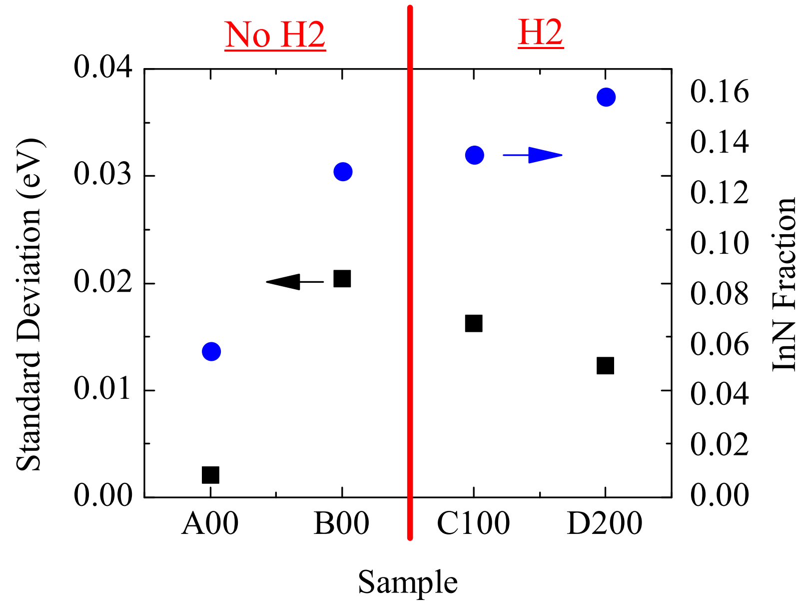

Figure 4.10: Quantified energy variation and average InN fraction for the CL maps (as shown in Figure 4.9) using the standard deviation of the peak energy variation.

mogeneity and quality, the variation of peak position in each map was quantified, by calculating the standard deviation over the entire map. The standard deviation highlights the energy spread within the measured area and is compared with the WDX composition for the different samples in Figure 4.10. The standard deviation in the peak energy is seen to reduce on going from samples B00 to C100 to D200 (i.e. on decreasing the growth temperature and increasing the hydrogen flow rate). This further emphasises that introducing small amounts of hydrogen into the carrier gas during growth at lower temperatures improves the luminescence homogeneity. The data further highlight that both a higher InN fraction and better luminescence homogeneity can simultaneously be achieved by introducing a small hydrogen flow into the growth procedure.

4.6 Summary

The composition and luminescence properties of a set of InGaN epilayers grown with varying temperature (680–750°C) and hydrogen flow rate (0–200 sccm) have been analysed. Compositional data from various techniques are in close agreement for the lower InN content samples, with the difference margin increasing with increasing average InN content. Further analysis revealed the presence of an indium gradient through the layer, for which the higher composition was found to lie near the surface of the layer. The amplitude of the InN gradient increased with increasing average InN fraction.

The samples grown with small amounts of hydrogen added to the nitrogen carrier gas were seen to improve in surface quality and compositional homogeneity in comparison to samples grown at the same temperature but with no hydrogen introduced. In addition to this improved quality and homogeneity, the addition of small flows of hydrogen to the nitrogen carrier gas during the InGaN deposition reduced the InN fraction. The loss of indium content could be compensated by lowering the InGaN growth temperature.

The small amounts of hydrogen also had an influence on the luminescence properties. The peak energy increased and FWHM decreased with increasing hydrogen flow compared to samples grown at the same temperature. The added hydrogen flow had a positive effect on the luminescence homogeneity with the CL maps of the higher quality samples showing a reduction in peak energy variation across the mapped area. By quantifying these peak emission energy variations it was shown that 160 nm thick InGaN epilayer samples with an average InN fraction of 10–15 % and grown with a small hydrogen carrier gas flow have a reduced spatial inhomogeneity of the emission energy compared to equivalent samples grown without hydrogen.

Many suggestions have been made as to why the hydrogen has these and other effects during growth of InGaN. Piner et al suggest that the hydrogen reduces the lifetime of the reactive indium at the surface and also reduces the thickness of the thermal boundary layer leading to less gas phase reactions [119, 132]. Thermodynamic calculations by Koukitu et al suggest that the addition of the H_2 can slow down the reaction between TMIn and NH_3 as H_2 is a by-product of the reaction, shifting the equilibrium towards the left [133]. More

recent suggestion by Czernecki et al is that the hydrogen attaches to the Ga and In adatom weakening the bond to the surface, with the adsorption energy of the Ga-H and In-H complexes being ∼1.8 eV smaller than the single metal adatoms [134]. Many more proposals have been made but understanding the influence of hydrogen has yet to be fully resolved.

The small amounts of hydrogen added for growing InGaN could also be applied to QW and LED structures. It would help improve the structural quality and luminescence homogeneity of the QWs even for the thin layers of the QWs, as suggested by the constant strain through material from the XRD measurements. This could result in higher InN contents being incorporated with higher recombination efficiency, leading to improved blue/green emitting devices. Further investigations would be required in order to confirm this.

Chapter 5

Composition and Luminescence Studies of InAl(Ga)N Epilayers

5.1 Introduction

$In_xAl_{1-x}N$, henceforth referred to as InAlN, is a wide and direct bandgap semiconductor alloy spanning an energy range of 0.7–6.2 eV [135, 136]. It has an advantage over other ternary nitride alloys in that it can be lattice matched to GaN with an InN content of ∼17 %, reducing strain induced defects, which improves crystalline quality and device efficiency [35, 45]. This gives InAlN the potential to replace other alloys such as AlGaN and InGaN in optoelectronic and power transistor devices. However difficulty arises in the growth of InAlN (and InAlGaN) due to the temperature differences between InN (∼600°C) and AlN (∼1100°C). This can lead to substantial compositional inhomogeneities and large variations in bandgap [137]. A widely researched application is the substitution of AlGaN barrier layers with InAlN in GaN based high electron mobility transitor (HEMT) structures [138, 139, 140]. The presence of the InAlN barrier induces a high density two dimensional electron gas (2DEG) through the difference in spontaneous polarization between InAlN and GaN, and higher current densities are possible [138, 141]. Furthermore, lattice matching the InAlN to GaN helps in reducing stress in the barrier which in turn may improve device reliability [40, 142]. InAlN can also be used for in situ optical monitoring during metalorganic chemical vapour deposition (MOCVD) growth of GaN based structures on free standing

GaN substrates [38]. This application exploits the difference in refractive index of lattice matched InAlN compared to GaN to aid with accurate growth rate measurement using in situ reflectometry. The inclusion of a thin InAlN layer allows for reflectivity oscillations whilst not inducing extra dislocations.

Recently it has been reported that unintentional Ga incorporation can occur during MOCVD growth of InAlN layers on GaN buffers in close-coupled showerhead vertical MOCVD reactors [143, 144]. The Ga incorporation has been associated with left over trimethylgallium (TMGa) precursor and Ga deposits on the susceptor and/or reactor walls [143, 145, 146]. Another proposed cause is diffusion of Ga from the underlying GaN layer [144]. Unwanted Ga incorporation can change the structural, electrical and optical properties of the nominal InAlN material, giving rise to undesirable characteristics. The bandgap has a strong dependence on composition, which determines the emission wavelength and efficiency of an optoelectronic device.

Ga auto-incorporation is difficult to determine through x-ray diffraction (XRD) alone, which is often the primary characterisation technique used after growth. This is due to the interplay of composition and strain, and therefore Ga inclusion can often be missed. This chapter describes the thorough analysis of the composition of Ga auto-incorporated InAlGaN layers using wavelength dispersive x-ray (WDX) spectroscopy. Rutherford backscattering spectrometry (RBS) measurements were performed at IPFN, Intituto Superior Técnico, Portugal, to confirm the Ga inclusion and x-ray diffraction (XRD) data from Tyndall National Institute, Cork was re-evaluated to give further confirmation and to provide extra strain information. The optical properties of these InAlGaN layers are also investigated using cathodoluminescence (CL) measurements and related to the composition data.

5.2 Sample and Experimental Details

Four nominally InAlN (80 nm) layers were deposited on 1 μm GaN buffer layers in a 3×2” AIXTRON close coupled showerhead MOCVD reactor at the Tyndall National Insitute, Cork. The substrates used were c-plane sapphire substrates with a 0.4 degree miscut. All layers were non-intentionally doped. Before each layer was grown the showerhead through which precursor gases enter the reac-

InAlN layer growth condition	Sample A	Sample B	Sample C	Sample D
NH_3 (mmol/min)	56	56	168	56
TMIn (μmol/min)	5	5	16	5
TMAl (μmol/min)	5	5	16	5
Growth time (s)	1330	1330	1300	2520
Reactor total flow (sccm)	8000	8000	24000	24000

Table 5.1: Selected growth parameters for the nominally InAlN epilayers grown in this series.

tor was cleaned and the reactor baked in an attempt to minimise contamination of epilayers. Trimethylgallium (TMGa), trimethylindium (TMIn) and trimethylaluminium (TMAl) were used as group III precursors. The GaN layers used a standard recipe, with a low temperature GaN nucleation layer followed by growth at 1060 °C with H_2 used as a carrier gas [147, 148]. The reactor conditions and carrier gases were then changed to those suitable for InAlN growth, using N_2 carrier gas both for the main reactor flow and as the precursor flow for the TMAl and TMIn. The InAlN epilayer growth parameters are presented in Table 5.1 above. Sample C has three times the group III and V precursor flows of samples A and B, and the carrier flows are scaled up accordingly to give a total flow of 24000 standard cubic centimetres per minute (sccm) compared to 8000 sccm for A and B. Sample D uses the same group III and V precursor flow rates as A (and B) but maintains the high 24000 sccm total flow rate of sample C, by using an increased carrier gas flow. As a result the V/III ratio of 4573 was held the same for all samples, as was the temperature (790 °C) and total pressure (70 mbar).

This chapter describes WDX measurements taken using our Cameca SX100 electron probe micro-analyser (EPMA) consisting of three x-ray spectrometers with TAP (thallium acid phthalate), LPET (large pentaerythritol) and PC1 (synthetic pseudocrystal) diffracting crystals used for elemental detection [76, 131]. Collaborators at IPFN, Portugal performed RBS using a collimated beam of 2 MeV He^+ ions and a silicon pin diode detector positioned at a scattering angle of 165°. Spectral fitting of the RBS data was performed manually [149] and then confirmed by "NDF" code fitting [104] to obtain composition and thickness information. RBS minimum yield measurements were performed using a beam of 1.5 MeV He^+ ions and a scattering angle of 140° by Jorge Sabino at IPFN.

X-ray diffraction (XRD) data was measured using a PanAnalytical X'Pert double crystal diffractometer. Taken together these techniques provide information on composition, spatial homogeneity, depth homogeneity and strain. The optical properties of the layers were investigated using cathodoluminescence (CL) spectroscopy measured in a scanning electron microscope (SEM) [111, 150]. Additional sample quality analysis was performed through secondary electron (SE) and atomic force microscopy (AFM) imaging, and RBS minimum yield measurements to gain information on sample quality and growth conditions. The SE images were taken on our field emission gun (FEG) ESEM and the AFM images were taken by Michele Conroy at Tyndall National Institute, Cork.

5.3 Sample Quality

The SE images in Figure 5.1 show a large variation in surface features across the 4 samples. The comparison of SE images of samples A and B reveals that sample B has a lower quality surface, which is evident from the mottled effect of the surface, though both growths were the same. The SE image of sample C differs from the other 3 samples as it shows striations across the surface. These are likely to be atomic steps, which may be the result of the different precursor flow for sample C. The surface of sample D is also different in comparison to the other 3 (Figure 5.1). The surface appears smoother than sample A, but still has a number of surface defects which are of lower density than sample A. Again this could be due to having triple the total flow rate, like sample C, whilst having the same precursor flow as samples A and B. In addition lower magnification images (not shown) revealed that both samples A and D exhibit similar linear cracking on the surface which can be related to tensile strain [151].

The sample surfaces were also imaged by atomic force microscopy (AFM), offering further insight into the growth processes at work for each reactor condition. Figure 5.2 shows 5×5 μm^2 surface AFM images of samples A–D, with the surface morphology and measured root mean square (rms) roughness recorded. As in the SE images in Figure 5.1, sample B is confirmed to be of poorer quality than sample A despite the two having nominally the same growth conditions. Its morphology has a mottled effect which is similar to the SE image and has > 3 times the rms roughness value of the other samples. Hillock features commonly

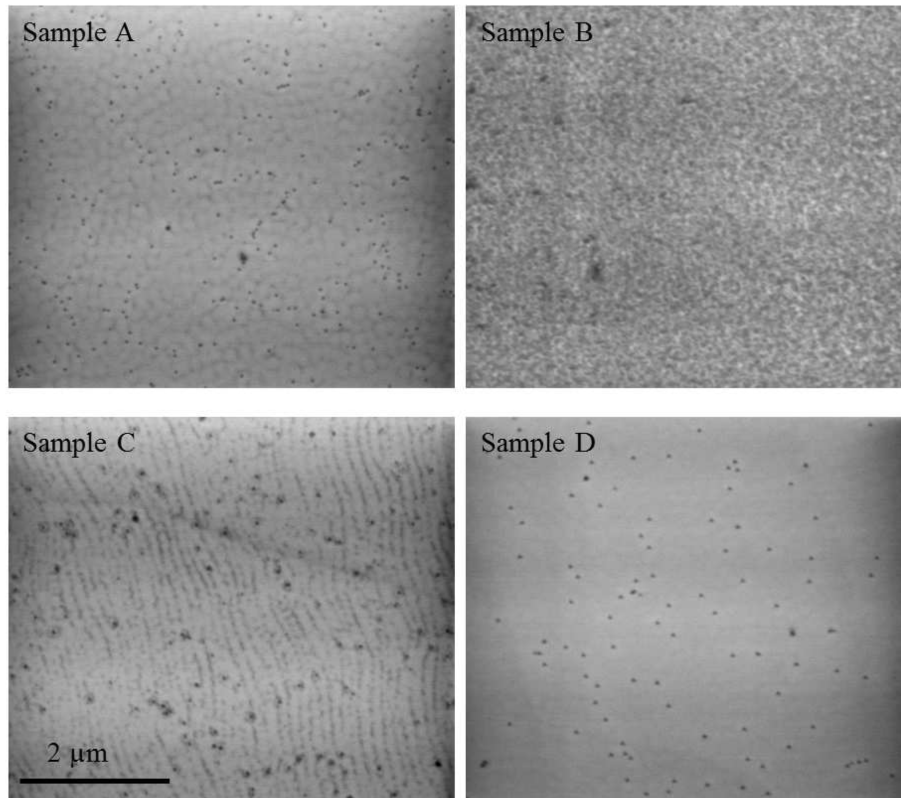

Figure 5.1: Secondary electron images of all samples.

found on InAlN surfaces are visible in samples A, C and D, although interestingly the sample with the raised group III flow rates, sample C, exhibits a regularity in the hillock spacing reminiscent of step-flow growth, a common feature of GaN surfaces. This is seen to a lesser extent in sample A and is absent in sample D. Clearly modifying the incoming precursor and carrier gas flow rates affects not only the composition of the layer (see later) but also its morphology.

The rms values of the 4 samples reveal that all layers apart from B have comparable surface roughness (approx. 1–2 nm). Samples C and D, which were grown with the higher total flow rates, have an estimated dislocation density visible by AFM of approximately $4/\mu m^2$. Sample A showed no such defects, representative of the need to optimise growth with higher total flow rates when compared to the more established standard flows. However, the SE images in Figure 5.1 (taken at lower magnification than the AFM images in Figure 5.2) show sample A to have a surface defect density comparable to that of C and

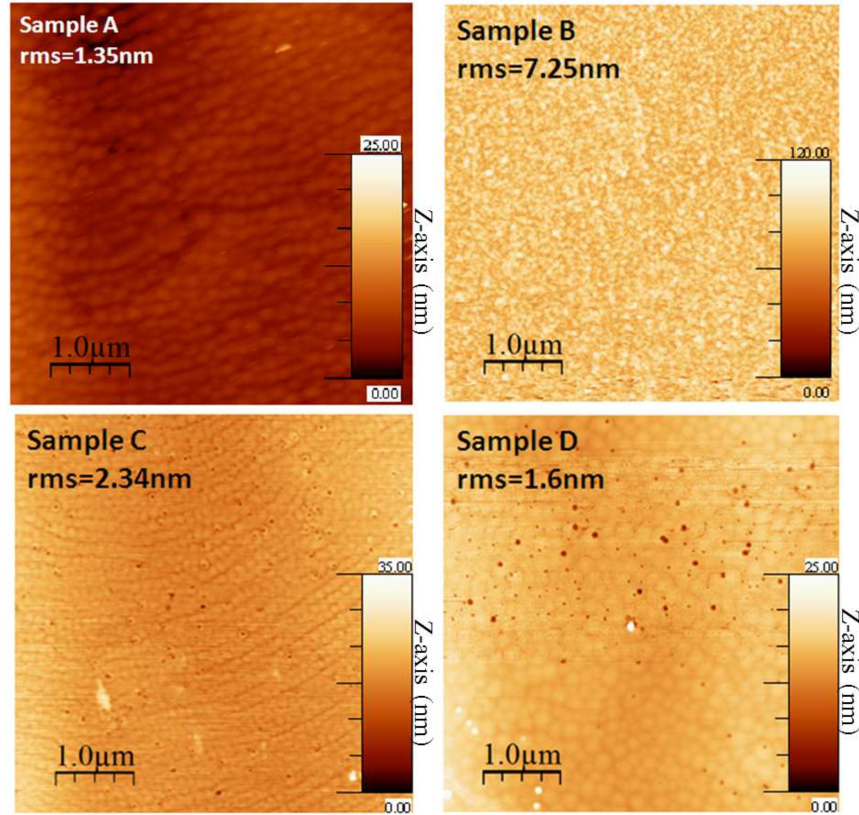

Figure 5.2: AFM images of all samples. The colour scale gives the vertical height in nanometres.

D. The reason for the discrepancy is unclear, and may be due to inadvertently sampling a small area of defect-free surface in AFM. Further investigations are required.

RBS minimum yield measurements were also performed to obtain further information on sample quality below the surface. As described in section 3.4.2 the minimum yield is determined by the ratio of the aligned counts to the random counts ($\chi_{min} = I_{aligned}/I_{random}$), and in this case the minimum yield was calculated for both the In and Ga peaks for all samples. The same set up and calibration was used throughout so that the regions of interest of each of the peaks were kept consistent over the 4 samples, with the energy range for the Ga peak ∼1555–1595 keV and the In peak ∼1690–1725 keV (Figure 5.3). The results are presented in Table 5.2.

The low minimum yield values of ∼3 % for samples A, C and D reveal a very

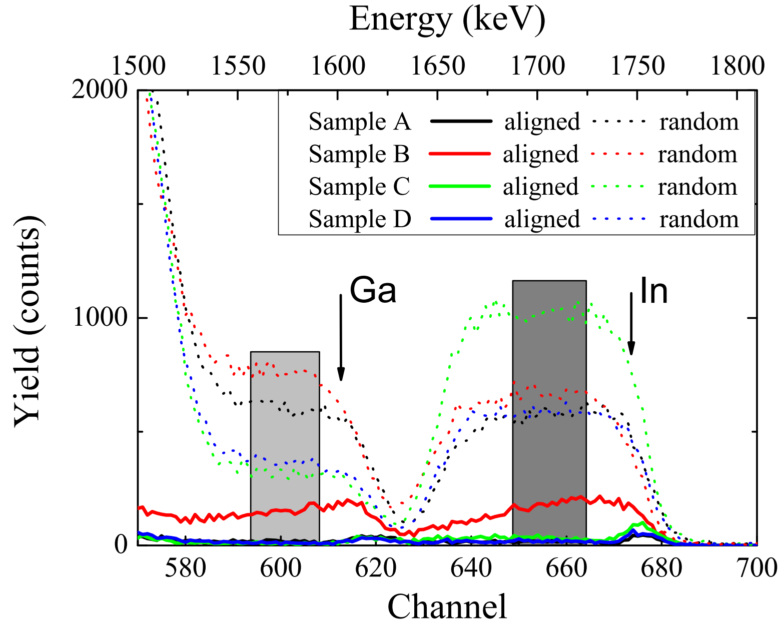

Figure 5.3: RBS minimum yield spectra with aligned and random spectra shown and areas of interest of Ga and In peak shown in grey.

	Sample A	Sample B	Sample C	Sample D
In aligned (counts)	329	3076	502	308
In random (counts)	10741	11168	16417	9412
In minimum yield %	3.1	27.5	3.1	3.3
Ga aligned (counts)	306	2604	143	171
Ga random (counts)	11087	12525	5066	5808
Ga minimum yield %	2.8	20.8	2.8	2.9

Table 5.2: Minimum yield results from the In and Ga peaks of the RBS spectra for each of the InAlGaN epilayers.

good crystalline quality for the InAlGaN layers, as was deduced from the SE and AFM images in Figures 5.1 and 5.2. Sample B returned a higher minimum yield in the range of 20–28 %. This indicates the sample is of lower quality which was again evident in the SE and AFM images. For sample B there is a clear gradient of backscattering yield in the aligned spectrum for both In and Ga regions of interest in Figure 5.3, showing that the film starts to grow with a good crystal quality which then deteriorates towards the surface. The results indicate that Ga atoms are less affected by this deterioration than the In atoms with ∼7 % less

minimum yield. This is also evident in the rest of the samples where the Ga has < 0.5 % minimum yield than In. The slope of the aligned spectrum in the regions of interest, along with the detector resolution and partial overlap of In and Ga signals may be potential causes for the differing values of the minimum yield.

5.4 Compositional and Structural Characterisation

Qualitative WDX spectral scans were performed at various electron beam energies to detect all elements present within the nominal InAlN/GaN bilayers. Each WDX crystal is rotated over the full angular range and maxima are detected at the corresponding elemental x-ray wavelengths satisfying Bragg's law (Section 3.4.1). The main x-ray lines detected were In L_α, Al K_α, Ga L_α and N K_α. At a beam energy of 2 keV a Monte Carlo electron trajectory simulation [94] shows 90 % of the deposited energy is within 35 nm of the surface as shown in Figure 5.4(a). Figure 5.4(b) shows Ga peaks in the spectrum from the TAP crystal at 2 keV, for which the beam excitation volume does not penetrate into the underlying GaN, demonstrating the presence of Ga within the top layer.

The threshold energy for excitation of the indium L_α x-ray is approximately 3.5 keV, requiring an electron beam energy in excess of this to accurately measure the In content. Analysis of electron trajectories using Monte Carlo simulations indicates that the excitation volume for beam energy of 4 keV reaches to a depth of approximately 95 nm for InAlGaN on GaN. Thus the thickness of the studied layers (<90 nm) is such that electrons of energy 4 keV and higher will penetrate through to the underlying GaN layer and generate x-rays from here (Figure 5.4(a)). Measurements were therefore taken at a number of different beam energies in the range 2 keV to 6 keV and the composition determined using software that analyses x-ray fluorescence from multilayer structures [100].

An InAlGaN-GaN bilayer was simulated for various (stoichiometric) quaternary compositions with the thickness of the quaternary layer set to be that determined from XRD. The RBS thickness was also used to help determine the composition but the simulation returned a poorer fit to the WDX measured data. These thickness values are given in Table 5.3. Characteristic x-ray fluorescence

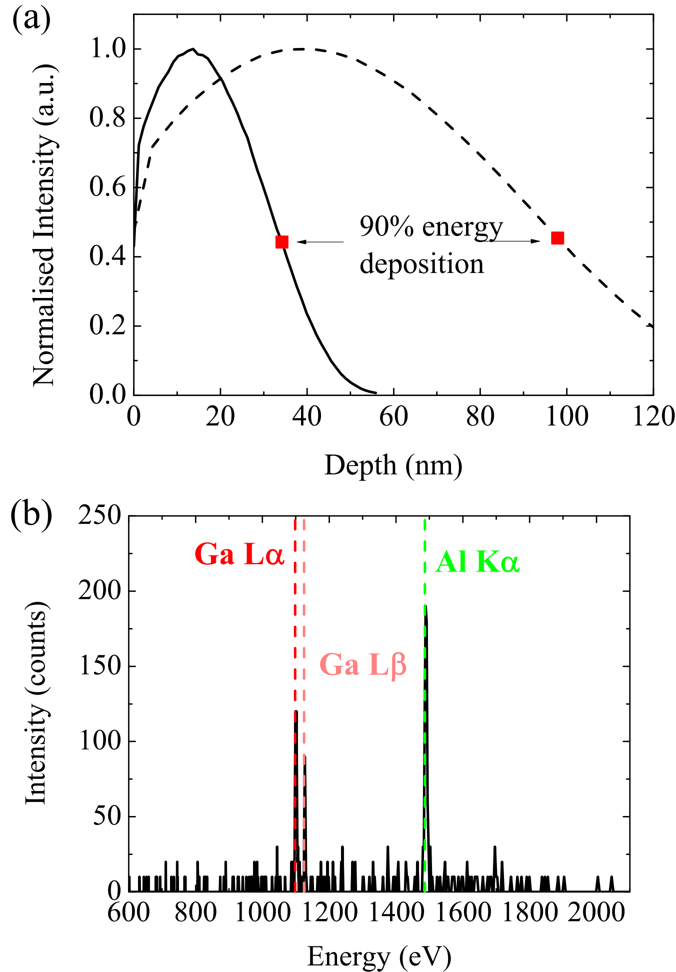

Figure 5.4: (a) Beam energy deposition from Monte Carlo electron trajectory simulations of 2 kV (solid line) and 4 kV (dashed line) beam energies. (b) Example WDX spectrum from the TAP crystal using a 2 kV beam showing the presence of Ga.

intensities were measured and compared with those from known standards (k-ratio = I_x/I_{std}), which were AlN for Al, InP for In and GaN for Ga and N (Section 3.4.1). The InAlGaN composition was altered in the simulation to provide an optimum fit to the measured WDX data as a function of excitation energy. The WDX data for In, Ga, Al and N are plotted against electron beam energies in Figure 5.5 for sample A, making up 15 points in total to fit. The decrease in Al and In counts and increase in Ga at higher beam energies are due to the excitation volume penetrating further into the underlying GaN buffer layer. For

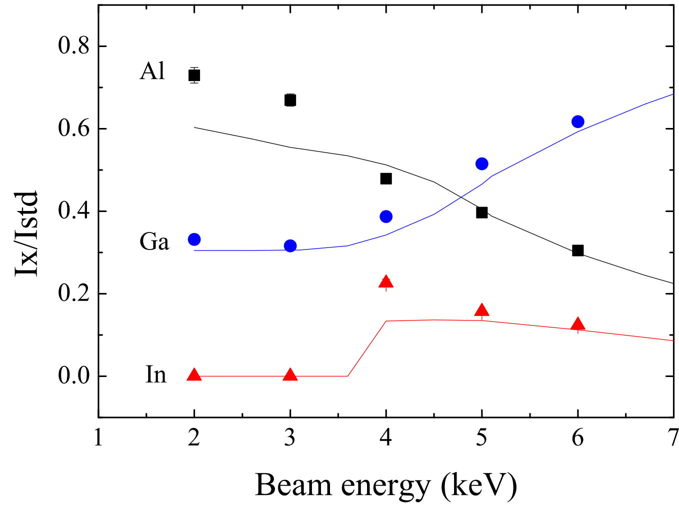

Figure 5.5: WDX measurement (points) and simulation (lines) for sample A.

energies below the In L_α x-ray excitation energy ($<$ 3.5 keV) there are no In counts, whilst the Ga counts measured below 3 keV demonstrate the presence of Ga in the upper layers. These features are evident in all measured samples. The fractional error in fitting to the measured points was calculated for each element at each beam energy. These values were averaged over the 15 points to obtain the uncertainty in the fit for each sample. Combining the error in the fit with the random and systematic errors resulted in uncertainties of approximately 10 % (i.e. [InN] = 7.0 $\pm$ 0.7).

RBS measurements were performed on each of the samples to confirm Ga auto-incorporation. To determine the composition and estimate its uncertainty, a manual analysis of the spectra was performed with the assumption of a homogeneous quaternary layer and a III/V ratio of unity. For this the Al/In and the Ga/In ratios were determined from signal areas and heights, respectively, following the procedures in Refs [149, 152]. The data were also fitted using the "NDF" code [104] confirming the compositional results and yielding values for the film thicknesses. Figure 5.6(a) shows the RBS spectrum measured from sample A and the corresponding fit assuming a homogeneous quaternary film. The Ga-incorporation in the uppermost layer is clearly shown by the shoulder at 1600 keV. Figure 5.6(b) shows the RBS spectra of all samples in the relevant area comprising the signals of In and Ga close to the surface. Incorporation of

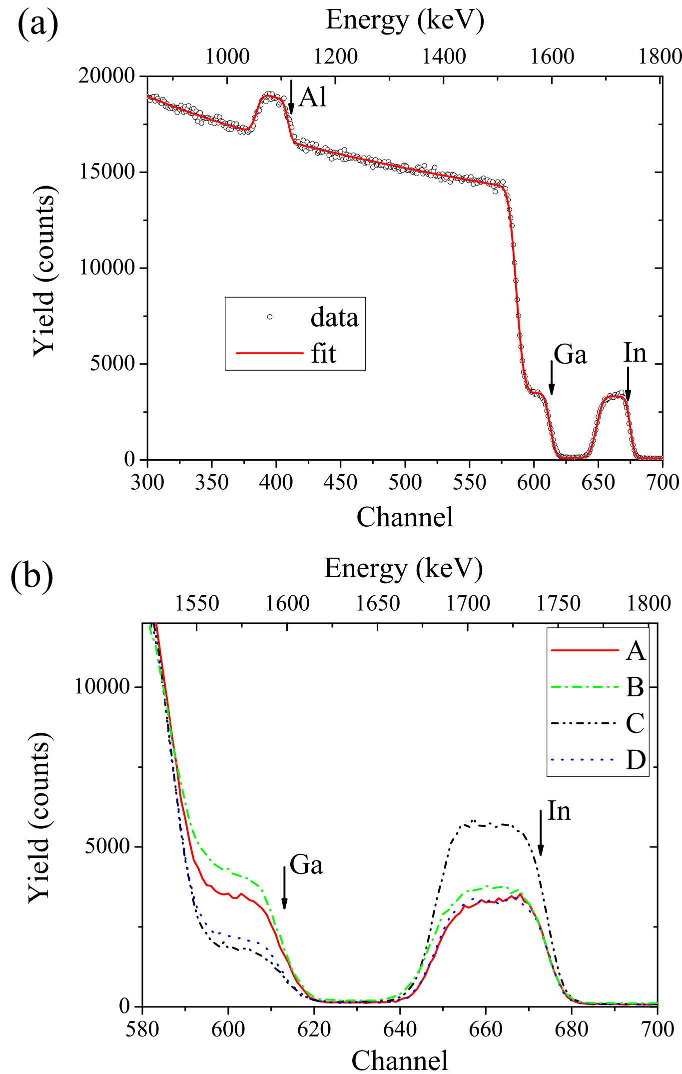

Figure 5.6: (a) RBS plot of the InAlGaN layer on GaN of sample A, showing the aluminium, gallium and indium signal. (b) Measured RBS spectra of all samples highlighting the small shoulder at ~1600 keV due to Ga in the top layer. Arrows indicate elements at the surface.

Ga is clearly observed for all samples albeit with different concentrations. It is clear from the Ga shoulder that samples C and D have less Ga incorporated than samples A and B. The overall uncertainty associated with the RBS data for the In and Ga content is approximately 4 %, and for the Al content approximately 1 %.

	Sample A		Sample B		Sample C		Sample D	
	WDX	RBS	WDX	RBS	WDX	RBS	WDX	RBS
AlN %	69.0	72.2	64	66.4	73.0	74.9	79.0	79.7
InN %	7.0	7.9	8.0	9.0	15.0	14.4	7.0	8.0
GaN %	24.0	19.9	28.0	24.6	12.0	10.7	14.0	12.3
XRD thickness (nm)	87.5		87		82		88	
RBS thickness (nm)	79		80		79		81	
InAlGaN a (Å)	3.178				3.174		3.199	
InAlGaN c (Å)	5.072				5.116		5.046	

Table 5.3: Composition fraction results from WDX and RBS measurements which were checked for consistency by XRD, and thickness results from both XRD and RBS. Also included are the a and c lattice parameters for the InAlGaN layer calculated from reciprocal space maps.

The resulting WDX and RBS composition data for the upper InAlGaN layer are summarised in Table 5.3, and reveal GaN fractions between 12 and 28 % and InN fractions between 7 and 15 %. There is high agreement between the WDX and RBS techniques. Consistently the RBS estimate of the InAlGaN thickness is somewhat lower than that determined by XRD. This could be a combined result of measuring different areas of the wafer and small discrepancies between the techniques, with the XRD thickness determined from Pendellösung fringes and the RBS thickness calculated using a density determined from interpolation of the known density values of the III-N binaries.

Relating these composition results back to the growth parameters in Table 5.1 we can see that those for samples A and B have resulted in more Ga incorporation, compared to samples C and D. This indicates that the increase in total flow rate acts to suppress the Ga incorporation and suggests the auto-incorporation is due to residual Ga coming from the reactor walls and delivery pipes, as suggested in Refs [143, 145, 146]. Increasing the total flow rate causes a reduction in the concentration of Ga above the sample surface, assuming a constant supply of Ga from the reactor walls and pipes. Sample D has approximately half the growth rate of samples A, B and C, but the results show no dependence on Ga auto-incorporation on growth rate.

After many growth runs a build up of matter can occur on the walls and delivery pipes which can be picked up by precursors. This suggests that the sus-

ceptor, showerhead and reactor may have to be fully cleaned between GaN and InAlN growth runs in order to suppress Ga incorporation completely. This can be a lengthy process and may not be a practical method for growth of InAlN. Therefore, refining the growth conditions to control the amount of Ga incorporated may be a more suitable solution. This will no doubt infer implications when growing InAlN for power transistor and optoelectronic devices.

HEMT structures have been grown under similar conditions to sample A at Tyndall National Institute, Cork. One HEMT had a pause after the growth of the GaN buffer where the reactor and showerhead were cleaned, and also the susceptor was changed to one which had not been exposed to Ga previously. The results revealed an order of magnitude decrease in Ga incorporation (approx. 13 to 1 %) in the InAlN layer when cleaning was implemented between the GaN buffer and InAlN layer [153]. This showed that the modified growth procedure was successful but did not fully eliminate Ga from being incorporated.

Another potential solution for the reduction of Ga auto-incorporation in InAlN is to have a small flow of TMIn when growing a high temperature buffer layer like AlGaN, GaN etc. The TMIn acts by stimulating Ga desorption from the reactor chamber during the buffer growth so Ga deposits will not build up. Due to the high growth temperatures the In should not be subject to adsorption within the buffer layer. The presence of TMAl during buffer growth has also been attributed to suppression of Ga incorporation like the TMIn but will result in Al incorporation. These hypotheses are currently being studied with AlGaN buffer layers grown at (1110°C) with and without TMIn flow. From initial WDX qualitative experiments the InAl(Ga)N on AlGaN buffers (without TMIn) have considerably reduced Ga incorporation in comparison to the InAl(Ga)N/GaN samples investigated in this chapter as shown in Figure 5.7. The InAl(Ga)N/AlGaN sample grown with TMIn during buffer growth has further reduced Ga incorporation in comparison to samples grown without TMIn flow at the buffer stage. Further work is required in order to obtain quantitative values and to fully understand this result, as the presence of TMAl during buffer growth seems to be the dominant factor in the suppression of Ga incorporation.

A reciprocal space map (RSM) was measured using [105] XRD scans to provide strain information for each InAlGaN/GaN sample. Sample B was omitted from this measurement due to it being of lower quality. All other InAlGaN layers

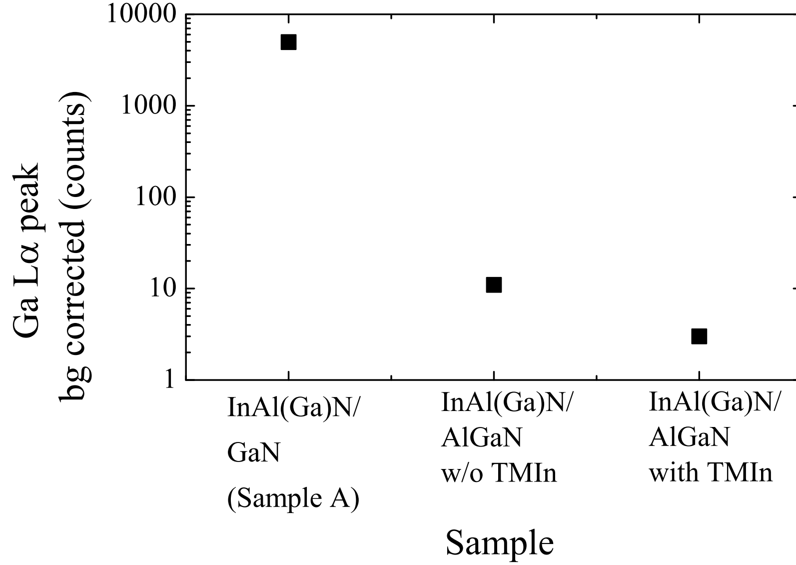

Figure 5.7: WDX qualitative scan Ga L_α spectral peak values measured from InAl(Ga)N/GaN Sample A (T_g = 790°C), and InAl(Ga)N/AlGaN samples with and without TMIn flow (T_g = 765°C).

were found to be fully strained to the underlying GaN, having the same a lattice parameter as shown for Sample A in Figure 5.8. The InAlGaN c lattice parameters varied across the sample set from (5.046 to 5.116 Å), as shown in Table 5.3, and were calculated from the RSMs using Equation 5.2. The c lattice parameters calculated from the composition results using Vegards law are in good agreement with these RSM values, increasing in the order Sample D, A, C. Sample C, with the considerably higher InN content, is seen to have the highest c-parameter and thus the lowest level of in-plane compressive strain. Relating this to the SE and AFM images we can say that the surface morphology is not a result of lattice mismatch.

$$a = \frac{1}{Q_y}\frac{\lambda}{\sqrt{3}}h \tag{5.1}$$

$$c = \frac{1}{Q_y}\frac{\lambda}{2}l \tag{5.2}$$

The values of all the allowed composition and relaxation values for the 0002 scans of each InAlGaN sample were determined using this strain data. Both the

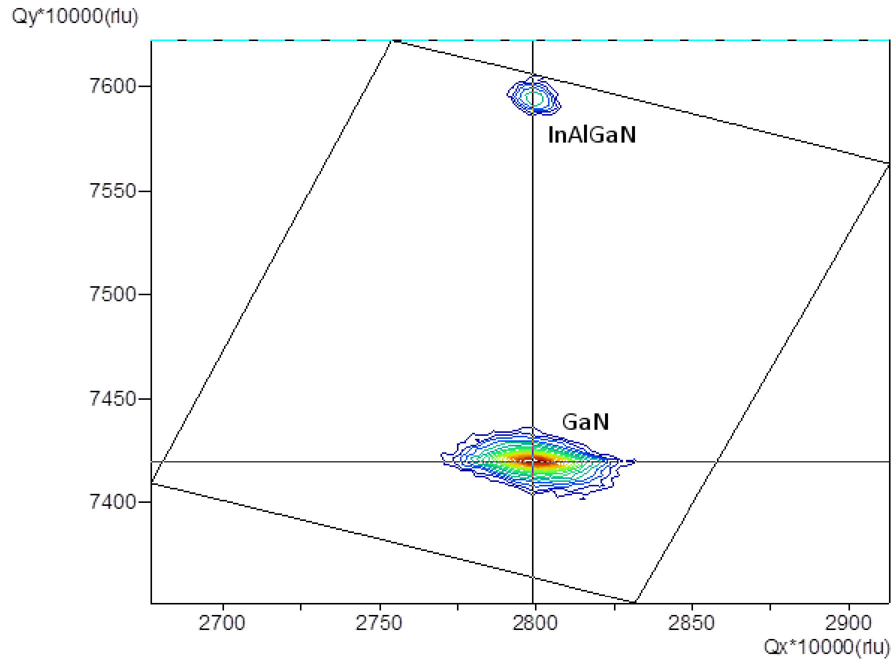

Figure 5.8: [105] RSM of sample A illustrating fully strained layer. The lattice parameters shown in Table 5.3 were taken from the equivalent maps for samples C and D.

WDX and RBS measured compositions for all samples fell within the range of determined XRD compositions indicating further consistency between the techniques. The XRD analysis and further strain and structural investigations are presented in Smith et al [153].

5.5 Optical Characterisation

The optical properties of these InAlGaN epilayers were studied using CL in the EPMA. Figure 5.9 shows CL spectra measured using a 5 kV beam voltage. These spectra are the mean of the 10^4 spectra in 5 μm^2 hyperspectral maps consisting of 100×100 pixels with a full spectrum saved at each pixel. The CL maps reveal a strong GaN peak at 3.4 eV which comes from the underlying GaN buffer layer. A broad InAlGaN luminescence is also evident within the maps and is fairly uniform over the mapped area, with several single spectra from different areas seen to have minimal change in shape as shown for sample A in Figure 5.10.

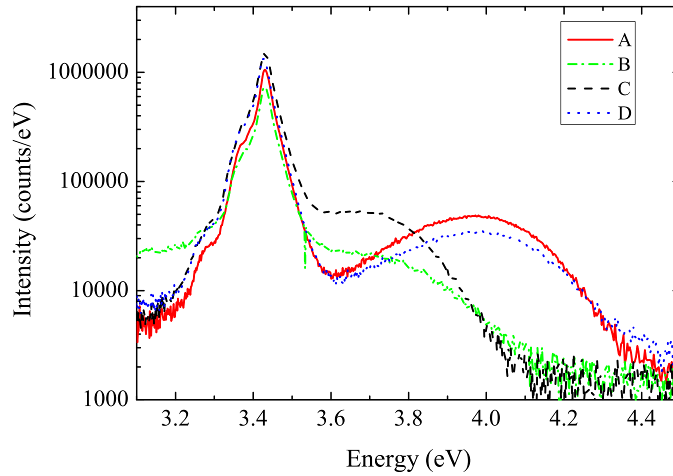

Figure 5.9: Mean spectra of CL maps show the InAlGaN luminescence peak.

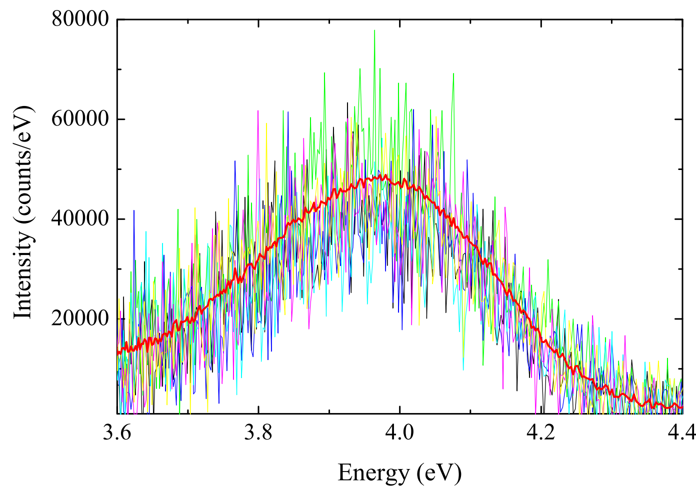

Figure 5.10: Single CL spectra taken from several different pixels over the map of sample A, with the mean spectrum of the whole map presented in red.

The InAlGaN luminescence of samples C is red shifted (3.7 eV) in comparison to samples A and D (3.95 eV). This is due to the higher InN content (15 %) within the layer. Sample A has 10 % more GaN than sample D but they have comparable spectra and the same peak energy which indicates that the change in GaN content has no great effect on the luminescence peak energy. This is the result of the extreme bandgap bowing for InAlN at low InN contents, which

reduces the possible bandgap variation for InAlGaN as the GaN content changes at low InN [60]. The broad luminescence in sample B which extends either side of the GaN peak could be attributed to AlN defect luminescence which is found around 3.3 eV with a linewidth > 500 meV [154, 155]. This is a result of the poor quality of sample B as was indicated by the minimum yield data in Table 5.2 and suggests that the InAlGaN layer has resulted in AlN clustering.

5.6 Summary

The compositional, optical and structural characterisation of a set of ∼80 nm thick InAlGaN epilayers with Ga auto-incorporation has been presented in this chapter. The samples have been analysed using a range of techniques to confirm the Ga auto-incorporation and to investigate the properties of the resultant quaternary. The SE imaging, AFM and RBS minimum yield techniques revealed that sample B is of poor quality with large surface roughness and a strong In and Ga gradient within the layer, unlike sample A which was grown with identical parameters. The CL results confirmed this poor quality with a weak, broad luminescence which may be associated with AlN defect.

The composition results from WDX and RBS measurements confirmed the presence of Ga within the top layer with GaN contents ranging 12–28 %. The values returned from the 3 techniques, including XRD, are all in good agreement. The growth parameters and resultant Ga incorporation indicate the likely cause being residual Ga coming from the reactor walls and delivery pipes. Increasing the total flow rate from 8000 sccm to 24000 sccm is seen to suppress the GaN incorporation from 28 to 12 %. This is a more viable method for reducing Ga incorporation than reactor cleaning between growth of the GaN buffer and InAlN layer as this is time consuming and samples have to be removed from the reactor resulting in surface oxidation issues.

Cathodoluminescence measurements revealed a broad InAlGaN peak whose energy varied with InN composition. The increase in InN resulted in a decrease in emission energy, but the change in GaN content caused no such variation in peak energy, which is positive for making UV LEDs that may inadvertently contain Ga. This broad quaternary luminescence peak showed to be fairly uniform when mapped over a small area. Although the Ga auto-incorporation had little or no

affect on the luminescence properties in this study there are implications that could arise in other InAlN devices such as HEMTs. The addition of Ga alters the structure of the nominal InAlN which can shift the lattice away from the LM point of GaN inducing strain at the InAl(Ga)N/GaN interface, influencing the electrical properties.

Consolidating these results with those from the literature it is believed that the root of the Ga auto-incorporation problem is in the design of some vertical MOCVD reactors. This indicates that InAlN can be grown Ga free and is not a fundamental issue.

Chapter 6

Composition and Luminescence Studies of InAlN/AlN Epilayers

6.1 Introduction

InAlN is a wide bandgap material which has an energy range from 0.7 eV to 6.2 eV by altering the composition, as outlined in Chapter 2 [136]. This makes it useful for a wide variety of applications. Unlike other nitride alloys it can be lattice matched to GaN with an InN content of approx. 17 %. This is the desired and most common method of growing InAlN due to the reduction in defects, improved device efficiency and crystal quality. A less explored alternative option for the buffer layer is AlN. Growing InAlN on AlN removes the chance for Ga auto-incorporation which is often a concern when growing on GaN as it can alter the materials properties as was explored in the previous chapter [147]. AlN buffers are seen to improve crystal quality and surface topography in the InAlN layer compared to an InAlN layer grown under same conditions but on GaN [156].

Pure InAlN layers on AlN are desirable for use as light emitters spanning the UV region of the energy spectrum. They allow low InN containing layers to be produced with low strain between the buffer and epilayer, unlike on GaN where reducing the InN composition far below the lattice match point ($\sim$17 %) results in highly tensile strained layers. Recent studies have shown that the band bowing effect is larger than previously thought especially at low InN contents [60].

Difficulty does arise in growing good quality InAlN layers on both AlN and

GaN buffers due to the large differences between the InN and AlN covalent bonds, and their lattice constants. This leads to phase separation and compositional inhomogeneities [45, 157]. The choice of growth temperature also poses challenges as there are large differences in the optimum temperatures for each binary compound, ∼600°C for InN and ∼1100°C for AlN, resulting in a large immiscibility gap [158, 159]. This makes incorporating small amounts of InN into AlN challenging.

In this work the optical and compositional properties of a series of InAlN layers with InN compositions ranging from <1 % to 30 % are investigated through cathodoluminescence (CL), photoluminescence (PL), wavelength dispersive x-ray (WDX) and x-ray diffraction (XRD) measurements. The surface quality was also studied through secondary electron (SE) imaging.

6.2 Sample and Experimental Details

A series of InAlN layers with thicknesses of ∼80–150 nm were grown on AlN buffers in a 3×2" AIXTRON close coupled showerhead MOCVD reactor at the Tyndall National Institute, Cork. The templates used were standard 2.5 μm thick AlN templates grown on c-plane sapphire. Before growth of the InAlN layer a ∼100 nm thick AlN connecting layer was deposited on the previously grown template. The temperature and pressure were 1110°C and 50 mbar, respectively, and the growth time was 450 s to achieve the desired thickness of ∼100 nm. The reactor and showerhead were also cleaned prior to growing the buffer layer to remove any residual Ga from previous growth runs in order to eliminate any Ga auto-incorporation. Also the susceptor was changed to one not previously exposed to growth of Ga-containing layers. For the InAlN layer trimethylindium (TMIn) and trimethylaluminium (TMAl) were used as group III precursors, and ammonia (NH_3) was used as the nitrogen source. The flow rate of these precursors were 5.2 μmol/min for the TMIn and TMAl, and 1256 sccm for the (NH_3). These were held constant throughout resulting in a fixed V/III ratio. The pressure and total flow were also held constant at 70 mbar and 8000 sccm, respectively. The growth temperature was varied from 940°C to 730°C to obtain a large range of samples with indium contents up to ∼30 %, and the growth time was varied from ∼2100s to 2700s to obtain the desired thicknesses. The growth parameters for

Sample	Growth Temperature (°C)	Growth Time (s)	Thickness (nm)
A (NT0753)	730	2400	-
B (NT0752)	750	2400	-
C (NT0751)	770	2100	116
D (NT0749)	780	2100	150
E (NT0748)	790	2100	92
F (NT0747)	800	2100	80
G (NT0754)	816	2400	100
H (NT0755)	825	2700	125
I (NT0769)	838	2700	126
J (NT0760)	850	2100	96.5
K (NT0761)	861	2100	97
L (NT0762)	870	2100	97
M (NT0763)	880	2220	102
N (NT0764)	890	2220	101
O (NT0765)	900	2400	113
P (NT0768)	916	2400	118
Q (NT0766)	929	2400	-
R (NT0767)	938	2400	-

Table 6.1: Growth parameters for the large set of InAlN/AlN epilayers grown in this series, with the layers thicknesses measured by XRD.

each sample, along with the thicknesses determined through XRD measurements (where possible) are presented in Table 6.1.

The SE images and CL measurements presented in this work were taken in a FEI Quanta 250 environmental SEM using low vacuum (LV) mode. WDX composition measurements were taken using the Cameca SX100 electron probe micro-analyser (EPMA), and confirmed by XRD which was performed at Tyndall National Institute, Cork using a PanAnalytical X'Pert double crystal diffractometer. The InN content for each sample provided by our collaborators through XRD measurements straight after growth is shown in Figure 6.1. The black points in Figure 6.1 represent the composition of fully strained layers and the red points fully relaxed layers.

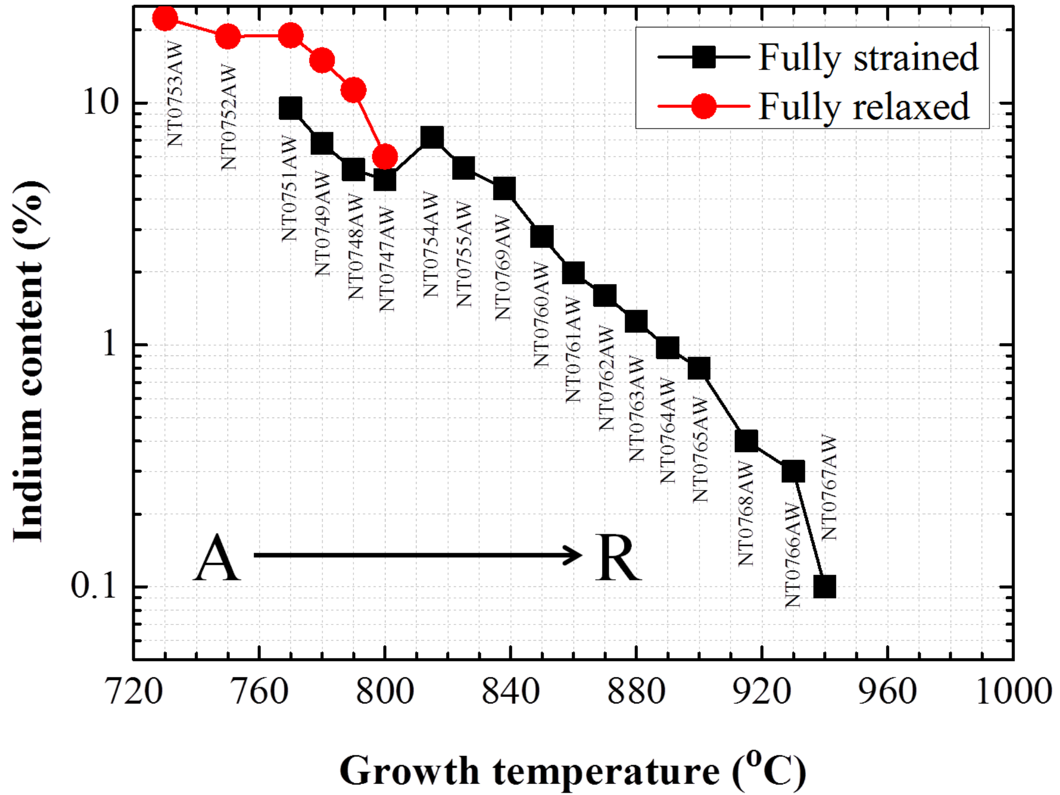

Figure 6.1: InN content of each sample measured using XRD. Plot provided by our collaborators at Tyndall National Institute. Black points represent fully strained layers and red points fully relaxed. Sample letter increases from A to R with increasing growth temperature.

6.3 Sample Quality

Secondary electron images of samples G (NT0754), H (NT0755), I (NT0769), J (NT0760), L (NT0762) and O (NT0765) are shown in Figure 6.2. These were taken under low vacuum conditions in the ESEM to illuminate charging effects and surface contamination. All samples show dark spots evident of pits (V-defects) whose density varies between samples as presented in Table 6.2. V-defects are often evident on the surface of indium containing nitrides [160, 161, 162].

Relating the defect densities back to the growth parameters we can see that the samples with the higher growth times have the lowest density values of the set, but have increased pit size. The larger V-defects are evident in Figures 6.2(a),(c) and (f) for samples G, I and O, which are some of the thicker samples

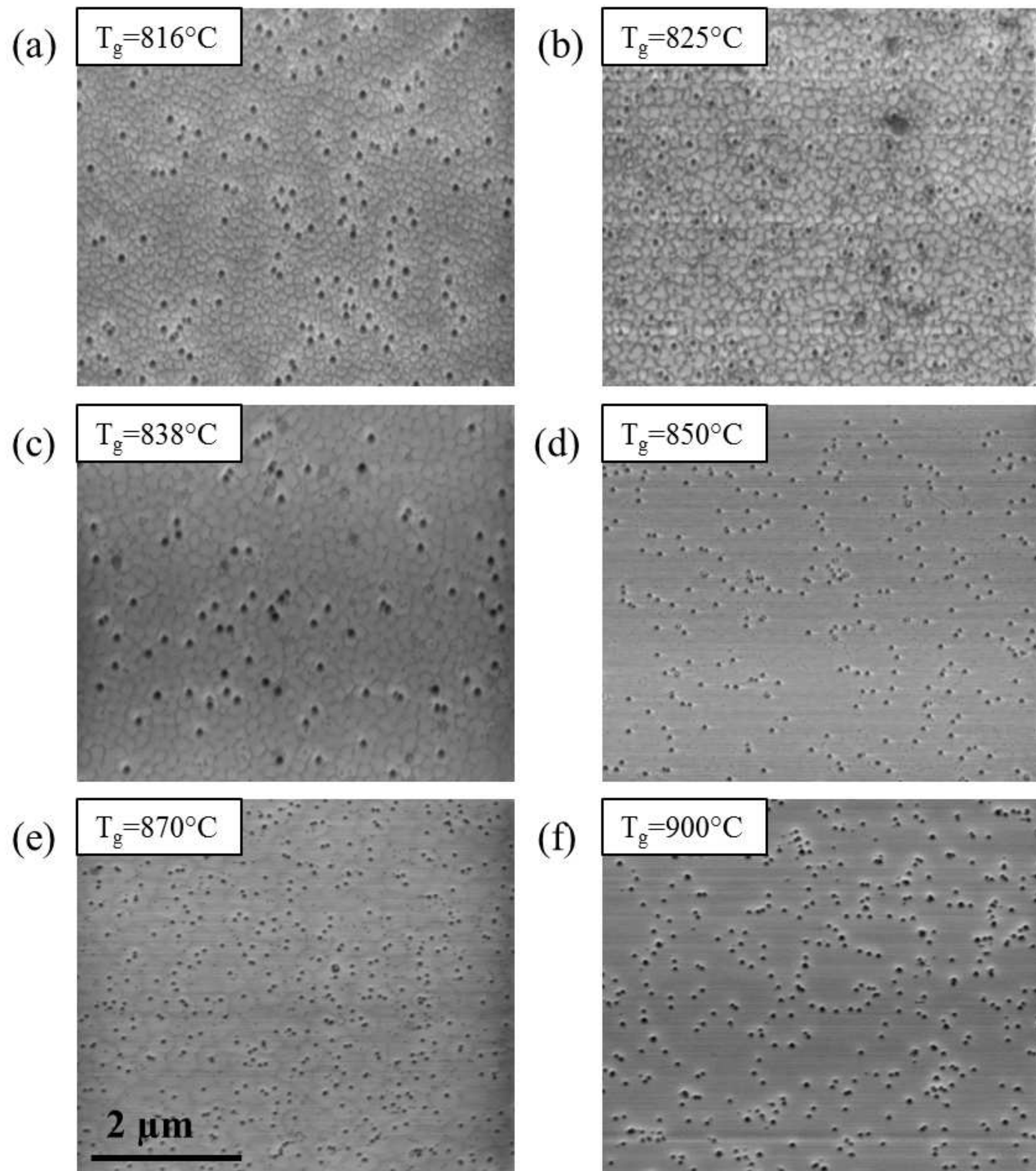

Figure 6.2: Secondary electron images taken in the ESEM in LV mode of samples (a) G (b) H (c) I (d) J (e) L (f) O.

out of the measured set (see Table 6.2). This was seen by Vennegues et al and other groups where the in-plane widths of the pits increased with layer thickness [163, 164]. The reduction in pit density with increasing thickness and decreasing temperature (illustrated in Figure 6.3) is unexpected as it is found that with InAlN on GaN an increase in pit density is associated with increased thickness

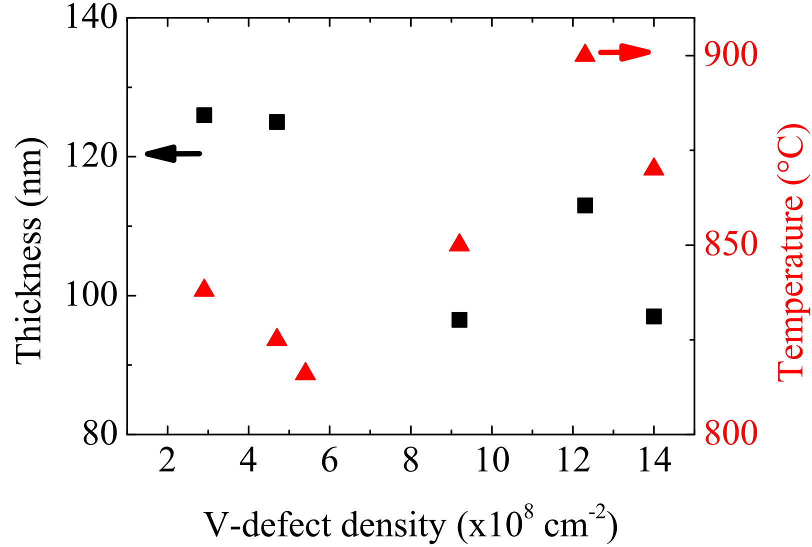

Figure 6.3: Relationship of V-defect density with change in growth temperature and thickness.

Sample	Defect density ($\times10^8$ cm^{-2})	Thickness (nm)	InN (%)
G (NT0754)	5.4	100	7.1
H (NT0755)	4.7	125	5.35
I (NT0769)	2.9	126	4.4
J (NT0760)	9.2	96.5	2.77
L (NT0762)	14.0	97	1.7
O (NT0765)	12.3	113	0.75

Table 6.2: Approximate densities of the V-defects evident in Figure 6.2, along with the measured thicknesses and InN contents from XRD measurements.

and InN content [151]. This dependence is a result of growing on AlN layers. The strain now increases from zero for low InN as opposed to growth on GaN where the lattice match point occurs for $\sim$17 % InN, but variations in the AlN templates will also influence the resultant surface quality of the InAlN layer. It is not possible to separate these effects for this sample set.

Samples G, H, I and L exhibit similar round 'hillock' like features on the surface which reduce in density and visibility from G–L. These hillock features are common in MOCVD grown InAlN layers [160]. Samples J and O appear to have a smoother surface with no visible 'hillocks' from the SE images. This suggests

that the increase in growth temperature (see Table 6.1) aids in the removal of these features improving surface quality. Others have reported this relationship [165], with the increase in temperature leading to greater surface diffusion and a reduction in InN content resulting in reduced strain and better sample quality.

6.4 Compositional Characterisation

WDX qualitative spectral scans were performed initially to check for any Ga x-ray signals due to the previous studies (Chapter 5) showing that Ga auto-incorporation can occur due to residual Ga left behind on the walls and pipes of the MOCVD reactor [147, 153, 166]. A 4 keV beam was used as x-ray excitation for the top InAlN layer and through to the underlying AlN layer of sample O. The x-ray spectrum of the TAP crystal (used for Ga L_α detection) is displayed in Figure 6.4. It reveals no presence of Ga auto-incorporation with the Ga L_α line indicating no counts from the measured spectrum. The strong Al K_α peak and smaller K_β are evidence of the AlN within the InAlN layer and also from the AlN underlying buffer layer. This shows that a combination of reactor cleaning and change in buffer eliminates Ga incorporation in InAlN layers. Changing the buffer to AlN is an important factor as nominally grown InAlN/GaN HEMT structures which were discussed in Chapter 5 did not fully remove the Ga ($\sim$1 %) even with the same reactor cleaning performed between the GaN and InAl(Ga)N growth.

Reliable composition data needs comparable sample and standard, which in this case is most likely going to be achieved by having a carbon coating on both in order to increase conductivity within the samples. Before WDX quantitative results could be obtained a test was performed to see the influence of charging effects on the composition. This is due to AlN being fairly insulating and the samples in this work having large AlN contents in the layers. The influence of the underlying AlN must also be considered. To reduce the effects of charging a small coating of carbon is used to increase conductivity on the surface (in addition to the adhesive silver paint which acts as a ground for current flow within the sample). This is performed in a BAL-TEC CED 030 carbon thread evaporation unit. The sample is positioned at a chosen distance underneath the carbon thread which determines the thickness of carbon applied to the sample surface. The further the distance the thinner the coating. In this case the InAlN/AlN samples were

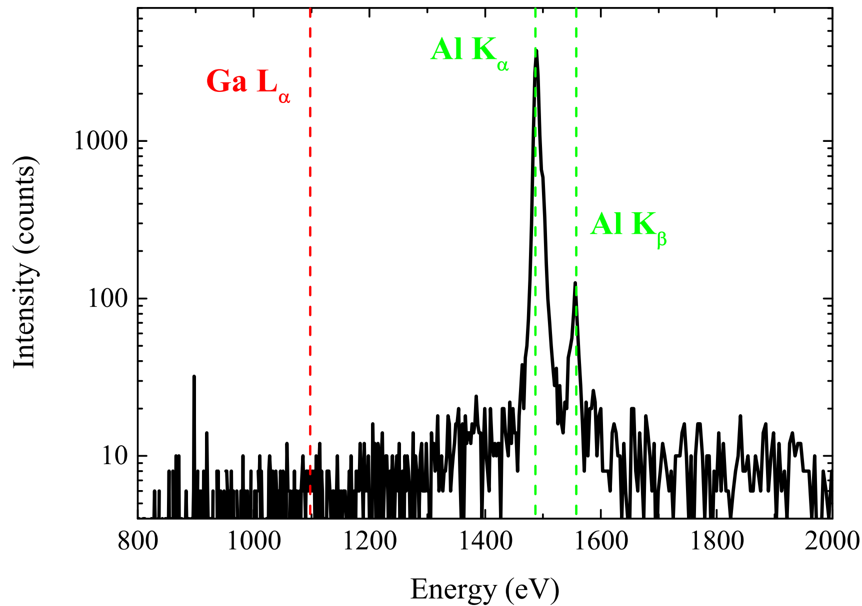

Figure 6.4: An example WDX spectrum from the TAP crystal using a 4 keV beam which reveals no presence of Ga. The Al K_α and K_β are also shown as evidence to a strong Al signal.

placed at ∼12 cm from the thread which results in a coating of ∼5 nm. The sample and thread are enclosed in a glass chamber and the system is pumped down to a vacuum of $\sim 10^{-2}$ mbar. A high current is sent across the thread which evaporates the carbon, coating the sample uniformly. Carbon is often the coating material used for microanalysis due to its excellent transparency and electrical conductivity [90]. It can however pose problems when studying soft x-rays as carbon can absorb x-rays with energies <1 keV [97].

Qualitative scans were performed using a 5 keV beam on a selection of uncoated and carbon coated samples for comparison. As WDX is a surface sensitive technique the effects of the small amount of carbon on the surface are also investigated. Figure 6.5 presents the x-ray spectra of sample H measured on carbon coated and uncoated pieces of sample. The spectra detected by PC1 crystal in Figure 6.5(a) shows a strong N K_α and a small O K_α peak of the same intensity for both uncoated and coated samples. A small C K_α peak is visible in the coated sample spectrum giving evidence of the carbon coming from the coating. These features are also evident in the PC1 spectra of other samples. This illustrates

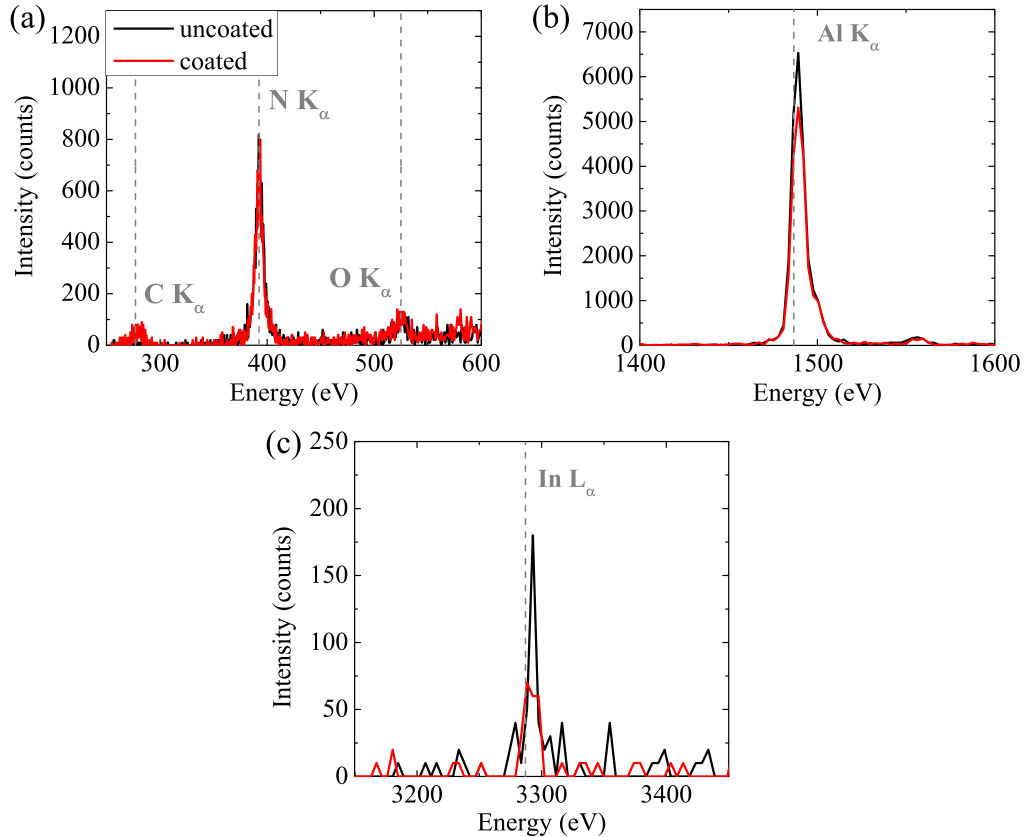

Figure 6.5: Full qualitative x-ray scan of each crystal (a) PC1 (b) TAP and (c) LPET, comparing x-ray counts of sample G with carbon coating (red line) and without (black line). A 5 keV beam was used and x-rays from Al, In, N and O (also C for coated sample) were detected. The grey dashed lines indicate the tabulated x-ray energies.

that the coating of carbon has little or no influence on the light elements in the film. The detection of O is perhaps due to the samples undergoing some surface oxidation after growth. There is a slight difference between the coated and uncoated spectra of the Al K_α and In L_α x-ray peaks in Figure 6.5(b) and 6.5(c). In both cases the uncoated sample returns higher counts. One would expect the carbon coating to have a greater effect on the light elements than the heavy as they are more susceptible to absorption [97]. The difference in the results is likely due to the change in excitation volume with conductivity, and the fact that these are thin films. As a 5 keV beam was used the x-rays were generated from both the InAlN layer and the underlying AlN buffer layer. By adding the carbon coating

it increased the conductivity and reduced the surface potential allowing the beam of high energy electrons to penetrate further into the sample. This increased the penetration depth and overall sampling volume, resulting in a smaller proportion of x-rays generated in the InAlN layer compared to the uncoated sample. Smaller amount of generated x-rays results in reduced counts detected for the In L_α signals. The situation is more complex for the Al, which is present in both layers. The reduction in Al K_α could be due to the fact that although extra Al x-rays are generated these are at an increased depth in the sample. The N K_α and O K_α remain unchanged as the change in penetration volume has no effect on these signals due to N being stoichiometric through the 2 layers and the O being only on the surface.

WDX quantitative analysis was performed to gain insight into the effect of carbon coating on the resultant composition. Initial measurements were taken from a selection of samples (H, I, J, L and O) without any carbon coating at varying beam energies (4 keV, 5 keV and 6 keV). The results revealed high total weight percents (average ∼120 %) and low N percents (average ∼45 %), both of which varied with beam energy. These values are used as a validity check of the measurement and should be close to 100 % and 50 %, respectively. The weight % decreased and the N % increased with increasing beam energy over the sample set. These results suggest that there is over sampling in the sample compared to the standard, but with increasing beam voltage the penetration volume is becoming more comparable with that in the standard. This may be a consequence of charging effects as low beam energies will be influenced more by charging than higher beam energies.

Following this result the carbon coated pieces of the samples were measured. The average total weight % and N % values were ∼90 % and ∼48 %, respectively. The weight % increased and the N % decreased with increasing beam energy, unlike the uncoated sample. The N % is closer to the required value but the weight % is still too far from the 100 % to deem the measurement accurate. This suggests there is under sampling in the sample compared to the standard. By coating the sample, but not the standard, in carbon the penetration volume and x-ray generation are not comparable.

The final WDX quantitative measurement was carried out using both carbon coated samples and standards (AlN and InP) in order to have comparable sam-

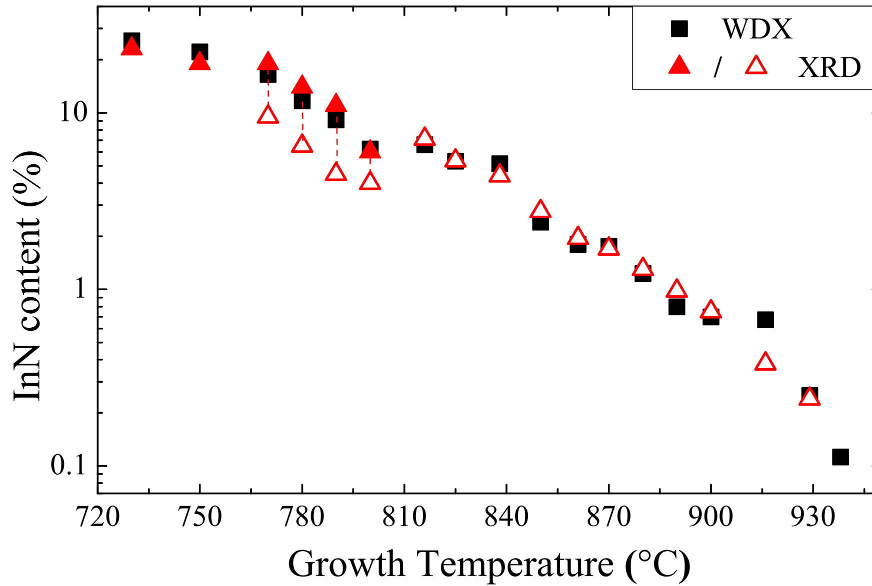

Figure 6.6: InN content as a function of temperature measured by WDX and XRD. The open triangles represent the InN values determined by XRD when the layer is simulated as fully strained (see Figure 6.1).

pling. The results revealed an average total weight % of ∼102 % and N % of ∼50 %. The N % did not vary with increasing beam energy and the weight % decreased only slightly. This indicates that an accurate measurement is achieved, and the discrepancy in the weight % could be due to a small amount of carbon being detected but not accounted for in the correction process and in determining the k-ratios.

The composition was initially determined by using the layers analysis software as described in Chapter 3. Quantitative data was taken for all samples at beam energies of 3 keV, 4 keV, 5 keV and 6 keV, and the composition was varied until the optimum fit was achieved. The thickness was obtained through XRD measurements and was fixed during the fitting process. It was found that for the first set of measured samples (H, I, J, L and O) the InN content from fitting the k-ratios at each beam energy was equivalent to that determined by using 5 keV alone. Also there was minimal change in composition over the measured beam energies. Therefore the InN contents for the rest of the samples were determined using a 5 keV beam. These are presented in Figure 6.6 as a function

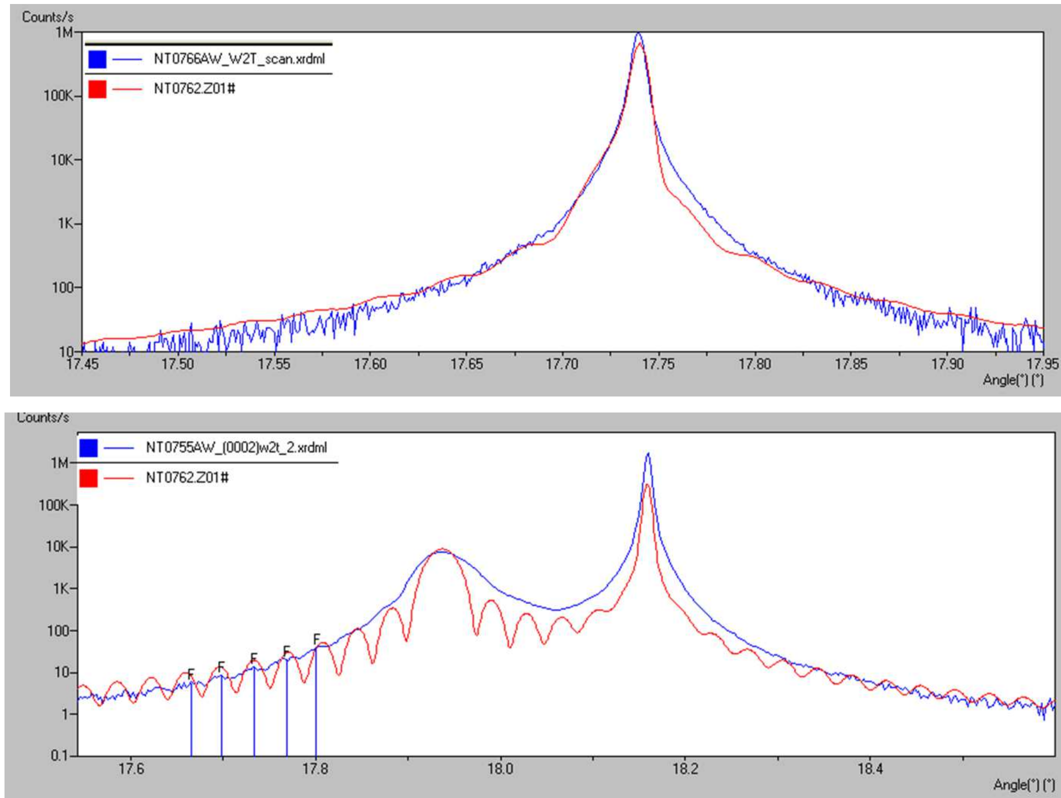

Figure 6.7: ω-2θ (0002) XRD scan of (a) sample Q with a growth temperature of 929°C and InN content of 0.24 %, and (b) sample H with growth temperature 825°C and InN content of 5.3 %. The sharp peaks correspond to the AlN layer and the broad peak corresponds to the InAlN layer. The InAlN and AlN peaks have overlapped in (a) for sample Q. The measured spectrum is shown in blue and the simulated fit is shown in red.

of growth temperature. A comparison is made with values determined by XRD ω-2θ (0002) scans as shown previously in Figure 6.1. A good agreement between the techniques can be seen for all samples, covering a wide range of compositions. The open triangles in Figure 6.6 represent the XRD InN content results for the selected samples (C–F) when the layer is said to be fully strained. The connected filled triangles represent the InN content for fully relaxed layers. The WDX results are in good agreement with the fully relaxed values which confirms that the samples <810°C are fully relaxed.

Interestingly the WDX and XRD results are comparable even at low InN values (<1 %), where discrepancies are likely to occur. For the samples with

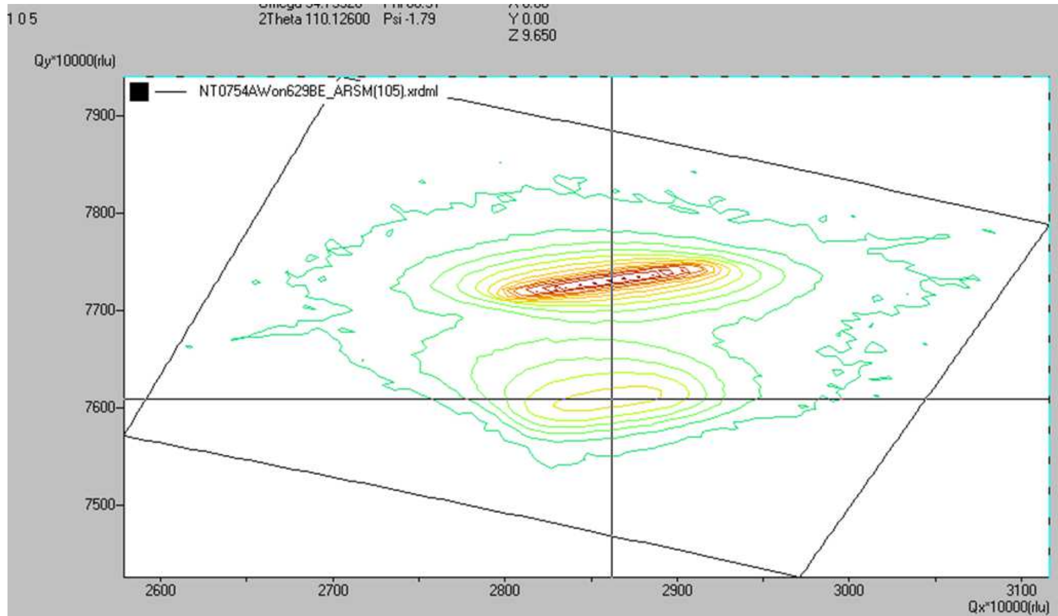

Figure 6.8: An RSM of sample G showing no relaxation.

lower InN contents the spectra from the ω-2θ XRD scans are harder to fit due to negligible Pendellösung fringes and the overlap of the InAlN and AlN peaks. This makes it difficult to determine the composition. An example is shown in Figure 6.7(a) for sample Q where the InN content is found to be 0.24 % from XRD and 0.25 % from WDX. An ω-2θ XRD scan for sample H, with an InN content of $\sim$5.3 % is presented in Figure 6.7(b). It illustrates the two defined peaks from the InAlN and AlN layers, not resolved in Figure 6.7(a). As the InN content is reduced the InAlN peak moves towards the AlN peak causing overlap as seen for sample Q. Sample R is not shown in Figure 6.6 for XRD as the composition could not be determined. The InN content is found by WDX to be 0.1 %, which highlights the advantages of WDX over XRD for measuring low compositions. This is seen by others where WDX is compared with RBS for samples with dilute compositions [79].

Information on the strain of these samples was provided by our collaborators at Tyndall Institute through RSM measurements. A selected sample set were measured and showed to be fully strained to the underlying AlN. An example RSM is shown in Figure 6.8 for sample G where the InAlN and AlN satellites have the same Q_x value, and therefore the same a lattice parameter. This gives

evidence of the sample having strain along this plane. Further measurements show samples G-R also to have strain. Sample A-F are found to be fully relaxed as was shown with the composition measurements in Figure 6.6.

6.5 Optical Characterisation

The optical properties of these InAlN epilayers were studied using room temperature CL. As the measurements were taken under low vacuum (0.1 mbar) in the ESEM the samples did not require carbon coating as the low vacuum mode reduces charging effects. The beam energy used for generating the CL signal was 5 keV. Single point CL spectra were taken on different areas for samples G, H, I, J, L and O. The samples gave weak luminescence with low emission intensity. An example spectrum is presented in Figure 6.9 in black for sample L. It shows a broad InAlN luminescence with a linewidth of ∼700 meV. Note that no near band-edge luminescence of AlN was detected (at ∼6.2 eV). A check was carried out to determine the scope of the CCD detector and collection efficiencies at these high energies. The CL of an InAlGaN/AlN epilayer sample was measured under high current conditions. A small peak around 6 eV of AlN related emission was present in the spectrum as shown in red in Figure 6.9 giving evidence that high emission energies can be detected. Although a long acquisition time and large slit was needed to obtain the spectrum.

The rest of the samples in the subset were found to give similar spectra to sample L, with broad luminescence and no AlN emission detected. The spectra are presented in Figure 6.10 with an offset applied to each spectrum for clarity. A variation in peak emission energy with InN content across the measured spectra is evident but there is no clear dependence on FWHM. Each spectrum was fitted using a Gaussian peak fit allowing the peak energy and FWHMs to be determined. These values are plotted as a function of InN content in Figures 6.11(a) and 6.11(b).

From Figure 6.11(a) there is argument for a negative relationship between peak energy and InN content. All samples except one lie on the trend of decreasing peak energy with increasing InN content. This may imply bandedge luminescence as this follows the same well known red-shift relationship with increasing InN [167, 168]. However the peak energy values are lower than expected for the

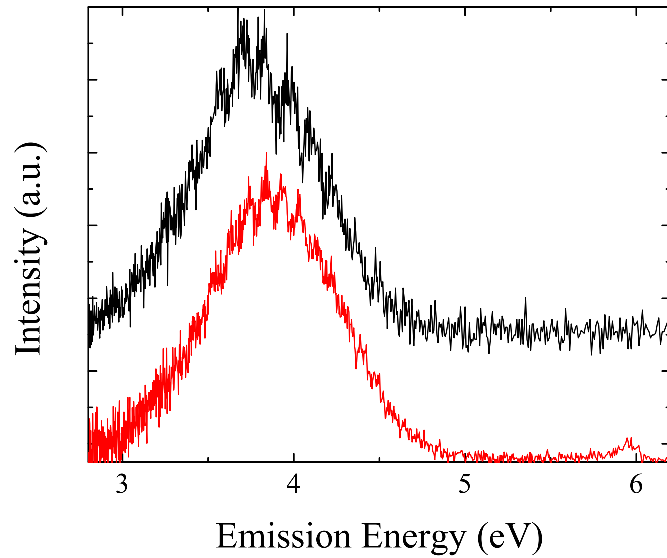

Figure 6.9: A CL spectrum of broad InAlN related luminescence with no evidence of AlN luminescence at ~6.2 eV (black line) and a CL spectrum of an InAlGaN/AlN epilayer sample with a small peak around 6 eV of AlN related emission giving evidence that high energies can be detected (red line). An offset is applied to the spectra for clarity.

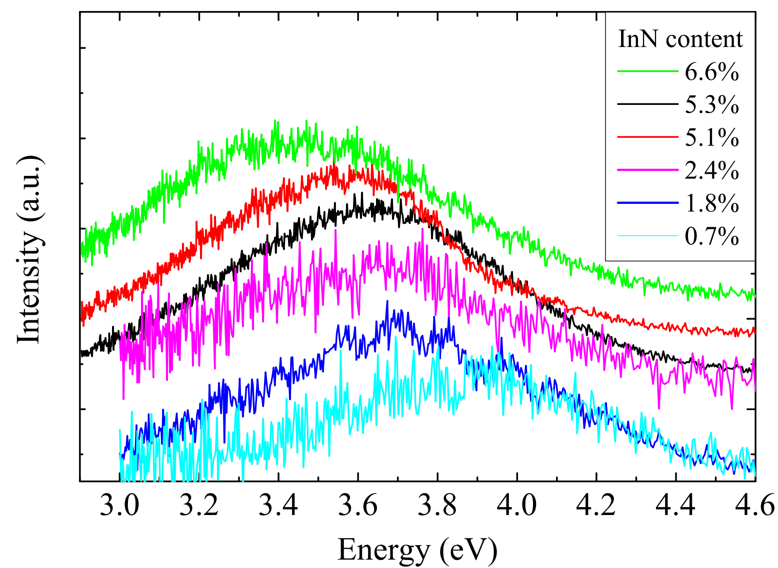

Figure 6.10: CL spectra of broad InAlN related luminescence.

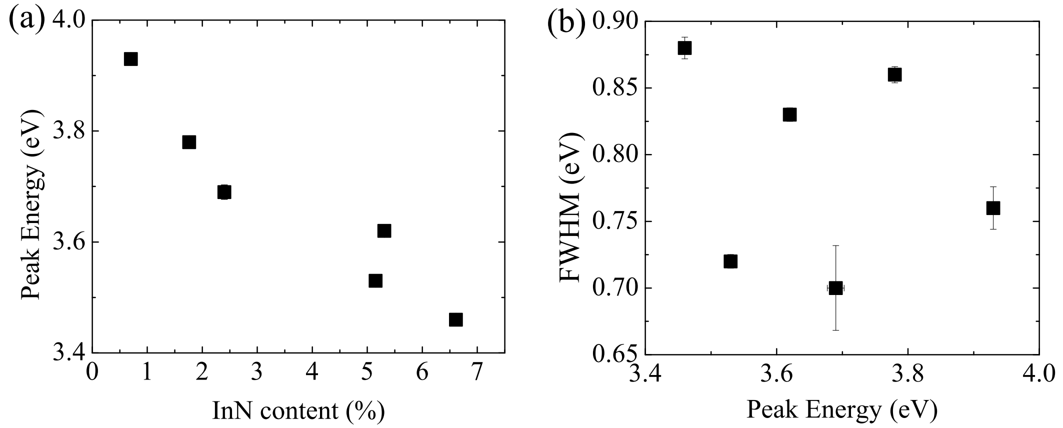

Figure 6.11: (a) Peak energy position variation with InN content of the spectra shown in 6.10. (b) FWHM as a function of peak energy.

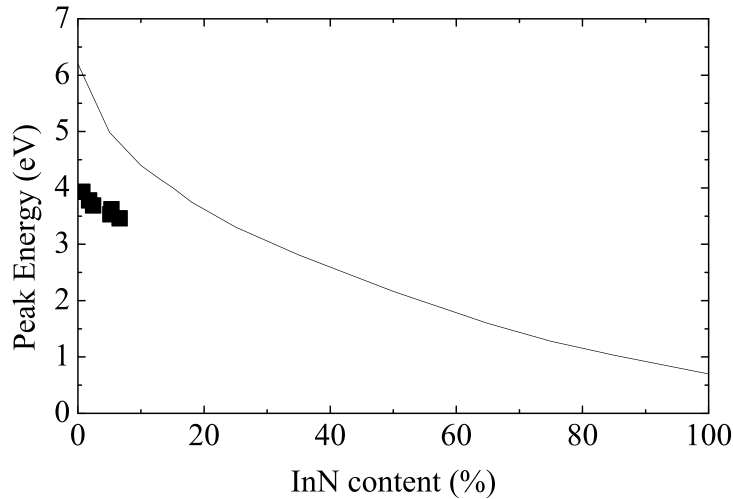

Figure 6.12: The CL peak energy results in relation to the InAlN band bowing calculated by Schulz et al using a tight-binding (TB) model [60].

measured InN contents [67]. This is clear when plotting them alongside the compositional dependent bandgap bowing for InAlN calculated by Schulz et al [60] using a tight-binding (TB) model as shown in Figure 6.12. RT PL measurements performed at Tyndall confirm these results (see Figure 6.13), with similar peak energy and FWHM values. A negative peak energy dependence with increasing InN content is also found.

PLE measurements also performed at Tyndall reveal a large Stokes-shift of

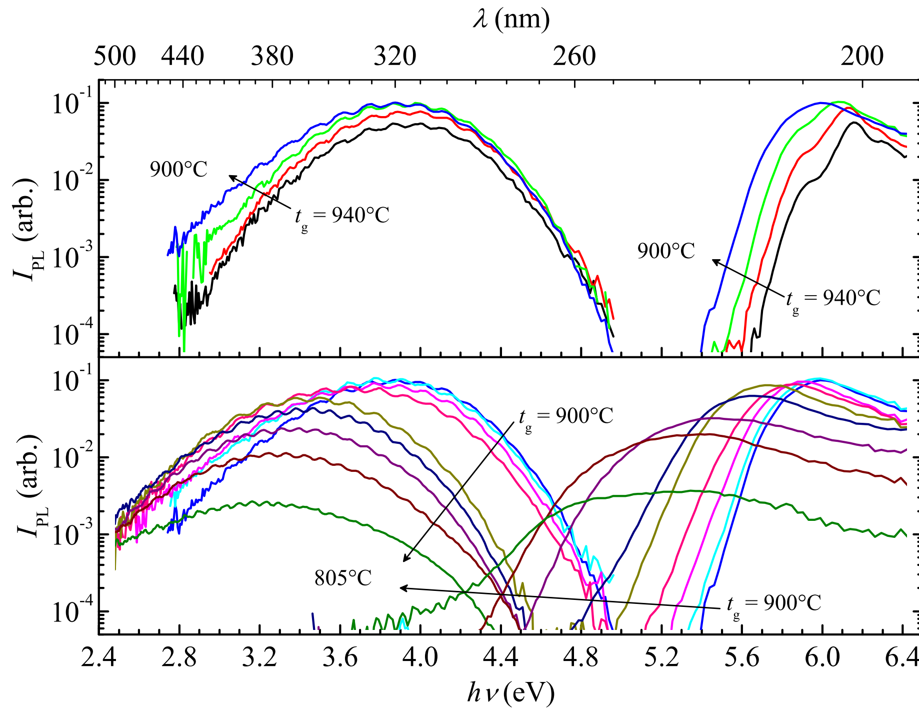

Figure 6.13: RT PL and PLE spectra from Tyndall of InAlN epilayers grown at different temperatures. PL spectra is shown on the left (lower energy) and PLE on the right (higher energy).

up to ∼2 eV between the excitation and emission spectra as shown in Figure 6.13. Butté et al found similar Stokes-type shifting in the emission of their RT PL measurements of InAlN layers compared to the bandedge, which they determined through RT reflectivity measurements [45, 169]. The difference between the PL luminescence and the bandedge can be attributed either to In fluctuations, or deep defects and/or impurities acting as recombination centres. Looking at the variation in FWHM with peak energy in Figure 6.11(b) there is no clear dependence. This dependence is usually due to the increase in alloy fluctuations with increasing InN content. However in this case the alloy fluctuations would be particularly high even with small amounts of InN being incorporated into the lattice, as the results show very broad luminescence with the values of the fit-

ted FWHMs being exceptionally large (approx. 0.7 eV to 0.9 eV) even for low InN contents (0.22 % InN -from PL/0.7 % InN - from CL). This suggests that localisation is perhaps not due to alloy fluctuations.

Relating these optical properties back to the sample quality in Figure 6.2 we can see that the samples with FWHM values >0.8 eV (G, H and L) have the 'poorer' surface with either increased v-pit densities or the highest density of 'hillock' like features. The samples with FWHM values <0.8 eV (I, J and O) have the 'smoother' surfaces or the lowest v-pit density.

6.6 Summary

The compositional and optical properties of a large set of ∼80–150 nm InAlN epilayers grown on AlN buffers by MOCVD were investigated. Surface and structural properties were also presented for selected samples. The SE images revealed variations in sample quality, with the samples grown at higher temperatures having smoother surfaces. The XRD RSM measurements found the samples grown T>800°C to be fully strained to the underlying AlN and those grown T<800°C to be fully relaxed.

The InN content was varied by decreasing the growth temperature. WDX and XRD measurements revealed a wide range of InN contents from 0.1% to 25.6%, with a high agreement between the techniques over the whole composition range. The WDX compositional analysis revealed no presence of Ga within the samples after reactor cleaning and growing the InAlN on AlN buffers.

CL measurements produced broad InAlN luminescence spectra which varied with InN content. The peak energy was found to be 3.46–3.93 eV for InN compositions of 0.7–6.6 %. Further analysis suggests this is not bandedge emission due to the low peak energy and very wide FWHMs when compared to predicted and measured values. The luminescence could be due to high alloy fluctuations within the poor quality material although this is questionable for the low InN (0.22 %) containing samples.

Chapter 7

Luminescence Studies of InGaN Through Photoluminescence Mapping

7.1 Introduction

Photoluminescence (PL) spectroscopy is a useful method for characterising light emitting semiconductors like the III-nitrides, as introduced in Chapter 3. It can provide information on bandgap, structural properties, defects and internal quantum efficiencies (IQE) of the material under study. Looking at the spatial dependence of PL allows a deeper insight into the materials properties and behaviour to be obtained. Low temperature (LT) measurements can also be performed which can be useful in comparison with room temperature (RT) CL. In this Chapter the design and operation of a home built PL mapping system is demonstrated, along with some initial results. An investigation of InGaN/GaN quantum well (QW) LED samples grown under different barrier temperature methods is also presented. Both RT and LT mapping of these samples have been made, with preliminary work on a new characterisation method, IQE mapping, discussed.

Figure 7.1: Photo depicting PL mapping with moving nanopositioners and sample luminescence. The sample is mounted on to a metal stub which is connected to the movable positioners and a reflecting objective is used to focus the laser light and collect the emission from the sample. The size of the positioners are given for scale purposes.

7.2 Photoluminescence Mapping System

7.2.1 Design and Set Up

The design of the home built PL system is outlined in Chapter 3 with the schematic shown in Figure 3.20. As mentioned previously in Chapter 3, the system adopts a vertical microscope design which has the advantage of imaging the sample surface, and also allowing easy control over the location of the laser spot. This design also limits the number of optical components which may otherwise reduce the laser power that reaches the sample surface. The set up has the use of 2 lasers, a 325 nm HeCd laser and a 405 nm laser diode. For measurements within this chapter only the HeCd laser has been utilised, providing short wavelength (325 nm), good mode quality (TEM_{00}) and reasonable power

(17 mW). This aids in the reduction of the spot size by improving the diffraction limit, in order to achieve micron scale resolution with good power density. This is defined by the Rayleigh criterion:

$$d = \frac{1.22\lambda}{NA} \tag{7.1}$$

where d is the diameter of the laser spot, λ is the wavelength of the laser, and NA is the numerical aperture of the focusing lens (in this case the reflecting objective). An additional factor implemented was the inclusion of a beam expander which aids in filling the reflecting objective, giving a more tightly focused spot (see section 7.3.1). Also the reflecting objective was changed to one with a higher NA (from 0.4 to 0.5) (and UV coating) to aid in the reduction of spot size (and power loss). This resulted in an ideal theoretical spot size of $d \approx 0.8$ µm. For the system's mapping capabilities a set of Attocube nanopositioners (and the motion controller) were used along with a modified version of the *CHIMP* software. *CHIMP* was implemented for positioner control, spectral acquisition, hyperspectral imaging and data analysis. A detailed description of the operation of the nanopositioners is provided in the subsequent section.

7.2.2 Operation of Nanopositioners

The positioners used for sample movement and mapping are a pair of Attocube ANPx101 nanopositioners. These positioners were chosen as they provide the necessary range of movement while still being small enough to fit inside the cryochamber. Stacked with one at 90° to the other provides x and y movement across the focal plane. The sample is brought into focus using a manual crank in the z-axis, with aid of the camera in the microscope.

The positioners operate using a piezoelectric design and slip-stick principle [170, 171]. An applied voltage (V) drives the piezo from its initial position extending the main body, as illustrated in Figure 7.2(a) by the movement of m_1 and m_2. This drive motion is slow, with the two masses being held together due to friction. The voltage is then dropped to zero contracting the piezo and rapidly retracting m_2. This induces an inertial force which is greater than the frictional force leaving m_1 in position. The main body of the positioner is now displaced by a distance Δx. When operating the nanopositioners a greater voltage will result

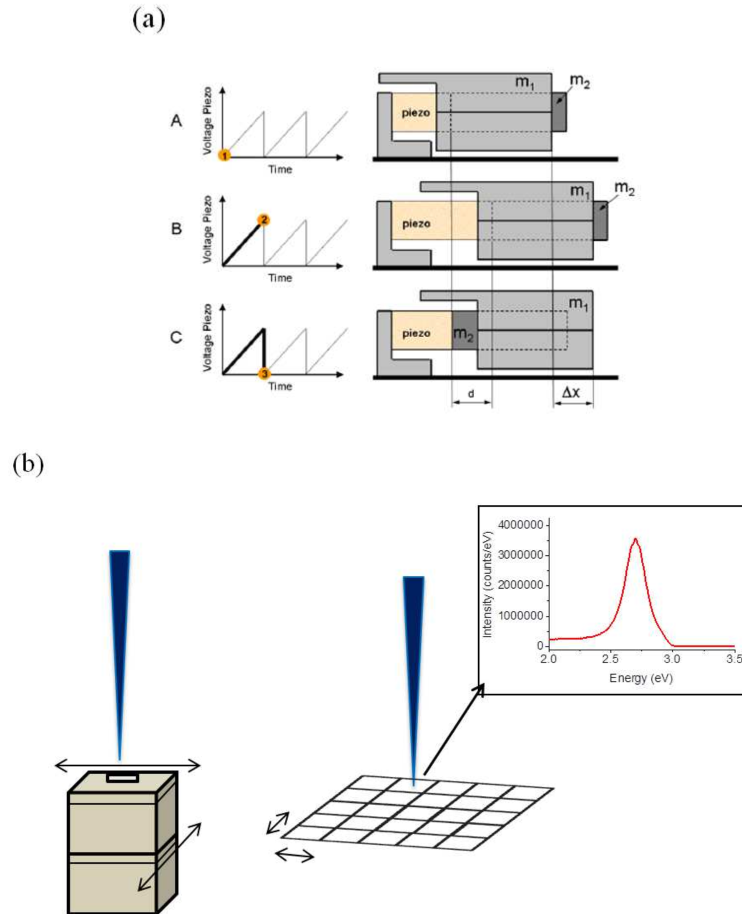

Figure 7.2: Operation of nanopositioners used for PL mapping. (a) Illustrating piezoelectric slip-stick motion. (b) Schematic of the PL mapping and acquisition.

in a larger step size, but due to the piezo nature of the device a relationship between Δx and V cannot be defined. Therefore many small 'steps' are more advantageous for repeatability than one large step. The speed of the stepping motion can be controlled by altering the signal frequency ($f = 1/t$, where t is the time taken to drive the piezo).

7.3 Initial Measurements

This section includes measurements of the spot size using various methods and under different conditions. It also gives details of generating the initial RT and

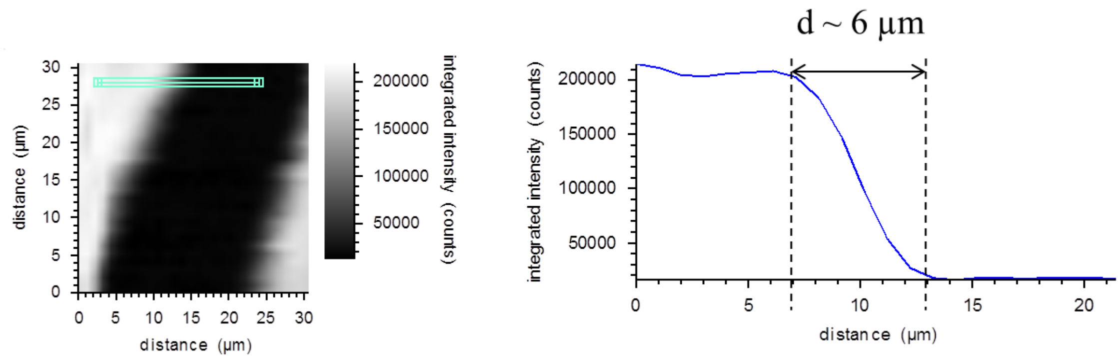

Figure 7.3: Example of edge technique to determine spot size. Mapping of an LED contact using the HeCd laser without the beam expander.

LT maps, the challenges associated with mapping using this type of system, and how these were resolved.

7.3.1 Spot Size Measurement

The spot size was measured in order to determine the optimum resolution of the PL maps. A greyscale image of the spot on the surface of the sample was taken by the camera. Using imaging software an intensity profile of a line through the imaged spot was produced and the FWHM of the fitted Gaussian was used to determine the spot size. This method was inaccurate as the intensity of the profile saturated even with additional filters, resulting in large errors in the fitting. Another approach based on an adaptation of the boundary diffraction wave method was therefore used in order to get a rough idea of the spot size. This follows the principle whereby the laser is scanned over a straight edge of differing optical material to obtain an intensity profile [172]. This is illustrated in Figure 7.3 by mapping an LED contact and extracting the linescan over the mapped edge. The spot size (ω) is determined to be ω ~5 μm in diameter and is calculated using $\omega = 0.7803d$, where d is the distance between 10 % and 90 % intensity [172]. This is for the HeCd laser with no beam expander.

On adding the beam expander the spot size is reduced further due to the beam filling the reflecting objective. Evidence of this is illustrated in the PL map in

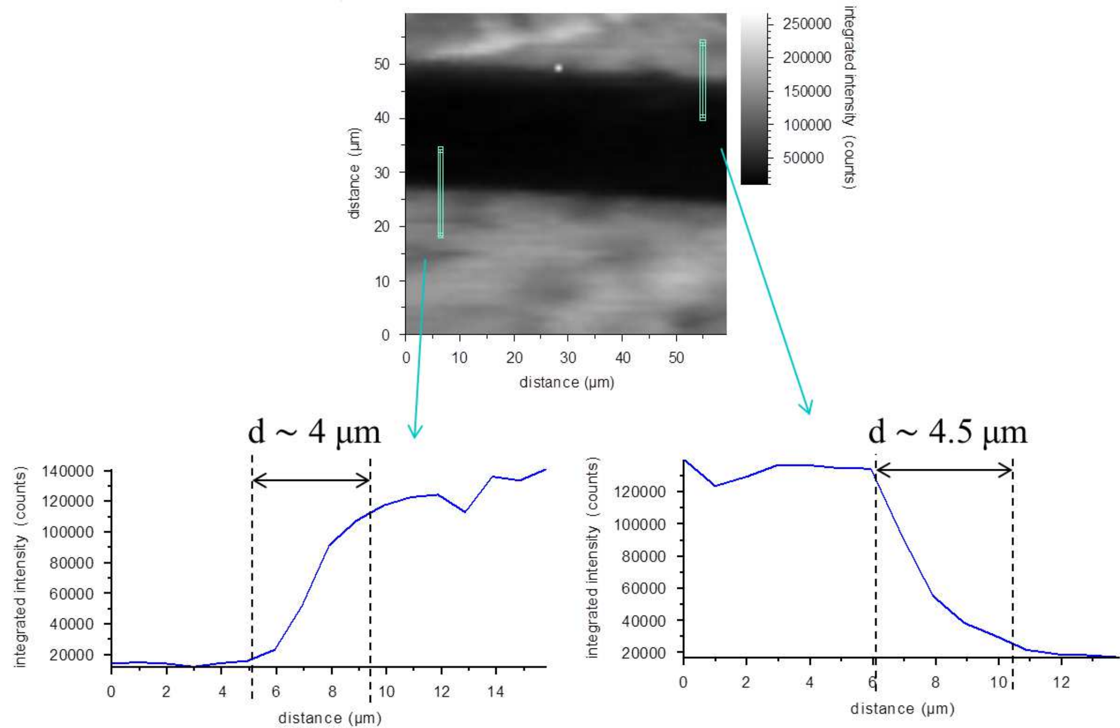

Figure 7.4: Illustrating edge technique to determine spot size for the inclusion of the beam expander.

Figure 7.4 by the edge technique. The spot size has improved and is determined to be ω ~3-3.5 μm. This is only an approximation of the spot size of the laser and has a large error of ~1 μm (~25 %). Additional factors contributing to the larger value spot size compared to the theoretical value could be from not completely filling the objective, carrier diffusion prior to emission, and lens aberrations such as astigmatism, coma, spherical aberration etc. A more accurate value will come from the resolution of the smallest visible features within the measured PL maps.

RT PL intensity maps of InGaN/GaN LED samples, investigated further in section 7.4, revealed dark "spotty" like features of $<$ 10 μm. Linescans over the smallest features produced intensity profiles which were fitted by Gaussian functions. The FWHM of these fitted Gaussians was used to determine a more accurate spot size. The linescan of one of the smallest features resolved is shown in Figure 7.5 and has a FWHM value of 2.9 μm with a standard error of 0.6 μm (~20 %).

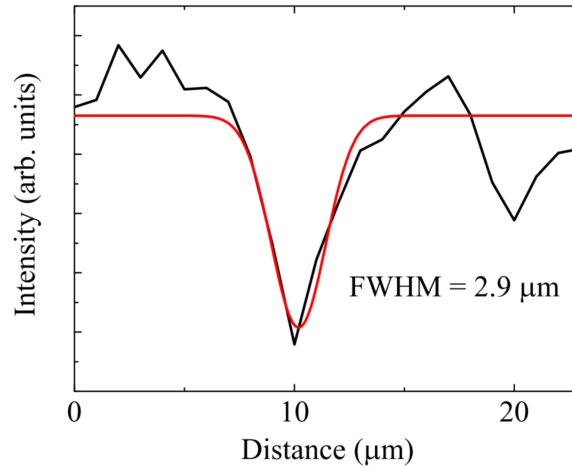

Figure 7.5: Gaussian fitted linescan profile of smallest resolved feature with a FWHM of 2.9 μm.

7.3.2 RT Maps

Room temperature (RT) maps were performed with various step sizes and areas to obtain the optimum stepping sequence, and to calibrate the corresponding voltage (V) and frequency (f) input. Difficulty arose in creating square maps as there is no feedback loop between the nanopositioners and controller, and due to the piezo-nature of the devices the step size varied. Metal grids with a square pattern were used for calibration of step size, map size and to insure maps were square. An example of this calibration method is given by the RT map in Figure 7.6. It highlights the influence of the variation in step sizes, as the grid (which is shown as the dark regions) is shifted at the bottom of map. We can see from the figure that in this case the $-x$ direction steps are larger than the $+x$ steps as more of the grid is sampled. Another possible influence could be that the positioners stop for spectral acquisition (after a number of steps) in the $+x$ direction but not on the return.

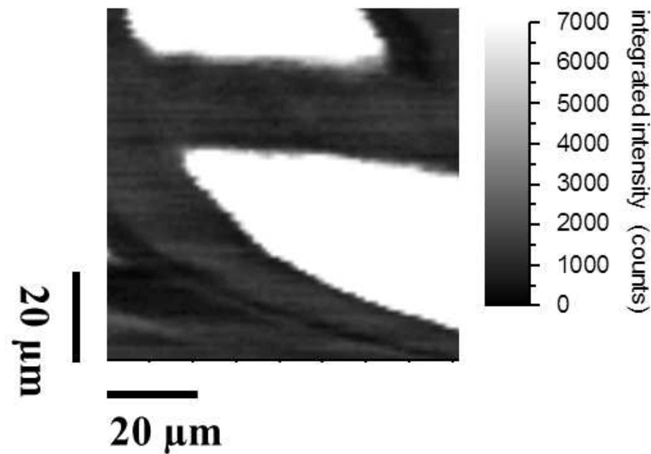

Figure 7.6: RT map of a square metal grid highlighting the variation in step size from one direction to the other.

7.3.3 LT Maps

LT maps were performed in a similar way to the RT maps. An additional issue here is that the repeated motion of the cryopump piston caused the nanopositioners to vibrate, as they were situated within the cryochamber at the end of the coldhead. The vibration causes the sample to move in and out of focus and has influence on the PL maps, where a periodic crosshatch pattern can be seen across the map as shown in Figure 7.7(a). To reduce this effect the surrounding coldhead was weighted down to minimize the vibrations. This proved unsuccessful as the positioners are sensitive to the smallest of movements. In addition to the crosshatch effect the piston had influence on the repeatability of the step size of the positioners as features look stretched along the x-direction. To rid the effect of the piston movement the cryopump was switched off at the start of acquiring a map. This method removed the crosshatch effect but resulting in the positioners drifting as shown in Figure 7.7(b). Also turning the cryopump off will result in an increase in temperature as the map is acquiring, but this should have little impact on the map if kept within a small range (see caption for details).

Before investigations into the RT PL properties of InGaN/GaN LED samples (next section) attempts at resolving the LT PL mapping issues (as described in this section) were made in order to gain LT spatial PL properties of these samples.

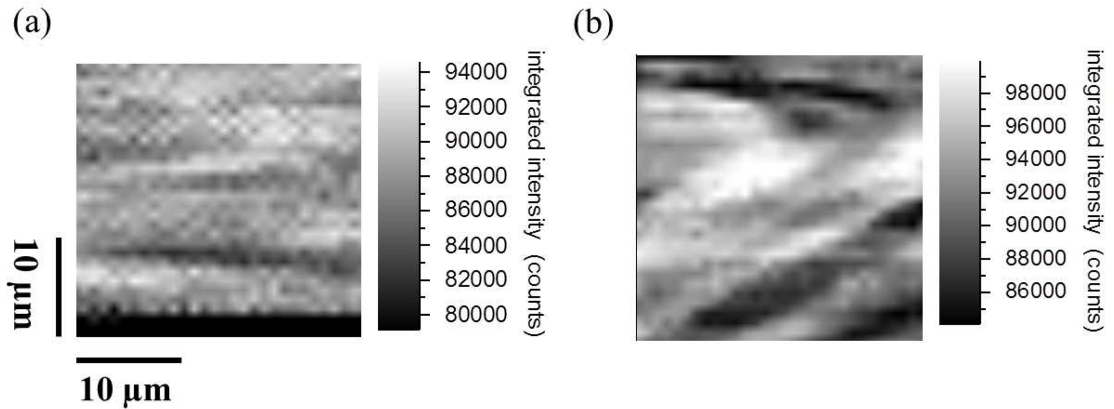

Figure 7.7: (a) LT map (T∼19K) with cryopump on throughout measurement. (b) LT map with cryopump turned off at start of map acquisition. T at start of map ∼19K, T at end of map ∼39K.

The crosshatch effect issue was overcome by timing the spectral acquisition to the frequency of the cryopump piston. This reduced the visible effect within the maps as shown in Figure 7.8. The issue that was difficult to correct for was the positioner drifting. This is seen in the map in Figure 7.8. The solution to the RT step size variation problem (provided in section 7.4.2) did not work at LT as the positioners moved past the point of their piezo-electrical limit. This implies that the movement of the cryopump piston is inflicting a mechanical stress in the positioners causing them to move beyond their range. Due to the drifting and movement of the positioners the repeatability capabilities is affected, therefore an attempt at IQE mapping could not be achieved as this would require the same area to be mapped at RT and LT.

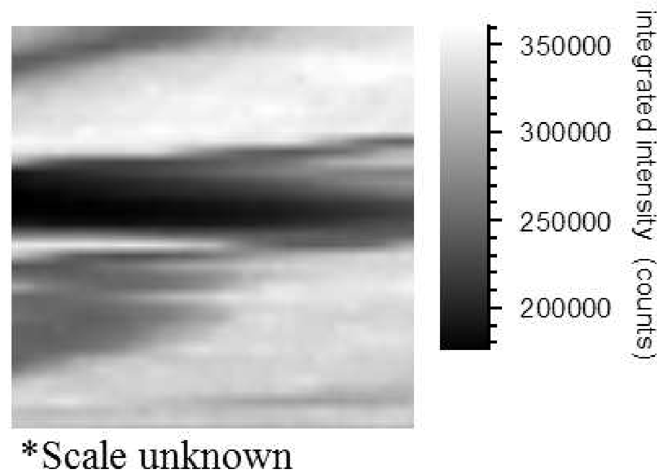

Figure 7.8: LT map of the 2T sample with no crosshatch effect but showing positioners drifting. Scale unknown due to inability to calibrate.

7.4 InGaN/GaN LED Structure Samples

The samples under study using the PL mapping system are InGaN/GaN multi-quantum well (MQW) LED structures grown under different barrier growth methods. These samples were chosen to test the resolution of the PL system as previous studies on similar samples using CL, EL and EBIC hyperspectral imaging showed features of around 5–10 μm [173, 174]. Also comparisons to the other techniques can be made, with the additional possibility of LT, to help resolve the origin of these features.

7.4.1 Sample and Experimental Details

The InGaN/GaN LED structures were grown by MOCVD at University of Cambridge. A 5 period MQW active region was grown on ∼1 μm n-type doped GaN layer, on thick low dislocation density (LDD) c-plane GaN/sapphire templates, with a 130 nm p-type doped GaN capping layer (see schematic in Figure 7.9(a)). The thickness of the InGaN QWs and GaN barriers were approximately 2.5 nm and 7.5 nm, respectively. Two different growth methods, quasi-2 temperature (Q2T) and 2 temperature (2T), were used to grow the InGaN/GaN active regions of separate structures [175]. The Q2T method commences the growth of

the GaN barrier layer at the low temperature (740°C), used for the InGaN layer growth, for the first few nanometres before increasing the temperature (860°C) for the rest of the barrier growth. This provides a protective cap for the QW and prevents indium re-evaporation during the temperature increase [176, 177, 178]. The 2T method allows a break in growth between the well and barrier to ramp up the temperature from InGaN growth (725°C) to GaN growth (860°C) [179, 180, 181]. This is expected to improve the crystal quality of the GaN barrier, but results in an indium loss in the QW. For both methods, after growth of the GaN barrier there is a break while the temperature is reduced before the growth of the next QW. These methods are illustrated in Figure 7.9(b). Following growth, the samples were processed at University of Bath into full LED structures by adding contacts to the n and p layers. This enables electrical studies to be conducted but these measurements will not feature in this thesis. Both RT and LT PL hyperspectral mapping have been performed on these samples (LT in Section 7.3.3), and the results compared with those from CL on a similar sample set, grown using the two growth methods.

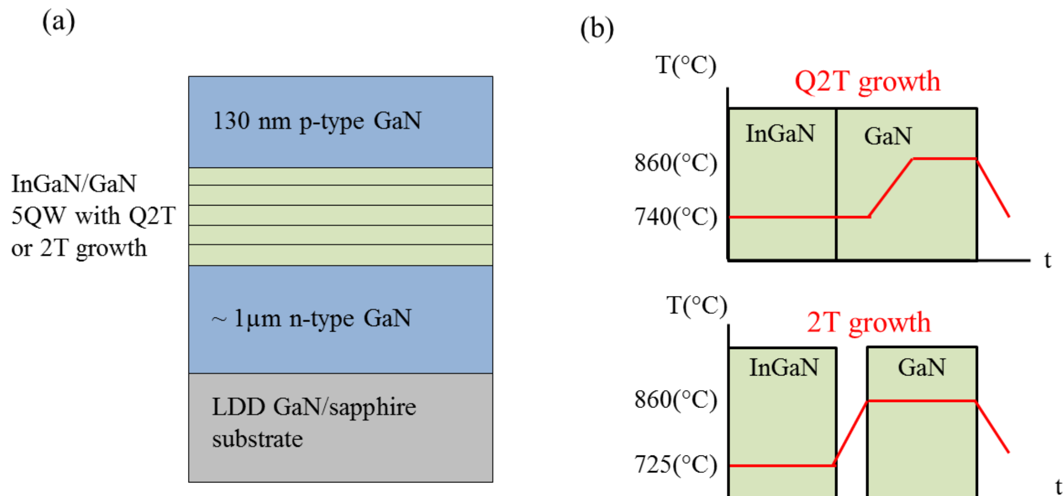

Figure 7.9: (a)Schematic of the InGaN/GaN LED sample structures. (b) Depiction of the barrier growth of the Q2T and 2T methods. After growth of the GaN barrier there is a break for both Q2T and 2T while the temperature is reduced before growth of the next QW.

7.4.2 Photoluminescence Characterisation

Initial RT maps were performed on both Q2T and 2T samples. The excitation power reaching the QWs of the samples was calculated to be $\sim 2.5 \times 10^2$ Wcm^{-2}. To overcome the issue of variation in step sizes for positive ($+x/y$) and negative ($-x/y$) directions (as was discussed previously in section 7.3.2), each positioner was moved to their extreme $-x, -y$ before acquisition commenced. When performing the PL mapping the step sizes were larger on the $-x$ than the $+x$ direction ensuring that the positioner was at the extreme $-x$ at the start of each line. This guarantees the positioner is always starting from the same x point. Spectra were only acquired in the $+x$ direction creating a square map.

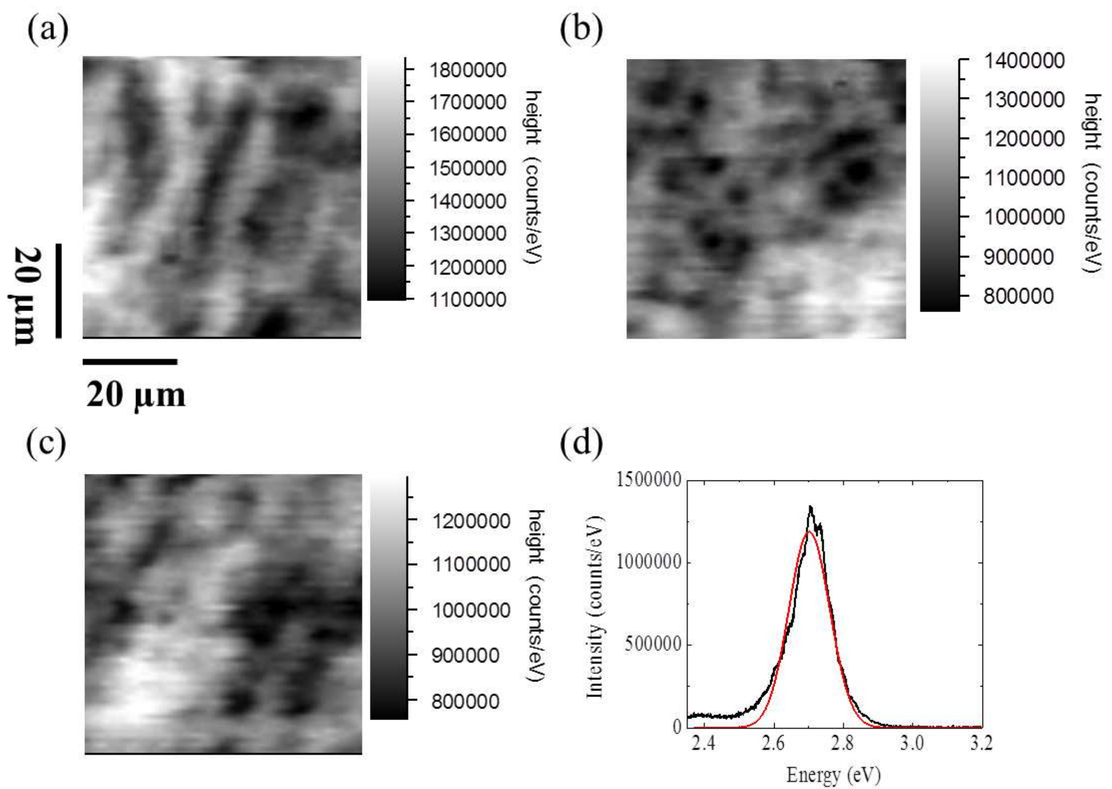

Figure 7.10: (a), (b), (c) Fitted intensity maps of different areas of the Q2T sample. (d) Typical spectrum taken from map (b) showing fitting.

Several 60x60 μm^2 maps were performed on different areas of the Q2T sample to explore the spatial variation of the InGaN QW luminescence. Each of the spectra, acquired at every pixel, were fitted using a Gaussian function. The fitted intensity maps are presented in Figure 7.10, along with an example spectrum. A comparison between the raw data and fitted maps were made, and revealed no difference in map appearance. Also the PL response was not applied to the maps as it would make little or no difference to the overall outcome of the maps due to the minimal variation in the response over the maps energy range. Dark spot-like features of ∼3–10 μm in size are evident in all three maps highlighting areas of non-radiative recombination. These dark spots are comparable with those found through CL measurements by Wallace et al on similar samples grown using the Q2T method, as shown in Figure 7.12(a) [173, 174]. The cause for these dark spots is suggested to be from threading dislocations (TDs) or decomposition effects of the InGaN in the wells, however others suggest thermal degradation of the QW layers is responsible [182]. The TDs could not be resolved using this PL mapping technique. There are also striation like features present in the map in Figure 7.10(a). These can be attributed to several dark spots situated close to each other forming these features, and are not a result of the scanning. The spots are not clear due to the limited resolution of the laser spot.

The maps of the energy of the peak corresponding to the intensity maps shown in Figure 7.10 revealed no spot-like features which correlated with the lower intensity spots. These are presented in Figure 7.11. However, the bright, higher intensity regions within these maps display areas of higher peak energy, i.e. these regions are blue shifted with relation to the rest of the map. This is a common observation in InGaN materials where there is a positive relationship between peak intensity and emission energy, as was also seen in Chapter 4 [183, 184, 121, 185]. The variation in peak energy across each of the maps was minimal (∼20 meV) with the mean peak energy centred at 2.705 eV. Directly comparing the spectra taken from the dark spots and light regions of these maps the intensity is reduced by $6x10^5$ counts/eV on average, and the peak energy is red shifted by ∼6 meV, from light to dark. This differs to the CL results by Wallace et al [173, 174], where the peak energy is blue shifted by 10–40 meV on going from light to dark regions. Evidence of this is given in the CL maps presented in Figures 7.12(a) and 7.12(b). The reason for the discrepancy between the PL and CL

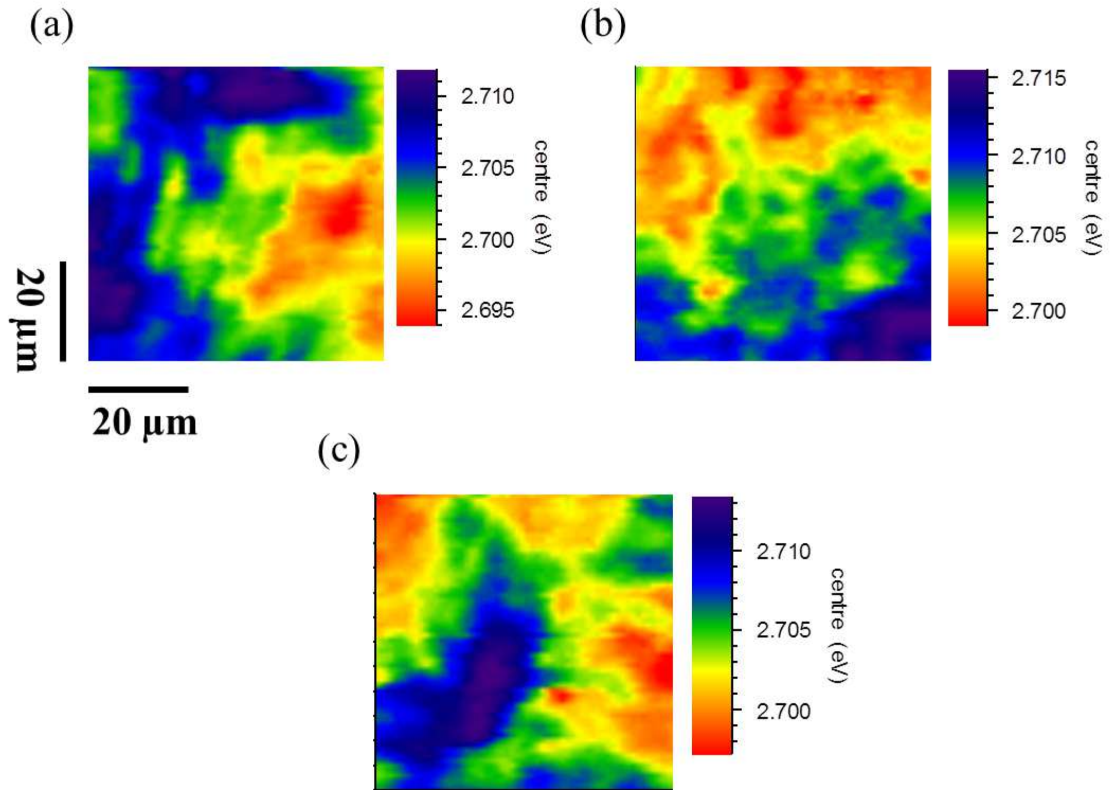

Figure 7.11: Fitted peak energy maps of Q2T sample.

results could be due to differences in excitation regimes. CL has greater excitation intensity than PL and can result in blue-shifting of the emission peak through screening of the QCSE due to increased carrier density [186, 187, 188]. Therefore, these dark spots could be acting as nonradiative carrier trapping regions caused by defect clusters, with the red shifting in the PL attributed to possibly alloy or well width fluctuations within the QWs.

Different areas of the 2T sample were mapped to compare the luminescence properties with the Q2T sample. The RT PL maps were performed under the same conditions as the Q2T sample. Again no response was applied to the maps as it had no influence on the outcome of the results, even when compared to the Q2T sample. The fitted intensity maps from the various regions are presented in Figure 7.13, along with an example spectrum. Unlike the Q2T sample, the RT PL intensity maps from the 2T sample show no dark spot-like features, as also seen in CL in Figure 7.12(c). There are some small variations in the intensity

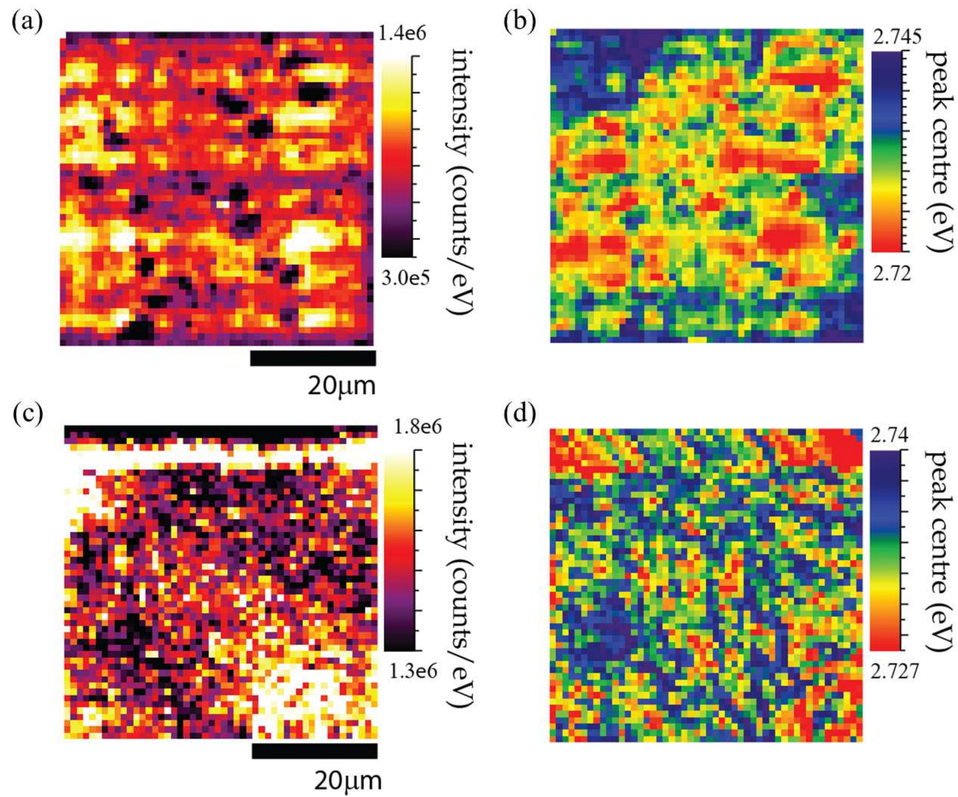

Figure 7.12: CL maps of (a) sample Q2T MQW intensity, (b) sample Q2T MQW peak energy, (c) sample 2T MQW intensity and (d) sample 2T MQW peak energy. *Data and image credit given to Michael Wallace.*

across each of the PL maps but the overall homogeneity has greatly improved when compared to the Q2T sample. Also the mean intensity is higher in the 2T maps compared to Q2T. Both the homogeneity and mean peak intensity of each of the maps are illustrated by comparing their histograms, whereby the peak and spread in intensity values of each map is given. These histograms are shown in Figure 7.14, with the Q2T sample having the lower intensity values and wider histogram pixel spread. This reveals that the Q2T sample is of poorer quality than the 2T even with the exclusion of the dark spots. This could be from an increase in defects in the lower temperature GaN cap which act as non-radiative recombination centres reducing the radiative emission from the QW. It could also be from an increase in InN content due to the capping nature of the GaN in the Q2T growth method whereby indium desorption is suppressed. From XRD

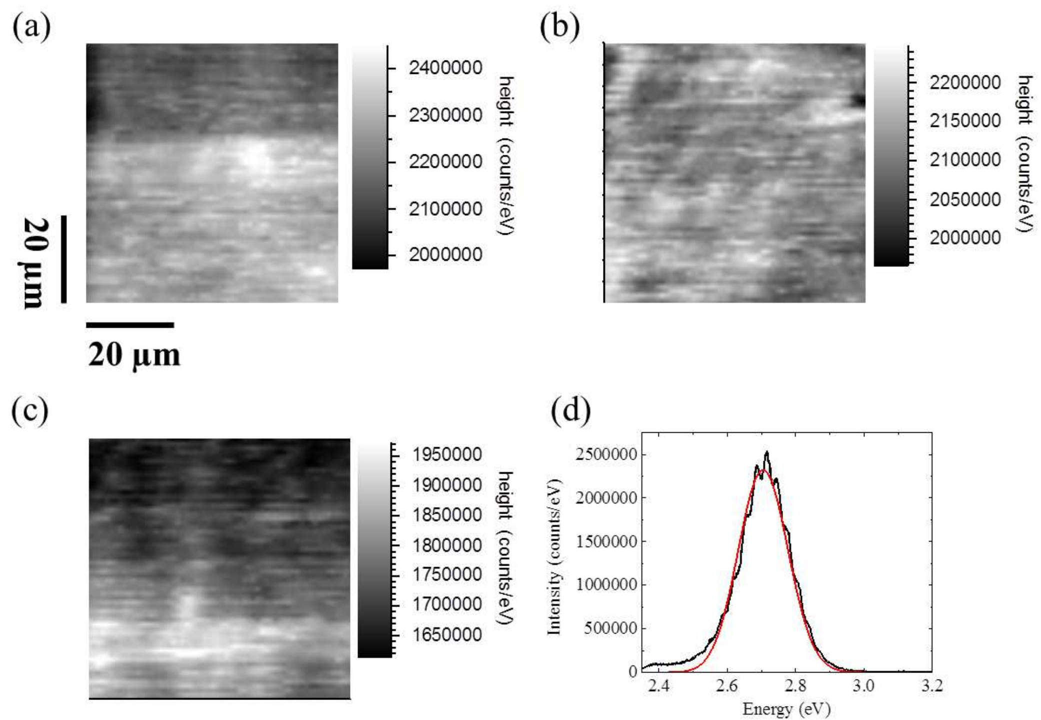

Figure 7.13: (a), (b), (c) Fitted intensity maps of different areas of the 2T sample. (d) Spectrum taken from map (a) showing fitting.

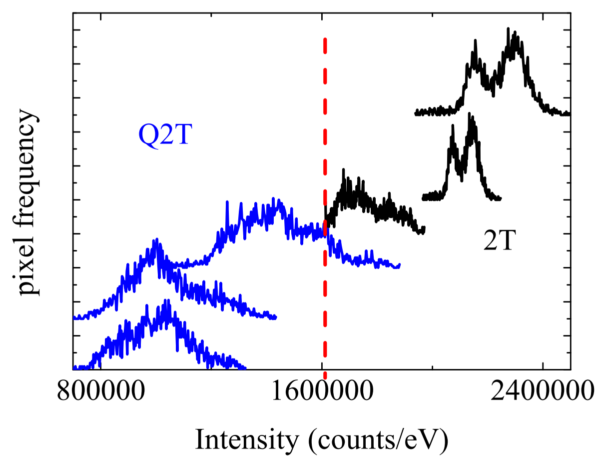

Figure 7.14: Histograms of each of the Q2T and 2T maps. The Q2T maps are presented in blue and 2T in black. Each histogram has been offset for clarity.

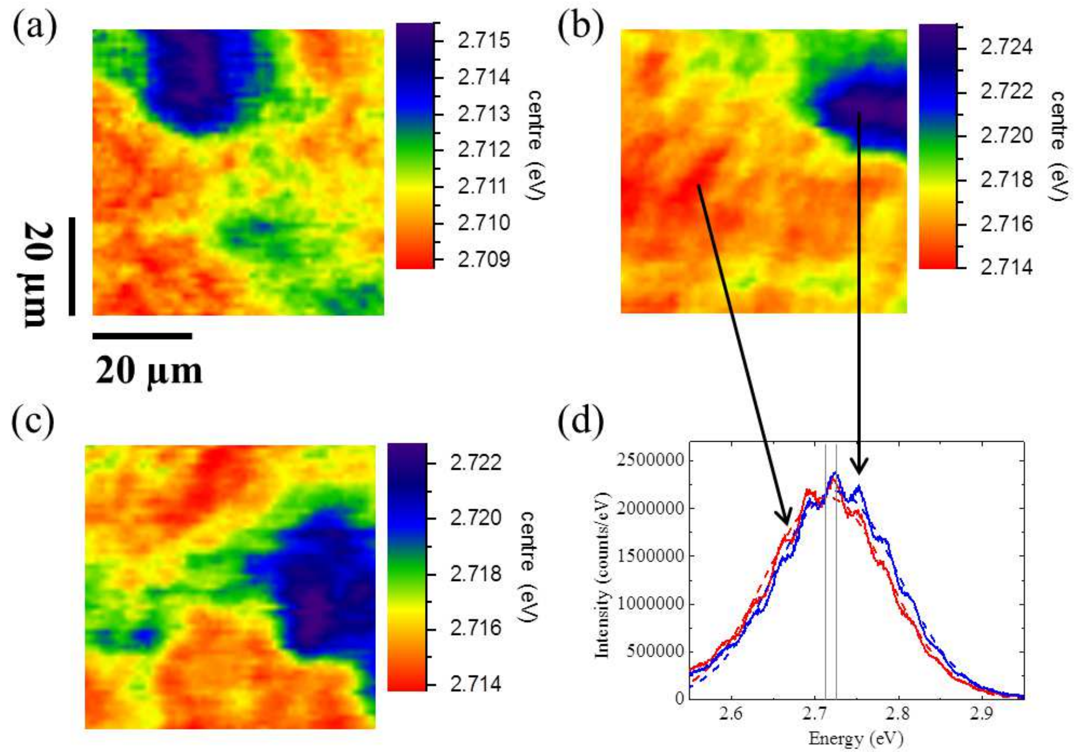

Figure 7.15: (a), (b), (c) Fitted peak energy maps of 2T sample. (d) Spectra taken from red and blue regions of map (b) as indicated by the arrows.

measurements the InN content within the wells is approximately 19 % for the Q2T sample and 17 % for the 2T sample. The increase in InN content in the Q2T sample will reduce the peak emission energy when compared to the 2T sample.

From the fitted peak energy maps of the 2T sample the mean centre energy is 10 meV higher than the Q2T at 2.715 eV, and also has lower peak energy variation across the maps (∼10 meV). This agrees with the XRD measurement that showed there to be less indium in the 2T sample than the Q2T. The energy maps also revealed interesting features which do not correlate with their intensity maps (Figure 7.13), unlike the Q2T sample. The areas of higher peak energy are not the areas of highest intensity. These energy maps are displayed in Figure 7.15, along with example spectra taken from a blue and red region. At first sight these blue regions might be related to the larger filament like features seen by Wallace et al [173] in CL and EL map measurements. However, the CL and EL

results show a clear relationship between intensity and emission energy, and these filament features are from a Q2T type sample not 2T.

These larger areas of shifted intensity could be from fluctuations in well thickness through monolayer variations, which may be induced by surface inhomogeneity in the templates. The narrower regions of the QWs would have higher emission energy [188, 189]. Well width fluctuations would result in variations in carrier localisation which in-turn varies the recombination probability, and therefore the intensity. However, Chichibu et al found that for QWs <3.6 nm there is little or no change in PL intensity while having a red-shift in peak energy [189]. This was reported for point spectra and not mapped areas. The authors attribute this to the thickness of the well being less than the Bohr radius (a_b) resulting in overlapping of the electron and hole wavefunctions below 3.6 nm. The thickness of the QWs for the 2T sample measured from XRD are estimated to be around 1.4 nm due to the 'gappy' nature of the wells (explanation further on). This suggests that the above argument by Chichibu et al is plausible here as the thickness of the wells are <3.6 nm. To confirm whether QW monolayer variations may be the cause for an energy shift with little or no change in intensity a closer look at the shift in energy over each of the maps was pursued. Over the 3 mapped areas the change in energy between the red and blue areas is ∼8–13 meV, with a 10 meV shift highlighted in the spectra in Figure 7.15(d). For one QW monolayer (1 ML = 0.259 nm) variation the change in bandgap energy was calculated by Graham et al to be 58 meV [190]. This is higher than the value returned from the maps suggesting that well thickness fluctuations is probably not the cause. This was calculated for a SQW of thickness 3.3 nm, with an InN content of 25 %, highlighting that a greater energy variation is expected for these thinner wells. From the fitted FWHM maps the areas of highest emission energy have the largest linewidths which supports the varied thickness argument. Also this indicates a positive relationship between energy and FWHM, and no relationship between intensity and FWHM.

Comparing these results to the structural and point PL results by Oliver et al on similar Q2T and 2T samples further conclusions can be made [175]. From transmission electron microscopy (TEM) measurements the Q2T sample is shown to have continuous QWs whereas the QWs in the 2T sample have gross well width fluctuations (GWWFs). The GWWFs result in gaps in the QWs which are then

filled by GaN from the subsequent barrier growth. This results in variations in the QW thickness, with the gaps that have no InGaN therefore having zero thickness as shown by the schematic representation in Figure 7.16. This may be the reason for the large blue shifted features in the PL energy maps. However, these GWWFs are around 50–100 nm whereas the blue regions are ∼20 µm. A possible cause could be collective regions of these InGaN GWWFs at different thickness or InN content than other regions. The overall increased intensity of the 2T maps in comparison to the Q2T, as shown by the histograms in Figure 7.14, could be from increased carrier confinement in the InGaN regions of the 'gappy' wells. Also the threading dislocations preferentially pass through the GaN region, as suggested by Oliver et al, allowing carriers to be trapped in almost defect free areas aiding radiative recombination [175, 191]. The 2T sample having higher mean intensity than the Q2T agrees with the PL (and EL) results by Oliver et al for the excitation power density ($\sim 2.5 \times 10^2$ Wcm^{-2}) used here in the PL mapping. A further agreement is in the FWHMs of each of the samples, where the 2T is ∼20–30 meV larger than the Q2T. Again this is due to the morphology of the 2T QWs where a variation in InN content (and thickness) across each of the 50–100 nm InGaN regions results in broader spectral emission.

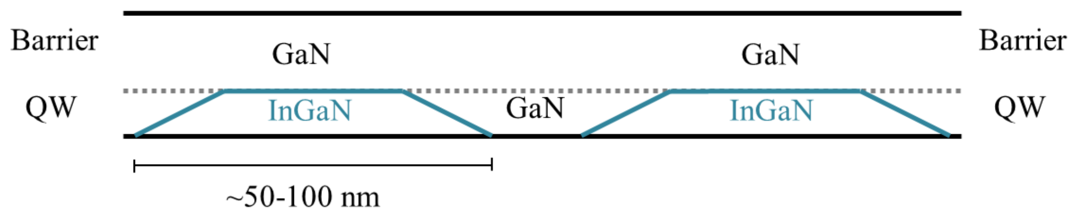

Figure 7.16: A schematic of a 2T QW and barrier showing the morphology of the InGaN QW.

7.5 Summary and Further Developments

A home built PL mapping system has been demonstrated, with details of the design and operation. Initial measurements revealed problems such as directional step size variation, drifting, and movement in and out of the focal plane caused by cryopump vibration at LT. The directional step size variation was corrected for by using the positioners at their maximum range and over stepping on the return direction. This allowed RT maps to be achieved. The LT vibrational issue which resulted in a visible crosshatch effect in the maps was resolved by acquiring spectra at similar frequency to the piston movement. A solution to the drifting problem was not found therefore accurate LT maps could not be achieved.

Utilising this mapping system, investigations of InGaN/GaN MQW LED samples grown under different barrier growth methods were made. The quasi-two-temperature (Q2T) sample revealed dark spot like features in the intensity maps which were comparable to CL measurements performed on similar samples. However, unlike the CL, these spots were not defined within the emission energy maps, and the dark spots were red shifted compared to the brighter regions in the PL whereas they were blue shifted in the CL. These features can be attributed to non-radiative trapping regions created by defects. The PL intensity maps of the two-temperature (2T) sample were found to be more uniform with no dark spot like features, and overall of greater intensity than the Q2T sample. The energy maps did display regions of 10–20 μm in size with higher emission energy which had no relationship with intensity, as no such features were visible in the intensity maps. The idea that these features were related to well thickness fluctuations was examined, and is unlikely to be the cause. This is due to the energy shift being smaller than the predicted value induced by the change in one monolayer.

The next steps in this PL mapping system development would be to solve the LT drifting issue in order to achieve LT maps. Possible solutions could be to adopt a feedback system whereby if the positioners moved further than a desired stepping distance they could be corrected for by counteracting the movement. Another solution, although expensive, would be to change the cooling system to a helium flow cryostat which would remove the source of the problem. On achieving LT mapping, attempts at IQE mapping can be made.

Chapter 8

Summary and Future Work

This chapter collates the main results of the work presented throughout this thesis and provides them as short summaries according to each of the results chapters. Discussions on future work associated with this research are also given.

8.1 Overall Summary

The work presented in this thesis investigates the compositional and optical properties of InGaN and InAlN alloys. The samples studied were; a set of InGaN epilayers grown with varying growth temperatures and hydrogen carrier gas flow rates, InAl(Ga)N epilayers grown on GaN buffers with Ga auto-incorporation, InAlN epilayers grown on AlN buffers, and InGaN/GaN LED structure samples grown under different barrier to well growth temperature methods (2T and Q2T). These last set of samples were used for the implementation of a PL mapping technique. The main techniques used for the study of these samples, including those from collaborators were WDX, RBS, XRD, CL, and PL. Other complimentary techniques used were SE imaging and AFM.

Chapters 1-3 provided background information on III-nitride based LEDs and the properties associated with the III-nitride material system, along with information on the growth and characterisation techniques encountered throughout this thesis. Chapters 4-7 presented the results and analyses of each of the samples under study, with chapter 7 giving a detailed description of setting up a PL mapping system.

Chapter 4 investigates the composition and luminescence properties of a set of 160 nm thick InGaN epilayers grown with varying growth temperatures (680–750°) and hydrogen flow rates (0–200 sccm). Composition measurements from 3 different techniques (WDX, XRD and RBS) are in close agreement across the samples with the lower InN content, with the difference margin increasing with increasing InN content. Further analysis on selected samples revealed the presence of gradients of InN through the layers. The samples grown with small amounts of hydrogen added to the nitrogen carrier gas were seen to improve in surface quality and compositional homogeneity in comparison to samples grown at the same temperature but with no hydrogen introduced. The addition of hydrogen also reduced the InN fraction. This could be compensated by lowering the InGaN growth temperature. CL measurements were also performed on these samples to study the influence of the added hydrogen flow to the optical properties. The peak energy increased and FWHM decreased with increasing hydrogen flow compared to samples grown at the same temperature which implies a reduction in defects within the InGaN layer. The added hydrogen flow had a positive effect on the luminescence homogeneity with the CL maps of the higher quality samples showing a reduction in peak energy variation across the mapped area. By quantifying the peak emission energy variations it was shown that InGaN epilayer samples with an average InN fraction of 10–15 % and grown with a small hydrogen carrier gas flow have a reduced spatial inhomogeneity of the emission energy compared to equivalent samples grown without hydrogen.

Chapter 5 investigates the compositional, optical and structural properties of a set of ∼80nm thick InAlGaN epilayers with Ga auto-incorporation. Various techniques were used to confirm the presence of Ga within the top layers. SE imaging, AFM and minimum yield measurements (achieved by RBS channelling) revealed that sample B was of poor quality with large surface roughness and a strong In and Ga gradient through the layer, unlike sample A which was grown with identical parameters. The CL results of sample B confirmed this poor quality with a weak, broad luminescence which may be associated with AlN defect. The composition results from WDX and RBS measurements returned GaN contents ranging between 12–28 % within the top layer. The values from all techniques, including XRD are in agreement. The growth parameters and resultant Ga incorporation indicate the likely cause being residual Ga coming from the reactor walls

and delivery pipes. Increasing the total flow rate from 8000 sccm to 24000 sccm was seen to suppress the GaN incorporation from 28 to 12 %. This was deemed a more viable method for reducing Ga incorporation than reactor cleaning between growth of the GaN buffer and InAlN layer. Another potential solution investigated was to introduce TMIn flow during buffer growth. Initial findings on using AlGaN buffers revealed approximately 2.5 orders of magnitude reduction in Ga in the InAlN layer without TMIn, and a further reduction with TMIn. Further investigations into which is the dominant suppressor between TMIn and TMAl is required. CL measurements revealed a broad InAlGaN peak whose energy varied with InN composition. The increase in InN resulted in a decrease in emission energy, but the change in GaN content caused no such variation in peak energy, which is positive for making UV LEDs that may inadvertently contain Ga. This broad quaternary luminescence peak was found to be fairly uniform when mapped over a small area.

Chapter 6 investigates the composition and optical properties of a large set of ∼80–150 nm thick InAlN epilayers grown on AlN buffers. Surface and structural properties were also presented for selected samples. The SE images revealed variations in sample quality, with the samples grown at higher temperatures having smoother surfaces. The XRD RSM measurements found the samples grown T>800°C to be fully strained to the underlying AlN and those grown T<800°C to be fully relaxed. The InN content was varied by decreasing the growth temperature. WDX and XRD measurements revealed a wide range of InN contents from 0.1% to 25.6%, with a high agreement between the techniques over the whole composition range. The WDX compositional analysis revealed no presence of Ga within the samples after reactor cleaning and growth of the InAlN on AlN buffers. CL measurements produced broad InAlN luminescence spectra which varied with InN content. The peak energy was found to be 3.46–3.93 eV for InN compositions of 0.7–6.6 %. Further analysis suggests this is not bandedge emission due to the low peak energy and very wide FWHMs when compared to predicted and measured values. The luminescence could be due to high alloy fluctuations within the poor quality material although this is questionable for the low InN (0.22 %) containing samples.

Chapter 7 demonstrated a home built PL mapping system, with details of the design and operation. Initial measurements revealed problems such as directional

step size variation, drifting, and movement in and out of the focal plane caused by cryopump vibration at LT. The directional step size variation was corrected for by using the positioners at their maximum range and over stepping on the return direction. This allowed RT maps to be achieved. The LT vibrational issue which resulted in a visible crosshatch effect in the maps was resolved by acquiring spectra at similar frequency to the piston movement. A solution to the drifting problem was not found and therefore accurate LT maps could not be achieved. However utilising this mapping system, investigations of InGaN/GaN MQW LED samples grown under different barrier growth methods could be made. The quasi-two-temperature (Q2T) sample revealed dark spot like features in the intensity maps which were comparable to CL measurements performed on similar samples. However, unlike the CL, these spots were not defined within the emission energy maps, and the dark spots were red shifted compared to the brighter regions in the PL whereas they were blue shifted in the CL. These features can be attributed to non-radiative trapping regions created by defects. The PL intensity maps of the two-temperature (2T) sample were found to be more uniform with no dark spot like features, and to have greater overall intensity than the Q2T sample. The energy maps did display regions of 10–20 μm in size with higher emission energy which had no relationship with intensity, as no such features were visible in the intensity maps. The idea that these features were related to QW thickness fluctuations was examined and is unlikely to be the cause.

8.2 Future Work

With regards to InGaN alloy the research into increasing the optical efficiencies of the material at longer wavelengths and understanding the ‘green gap’ issue is ongoing. This work looked at the effects of sample quality, composition and luminescence on InGaN epilayers when including small amounts of hydrogen to the nitrogen carrier gas during growth. The hydrogen flow was limited to 200 sccm and the growth temperature to 680°C so a possible future study could be to push these parameters further to see if longer wavelength emissions can be achieved, and to investigate if there is an optimum hydrogen flow rate. Also looking at these effects in QW structures is another possible study, with the aim to make full LEDs for testing.

For the Ga auto-incorporated InAlN layers the main focus is to fully understand where the Ga is coming from, how it is incorporated and how it can be reduced or eradicated. Initial work on suppressing the Ga by growing the buffer with small TMIn flow has seen a reduction in Ga, but as the buffer was AlGaN the TMAl is suggested to have similar effects. Therefore further study of TMIn flow during GaN buffer would clear this ambiguity. Also more optical studies would confirm if the luminescence is dominated by the InN content and not the GaN.

For the InAlN layers grown on AlN buffers possible further studies include developing these layers into QW structures with collaborators and characterising their properties. Hopefully with increased carrier confinement higher emission intensities will be achieved and investigations on the spatial variation of the luminescence may be possible. This would provide a deeper insight into the origins of the luminescence and give further information on the relationship of bandgap with InN content for low InN compositions. This would hopefully lead to the development of high energy UV LEDs.

The next steps in the PL mapping system development would be to solve the LT drifting issue in order to achieve LT maps. Possible solutions could be to adopt a feedback system whereby if the positioners moved further than a desired stepping distance they could be corrected for by counteracting the movement. Another solution, although expensive, would be to change the cooling system to a helium flow cryostat which would remove the source of the problem. On achieving LT mapping, attempts at IQE mapping can be made. This would involve mapping the same area at both RT and LT and taking the difference between the maps to get a rough idea of the spatial IQE. Also taking maps at temperature intervals would allow the evolution of spatial efficiency with temperature to be studied, and the possibility to link this to areas of high and low defect densities.

References

[1] "Nobel Prize in Physics 2014". http://www.nobelprize.org/nobel_prizes/physics/laureates/2014/ (url date: 18/11/2014).

[2] International Energy Agency. *Light's labour's lost: Policies for energy-efficient lighting.* 2006.

[3] Humphreys C J. Solid-state lighting. *MRS Bull.*, 33:459–470, 4 2008.

[4] European Commission MEMO/09/368. Phasing out conventional incandescent bulbs. http://europa.eu/rapid/press-release_MEMO-09-368_en.htm, September 2009.

[5] Kim J K and Schubert E F. Transcending the replacement paradigm of solid-state lighting. *Opt. Express*, 16(26):21835–21842, Dec 2008.

[6] Jones B F. The calculation of the luminous efficacy of a semiconductor lamp. *J. Phys. D: Appl. Phys.*, 6(7):L80, 1973.

[7] Taylor E, Edwards P R and Martin R W. Colorimetry and efficiency of white LEDs: Spectral width dependence. *Phys. Stat. Sol. A*, 209(3):461–464, 2012.

[8] Davis W and Ohno Y. Approaches to color rendering measurement. *J. Mod. Optic*, 56(13):1412–1419, 2009.

[9] Žukauskas A, Vaicekauskas R, Ivanauskas F, Gaska R and Shur M S. Optimization of white polychromatic semiconductor lamps. *Appl. Phys. Lett.*, 80(2):234–236, 2002.

[10] Ohno Y. Color rendering and luminous efficacy of white LED spectra. *Proc. SPIE*, 5530:88–98, 2004.

[11] Muramoto Y, Kimura M and Nouda S. Development and future of ultraviolet light-emitting diodes: UV-LED will replace the UV lamp. *Semicond. Sci. Technol.*, 29(8):084004, 2014.

[12] Schubert E F. *Light Emitting Diodes*. Cambridge University Press, second edition, 2006.

[13] Zheludev N. The life and times of the LED a 100-year history. *Nature Photon.*, 1, 2007.

[14] Round H J. A note on carborundum. *Electr. World*, 49:309, 1907.

[15] Lossev O V. Luminous carborundum detector and detection effect and oscillations with crystals. *Philos. Mag.*, 6(39):1024–1044, 1928.

[16] Holonyak N and Bevacqua S F. Coherent (visible) light emission from $Ga(As_{1-x}P_x)$ junctions. *Appl. Phys. Lett.*, 1(4):82–83, 1962.

[17] Dupuis R D and Krames MR. History, Development, and Applications of High-Brightness Visible Light-Emitting Diodes. *J. Lightwave Technol.*, 26(9):1154–1171, May 2008.

[18] Maruska H P and Tietjen J J. The preparation and properties of vapordeposited single crystalline GaN. *Appl. Phys. Lett.*, 15(10):327–329, 1969.

[19] Maruska H P, Stevenson D A and Pankove J I. Violet luminescence of Mg-doped GaN. *Appl. Phys. Lett.*, 22(6):303–305, 1973.

[20] Nakamura S and Fasol G. *The Blue Laser Diode: GaN Based Light Emitters and Lasers*. Springer, 1997.

[21] Nakamura S, Harada Y and Seno M. Novel metalorganic chemical vapor deposition system for GaN growth. *Appl. Phys. Lett.*, 58(18):2021–2023, 1991.

[22] Akasaki I. Key inventions in the history of nitride-based blue LED and LD. *J. Cryst. Growth*, 300(1):2–10, 2007. First International Symposium on Growth of Nitrides ISGN-1.

[23] Amano H, Asahi T and Akasaki I. Stimulated emission near ultraviolet at room temperature from a GaN film grown on sapphire by MOVPE using an AlN buffer layer. *Jpn. J. Appl. Phys.*, 29(2A):L205, 1990.

[24] Nakamura S. GaN growth using GaN buffer layer. *Jpn. J. Appl. Phys.*, 30(10A):L1705, 1991.

[25] Amano H, Kito M, Hiramatsu K and Akasaki I. P-type conduction in Mg-doped GaN treated with low-energy electron beam irradiation (LEEBI). *Jpn. J. Appl. Phys.*, 28(12A):L2112, 1989.

[26] Akasaki I and Amano H. Breakthroughs in improving crystal quality of GaN and invention of the p-n junction blue-light-emitting diode. *Jpn. J. Appl. Phys.*, 45(12R):9001, 2006.

[27] Nakamura S, Mukai T, Senoh M and Iwasa N. Thermal annealing effects on p-type Mg-doped GaN films. *Jpn. J. Appl. Phys.*, 31(2B):L139, 1992.

[28] Nakamura S, Iwasa N, Senoh M and Mukai T. Hole compensation mechanism of p-type GaN films. *Jpn. J. Appl. Phys.*, 31(5R):1258, 1992.

[29] Nakamura S, Senoh M and Mukai T. P-GaN/N-InGaN/N-GaN double-heterostructure blue-light-emitting diodes. *Jpn. J. Appl. Phys.*, 32(1A):L8, 1993.

[30] Nakamura S, Senoh M, Iwasa N, and Nagahama S. High-brightness InGaN blue, green and yellow light-emitting diodes with quantum well structures. *Jpn. J. Appl. Phys.*, 34(7A):L797, 1995.

[31] DenBaars S P, Feezell D, Kelchner K, Pimputkar S, Pan C-C, Yen C-C, Tanaka S, Zhao Y, Pfaff N, Farrell R, Iza M, Keller S, Mishra U, Speck J S and Nakamura S. Development of gallium-nitride-based light-emitting diodes (LEDs) and laser diodes for energy-efficient lighting and displays. *Acta Mater.*, 61(3):945–951, 2013.

[32] Khan M A, Shatalov M, Maruska H P, Wang H M and Kuokstis E. III-Nitride UV devices. *Jpn. J. Appl. Phys.*, 44(10R):7191, 2005.

[33] Han J, Crawford M H, Shul R J, Figiel J J, Banas M, Zhang L, Song Y K, Zhou H and Nurmikko A V. AlGaN/GaN quantum well ultraviolet light emitting diodes. *Appl. Phys. Lett.*, 73(12):1688–1690, 1998.

[34] Kneissl M, Kolbe T, Chua C, Kueller v, Lobo N, Stellmach J, Knauer A, Rodriguez H, Einfeldt S, Yang Z, Johnson N M and Weyers M. Advances in group III-nitride-based deep UV light-emitting diode technology. *Semicond. Sci. Technol.*, 26(1):014036, 2011.

[35] Lorenz K, Franco N, Alves E, Watson I M, Martin R W and O'Donnell K P. Anomalous ion channeling in AlInN/GaN bilayers: Determination of the strain state. *Phys. Rev. Lett.*, 97:085501, 2006.

[36] Wei Q Y, Li T, Huang Y, Huang J Y, Chen Z T, Egawa T and Ponce F A. Compositional instability in InAlN/GaN lattice-matched epitaxy. *Appl. Phys. Lett.*, 100(9), 2012.

[37] Dorsaz J, Carlin J-F, Gradecak S and Ilegems M. Progress in AlInN-GaN Bragg reflectors: Application to a microcavity light emitting diode. *J. Appl. Phys.*, 97(8), 2005.

[38] Watson I M, Liu C, Gu E, Dawson M D, Edwards P R, and Martin R W. Use of AlInN layers in optical monitoring of growth of GaN-based structures on free-standing GaN substrates. *Appl. Phys. Lett.*, 87(15):151901, 2005.

[39] Ichimura I, Maeda F, Osato K, Yamamoto K and Kasami Y. Optical disk recording using a GaN blue-violet laser diode. *Jpn. J. Appl. Phys.*, 39(2S):937, 2000.

[40] Maier D, Alomari M, Grandjean N, Carlin J, Diforte-Poisson M, Dua C, Delage S and Kohn E. InAlN/GaN HEMTs for operation in the 1000°C regime: A first experiment. *Electron Devic Lett., IEEE*, 33(7):985–987, July 2012.

[41] Mishra U K, Parikh P and Wu Y-F. AlGaN/GaN HEMTs - an overview of device operation and applications. *Proceedings of the IEEE*, 90(6):1022–1031, Jun 2002.

[42] Neufeld C J,Toledo N G, Cruz S C, Iza M, DenBaars S P and Mishra U K. High quantum efficiency InGaN/GaN solar cells with 2.95 eV band gap. *Appl. Phys. Lett.*, 93(14), 2008.

[43] Senda S, Jiang H and Egawa T. AlInN-based ultraviolet photodiode grown by metal organic chemical vapor deposition. *Appl. Phys. Lett.*, 92(20), 2008.

[44] Vilhunen S, Sarkka H and Sillanpaa M. Ultraviolet light-emitting diodes in water disinfection. *Environ. Sci. Pollut. Res.*, 16(4):439–442, 06 2009.

[45] Butté R, Carlin J-F, Feltin E, Gonschorek M, Nicolas S, Christmann G, Simeonov D, Castiglia A, Dorsaz J, Buehlmann H J, Christopoulos S, Baldassarri Höger von Högersthal G, Grundy A J D, Mosca M, Pinquier C, Py M A, Demangeot F, Frandon J, Lagoudakis P G, Baumberg J J and Grandjean, N. Current status of AlInN layers lattice-matched to GaN for photonics and electronics. *J. Phys. D: Appl. Phys.*, 40:6328–6344, 2007.

[46] Wu J. When group-III nitrides go infrared: New properties and perspectives. *J. Appl. Phys.*, 106(1), 2009.

[47] Chun H, and Manousiadis P, Rajbhandari S, Vithanage D A, Faulkner G, Tsonev D, McKendry J J D, Videv S, Xie E, Gu E, Dawson M D, Haas H, Turnbull G A, Samuel I D W and O'Brien D C. Visible light communication using a blue GaN μLED and fluorescent polymer color converter. *Photon. Technol. Lett., IEEE*, 26(20):2035–2038, Oct 2014.

[48] Gil B, editor. *Group III-nitride semiconductor compounds*. Oxford University Press, 1998.

[49] Nakamura S and Chichibu S F, editors. *Introduction to Nitride Semiconductor Blue Lasers and Light Emitting Diodes*. Taylor & Francis, 2000.

[50] Monemar B. III-V nitrides – important future electronic materials. *J. Mater. Sci.–Mater. El.*, 10(4):227–254, 1999.

[51] Bhuiyan A G, Hashimoto A and Yamamoto A. Indium nitride (InN): A review on growth, characterization, and properties. *J. Appl. Phys.*, 94(5):2779–2808, 2003.

[52] Denton A R and Ashcroft N W. Vegard's law. *Phys. Rev. A*, 43:3161–3164, Mar 1991.

[53] Vegard L. *Z. Phys.*, 5(1):17–26, 1921.

[54] Jiang H X and Lin J Y. AlGaN and InAlGaN alloys - epitaxial growth, optical and electrical properties, and applications. *Opto-Electron. Rev*, 10(4):271–286, 2012.

[55] McIntosh F G, Boutros K S, Roberts J C, Bedair S M, Piner E L and El-Masry N A. Growth and characterization of AlInGaN quaternary alloys. *Appl. Phys. Lett.*, 68(1):40–42, 1996.

[56] Darakchieva V, Beckers M, Xie M-Y, Hultman L, Monemar B, Carlin J-F, Feltin E, Gonschorek M and Grandjean N. Effects of strain and composition on the lattice parameters and applicability of Vegard's rule in Al-rich $Al_{1-x}In_xN$ films grown on sapphire. *J. Appl. Phys.*, 103(10), 2008.

[57] Ambacher O. Growth and applications of group III–nitrides. *J. Phys. D: Appl. Phys.*, 31(20):2653, 1998.

[58] Gil B, editor. *Low-Dimensional Nitride Semiconductors.* Oxford University Press, 2002.

[59] Bernardini F, Fiorentini V and Vanderbilt D. Spontaneous polarization and piezoelectric constants of III-V nitrides. *Phys. Rev. B*, 56:R10024–R10027, 1997.

[60] Schulz S, Caro M A, Tan L T, Parbrook P J, Martin R W and O'Reilly E P. Composition-dependent band gap and band-edge bowing in AlInN: A combined theoretical and experimental study. *Appl. Phys. Express*, 6(12):121001, 2013.

[61] Wu J and Walukiewicz W. Band gaps of InN and group III nitride alloys. *Superlattice Microstr.*, 34:63–75, 2003.

[62] Matsuoka T, Okamoto H, Nakao M, Harima H, and Kurimoto E. Optical bandgap energy of wurtzite InN. *Appl. Phys. Lett.*, 81(7):1246–1248, 2002.

[63] Gorczyca I, Suski T, Christensen N E and Svane A. Band gap bowing in quaternary nitride semiconducting alloys. *Appl. Phys. Lett.*, 98(24), 2011.

[64] O'Donnell K P, Auf der Maur M, Di Carlo A, Lorenz K and the SORBET consortium. It's not easy being green: Strategies for all-nitrides, all-colour solid state lighting. *Phys. Stat. Sol. RRL*, 6(2):49–52, 2012.

[65] Krames M R, Shchekin O B, Mueller-Mach R, Mueller G O, Zhou L, Harbers G and Craford M G. Status and future of high-power light-emitting diodes for solid-state lighting. *J. Disp. Technol.*, 3(2):160–175, 2007.

[66] Crawford M H. LEDs for solid-state lighting: Performance challenges and recent advances. *IEEE J. Sel. Top. Quantum Electron.*, 15(4):1028–1040, 2009.

[67] Kim K S, Saxler A, Kung P, Razeghi M and Lim K Y. Determination of the band-gap energy of $Al_{1-x}In_xN$ grown by metalorganic chemical-vapor deposition. *Appl. Phys. Lett.*, 71(6):800–802, 1997.

[68] Yamaguchi S, Kariya M,Nitta S, Kato H, Takeuchi T, Wetzel C, Amano H and Akasaki I. Structural and optical properties of AlInN and AlGaInN on GaN grown by metalorganic vapor phase epitaxy. *J. Cryst. Growth*, 195:309–313, 1998.

[69] Morkoç H. *Nitride Semiconductors and Devices*. Springer, 1999.

[70] Martin R W, Middleton P G, O'Donnell K P and Van der Stricht W. Exciton localization and the Stokes' shift in InGaN epilayers. *Appl. Phys. Lett.*, 74(2):263–265, 1999.

[71] El-Masry N A, Piner E L, Liu S X and Bedair S M. Phase separation in InGaN grown by metalorganic chemical vapor deposition. *Appl. Phys. Lett.*, 72(1):40–42, 1998.

[72] Chichibu S, Sota T, Wada K and Nakamura S. Exciton localization in InGaN quantum well devices. *J. Vac. Sci. Technol. B*, 16(4):2204–2214, 1998.

[73] Watson I M. Metal organic vapour phase epitaxy of AlN, GaN, InN and their alloys: A key chemical technology for advanced device applications. *Coordin. Chem. Rev.*, 257:2120–2141, 2013.

[74] Jain S C, Willander M, Narayan J and Van Overstraeten R. III-nitrides: Growth, characterization, and properties. *J. Appl. Phys.*, 87(3):965–1006, 2000.

[75] Keller S and DenBaars S P. Metalorganic chemical vapor deposition of group III nitrides– a discussion of critical issues. *J. Cryst. Growth*, 248(0):479–486, 2003.

[76] Taylor E, Fang F, Oehler F, Edwards P R, Kappers M J, Lorenz K, Alves E, McAleese C, Humphreys C J and Martin R W. Composition and luminescence studies of InGaN epilayers grown at different hydrogen flow rates. *Semicond. Sci. Technol.*, 28(6):065011, 2013.

[77] Gil B, editor. *III-nitride semiconductors and their modern devices.* Oxford University Press, 2014.

[78] Takeuchi T, Wetzel C, Yamaguchi S, Sakai H, Amano H, Akasaki I, Kaneko Y, Nakagawa S, Yamaoka Y and Yamada N. Determination of piezoelectric fields in strained GaInN quantum wells using the quantum-confined Stark effect. *Appl. Phys. Lett.*, 73(12):1691–1693, 1998.

[79] Shaw M, Yu K M, Ting M, Powell R E L, Sarney W L, Svensson S P, Kent A J, Walukiewicz W, Foxon C T, Novikov S V and Martin R W. Composition and optical properties of dilute-Sb $GaN_{1-x}Sb_x$ highly mismatched alloys grown by MBE. *J. Phys. D: Appl. Phys.*, 47:465102, 2014.

[80] Novikov S V, Yu K M, Levander A, Detert D, Sarney W L, Liliental-Weber Z, Shaw M, Martin R W, Svensson S P, Walukiewicz W and Foxon C T. Molecular beam epitaxy of highly mismatched N-rich $GaN_{1-x}b_x$ and $InN_{1-x}As_x$ alloys. *J. Vac. Sci. Technol. B*, 31(3):03C102, 2013.

[81] Joyce B A and Joyce T B. Basic studies of molecular beam epitaxy - past, present and some future directions. *J. Cryst. Growth*, 264(4):605–619, 2004.

[82] Okumura H, Ohta K, Feuillet G, Balakrishnan K, Chichibu S, Hamaguchi H, Hacke P and Yoshida S. Growth and characterization of cubic GaN. *J. Cryst. Growth*, 178:113–133, 1997.

[83] Henini M. Molecular beam epitaxy from research to mass-production - Part 1. *III-Vs Rev.*, 9(3):32–34, 1996.

[84] Foxon C T. Three decades of molecular beam epitaxy. *J. Cryst. Growth*, 251:1–8, 2003.

[85] Behet M, Hövel R, Kohl A, Mesquida Küsters A, Opitz B and Heime K. MOVPE growth of III-V compounds for optoelectronic and electronic applications. *Microelectr. J.*, 27:297–334, 1996.

[86] Creighton J R, Wang G T and Coltrin M E. Fundamental chemistry and modeling of group-III nitride MOVPE. *J. Cryst. Growth*, 298(0):2–7, 2007.

[87] Egerton R F. *Physical Principles of Electron Microscopy - An Introduction to TEM, SEM, and AEM.* Springer, 2005.

[88] FEI Company. The Quanta FEG 250/450/650 user operation manual - 5th edition, August 2011.

[89] Reed S J B. *Electron Microprobe Analysis and Scanning Electron Microscopy in Geology.* Cambridge University Press, 2005.

[90] Goldstein J I, Newbury D E, Echlin P, Joy D C,Romig Jr. A D, Lyman C E, Fiori C and Lifshin E. *Scanning Electron Microscopy and X-Ray Microanalysis.* Plenum Press, second edition, 1992.

[91] Yacobi B G and Holt D B. *Cathodoluminescence Microscopy of Inorgainc Solids.* Plenum Press, 1990.

[92] H Seiler. Secondary electron emission in the scanning electron microscope. *J. Appl. Phys.*, 54(11):R1–R18, 1983.

[93] Everhart T E and Thornley R F M. Wide-band detector for micro-microampere low-energy electron currents. *J. Sci. Instrum.*, 37(7):246, 1960.

[94] Drouin D, Couture A, Joly D, Tastet X, Aimez V, and Gauvin R. CASINO V2.42A fast and easy-to-use modeling tool for scanning electron microscopy and microanalysis users. *Scanning*, 29(3):92–101, 2007.

[95] Kanaya K and Okayama S. Penetration and energy-loss theory of electrons in solid targets. *J. Phys. D: Appl. Phys.*, 5(1):43, 1972.

[96] Deatcher C J, Bejtka K, Martin R W, Romani S, Kheyrandish H, Smith L M, Rushworth S A, Liu C, Cheong M G and Watson I M. Wavelength-dispersive x-ray microanalysis as a novel method for studying magnesium doping in gallium nitride epitaxial films. *Semicond. Sci. Technol.*, 21(9):1287, 2006.

[97] Mackenzie A P. Recent progress in electron probe microanalysis. *Rep. Prog. Phys.*, 56(4):557, 1993.

[98] Reed S J B. Optimization of wavelength dispersive x-ray spectrometry analysis conditions. *J. Res. Natl. Inst. Stand. Technol.*, 107:497–502, 2002.

[99] Merlet C. An accurate computer correction program for quantitative electron probe microanalysis. *Mikrochimica Acta*, 114-115(1):363–376, 1994.

[100] Amabile D, Martin R W, Wang T, Whitehead M A, and Parbrook P J. Compositional analysis of AlInGaN quaternary layers grown by metalorganic vapour phase epitaxy. *Phys. Stat. Sol. C*, 0(7):2478–2481, 2003.

[101] Chu W-K. *Backscattering spectrometry.* Academic Press, Inc., 1978.

[102] Barradas N P, Arstila K, Battistig G, Bianconi M, Dytlewski N, Jeynes C, Kótai E, Lulli G, Mayer M, Rauhala E, Szilágyi E and Thompson M. International Atomic Energy Agency intercomparison of ion beam analysis software. *Nucl. Instrum. Meth. B*, 262(2):281–303, 2007.

[103] Jeynes C, Barradas N P, Marriott P K, Boudreault G, Jenkin M, Wendler E and Webb R P. Elemental thin film depth profiles by ion beam analysis

using simulated annealing - a new tool. *J. Phys. D: Appl. Phys.*, 36(7):R97, 2003.

[104] Barradas N P and Jeynes C. Advanced physics and algorithms in the IBA datafurnace. *Nucl. Instrum. Meth. B*, 266(8):1875–1879, 2008.

[105] Fewster P F. X-ray diffraction from low-dimensional structures. *Semicond. Sci. Technol.*, 8(11):1915, 1993.

[106] Moram M A and Vickers M E. X-ray diffraction of III-nitrides. *Rep. Prog. Phys.*, 72(3):036502, 2009.

[107] Binnig G, Quate C F and Gerber Ch. Atomic force microscope. *Phys. Rev. Lett.*, 56:930–933, 1986.

[108] Everhart T E and Hoff P H. Determination of kilovolt electron energy dissipation vs penetration distance in solid materials. *J. Appl. Phys.*, 42(13):5837–5846, 1971.

[109] Edwards P R, Jagadamma L K, Bruckbauer J, Liu C, Shields P, Allsopp D, Wang T and Martin R W. High-resolution cathodoluminescence hyperspectral imaging of nitride nanostructures. *Microsc. Microanal*, 18:1212–1219, 12 2012.

[110] Bruckbauer J, Edwards P R, Bai J, Wang T and Martin R W. Probing light emission from quantum wells within a single nanorod. *Nanotechnology*, 24(36):365704, 2013.

[111] Edwards P R and Martin R W. Cathodoluminescence nano-characterization of semiconductors. *Semicond. Sci. Technol.*, 26:064005, 2011.

[112] Martin R W, Edwards P R, O'Donnell K P, Mackay E G and Watson I M. Microcomposition and luminescence of InGaN emitters. *Phys. Stat. Sol. A*, 192(1):117–123, 2002.

[113] Neamen D A. *Semiconductor Physics and Devices*. McGraw-Hill, third edition, 2003.

[114] Muth J F, Lee J H, Shmagin I K, Kolbas R M, Casey H C, Keller B P, Mishra U K and DenBaars S P. Absorption coefficient, energy gap, exciton binding energy, and recombination lifetime of GaN obtained from transmission measurements. *Appl. Phys. Lett.*, 71(18):2572–2574, 1997.

[115] Chang P C, Yu C L, Jahn Y W, Chang S J and Lee K H. Effect of growth temperature on the indium incorporation in InGaN epitaxial films. *Adv. Mat. Res.*, 287:1456–1459, 2011.

[116] Tamulaitis G. Spatial inhomogeneity of luminescence in III-nitride compounds. *Mater. Sci.*, 17(4):343–351, 2011.

[117] Sadler T C, Kappers M J and Oliver R A. The impact of hydrogen on indium incorporation and surface accumulation in InAlN epitaxy. *J. Cryst. Growth*, 331:4–7, 2011.

[118] Bosi M and Fornari R. A study of indium incorporation efficiency in InGaN grown by MOVPE. *J. Cryst. Growth*, 265:434–439, 2004.

[119] Piner E L, Behbehani M K, El-Masry N A, McIntosh F G, Roberts J C, Boutros K S, and Bedair S M. Effect of hydrogen on the indium incorporation in InGaN epitaxial films. *Appl. Phys. Lett.*, 70:461–463, 1997.

[120] Bosi M, Fornari R, Scardova S, Avella M, Martínez O and Jimenez J. Compositional and optical uniformity of InGaN layers deposited on (0001) sapphire by metalorganic vapour phase epitaxy. *Semicond. Sci. Technol.*, 19:147–151, 2004.

[121] Martin R W, Edwards P R, O'Donnell K P, Dawson M D, Jeon C-W, Liu C, Rice G R and Watson I M. Cathodoluminescence spectral mapping of III-nitride structures. *Phys. Stat. Sol. A*, 201(4):665–672, 2004.

[122] Kappers M J, Datta R, Oliver R A, Rayment F D G, Vickers M E and Humphreys C J. Threading dislocation reduction in (0001) GaN thin films using SiN_x interlayers. *J. Cryst. Growth*, 300:70–74, 2007.

[123] Oliver R A, Kappers M J, Sumner J, Datta R and Humphreys C J. Highlighting threading dislocations in MOVPE-grown GaN using an in situ treatment with SiH_4 and NH_3. *J. Cryst. Growth*, 289(2):506–514, 2006.

[124] Barradas N P, Jeynes C and Webb R P. Simulated annealing analysis of Rutherford backscattering data. *Appl. Phys. Lett.*, 71(2):291–293, 1997.

[125] Horcas I, Fernández R, Gómez-Rodríguez J M, Colchero J, Gómez-Herrero J and Baro A M. Wsxm: A software for scanning probe microscopy and a tool for nanotechnology. *Rev. Sci. Instrum.*, 78(1):013705, 2007.

[126] Massabuau F C-P, Sahonta S-L, Trinh-Xuan L, Rhode S, Puchtler T J, Kappers M J, Humphreys C J and Oliver R A. Morphological, structural, and emission characterization of trench defects in InGaN/GaN quantum well structures. *Appl. Phys. Lett.*, 101(21):212107, 2012.

[127] Bruckbauer J, Edwards P R, Wang T and Martin R W. High resolution cathodoluminescence hyperspectral imaging of surface features in InGaN/GaN multiple quantum well structures. *Appl. Phys. Lett.*, 98(14):141908, 2011.

[128] Pereira S, Correia M R, Pereira E, O'Donnell K P, Trager-Cowan C, Sweeney F and Alves E. Compositional pulling effects in $In_xGa_{1-x}N$/GaN layers: A combined depth-resolved cathodoluminescence and Rutherford backscattering/channeling study. *Phys. Rev. B*, 64:205311, 2001.

[129] Pereira S, Correia M R, Pereira E, O'Donnell K P, Alves E, Sequeira A D, et al. Strain and composition distributions in wurtzite InGaN/GaN layers extracted from x-ray reciprocal space mapping. *Appl. Phys. Lett.*, 81(18):3500–3500, 2002.

[130] Pereira S, O'Donnell K P and Alves E. Role of nanoscale strain inhomogeneity on the light emission from InGaN epilayers. *Adv. Funct. Mater.*, 17(1):37–42, 2007.

[131] ODonnell K P, Fernandez-Torrente I, Edwards P R and Martin R W. The composition dependence of the $In_xGa_{1-x}N$ bandgap. *J. Cryst. Growth*, 269(1):100–105, 2004.

[132] Piner E L, Behbehani M K, El-Masry N A, Roberts J C, McIntosh F G and Bedair S M. Impurity dependence on hydrogen and ammonia flow rates in InGaN bulk films. *Appl. Phys. Lett.*, 71(14):2023–2025, 1997.

[133] Koukitu A, Taki T, Takahashi N and Seki H. Thermodynamic study on the role of hydrogen during the MOVPE growth of group III nitrides. *J. Cryst. Growth*, 197:99–105, 1999.

[134] Czernecki R, Kret S, Kempisty P, Grzanka E, Plesiewicz J, Targowski G, Grzanka S, Bilska M, Smalc-Koziorowska J, Krukowski S, Suski T, Perlin P and Leszczynski M. Influence of hydrogen and TMIn on indium incorporation in MOVPE growth of InGaN layers. *J. Cryst. Growth*, 402:330–336, 2014.

[135] Aschenbrenner T, Dartsch H, Kruse C, Anastasescu M, Stoica M, Gartner M, Pretorius A, Rosenauer A, Wagner T and Hommel D. Optical and structural characterization of AlInN layers for optoelectronic applications. *J. Appl. Phys.*, 108(6):063533, 2010.

[136] Lorenz K, Magalhães S, Franco N, Barradas N P, Darakchieva V, Alves E, Pereira S, Correia M R, Munnik F, Martin R W, O'Donnell K P and Watson I M. $Al_{1-x}In_xN$/GaN bilayers: Structure, morphology, and optical properties. *Phys. Stat. Sol. B*, 247(7):1740–1746, 2010.

[137] Ahl J-P, Hertkorn J, Koch H, Galler B, Michel B, Binder M and Holländer B. Morphology, growth mode and indium incorporation of MOVPE grown InGaN and AlInGaN: A comparison. *J. Cryst. Growth*, 398(0):33–39, 2014.

[138] Jardel O, Callet G, Dufraisse J, Piazza M, Sarazin N, Chartier E, Oualli M, Aubry R, Reveyrand T, Jacquet J C, Di Forte Poisson M A, Morvan E, Piotrowicz S and Delage S L. Electrical performances of AlInN/GaN HEMTs. A comparison with AlGaN/GaN HEMTs with similar technological process. *Int. J. Microw. Wirel. T.*, 3:301–309, 2011.

[139] Guo S, Gao X, Gorka D, Chung J W, Wang H, Palacios T, Crespo A, Gillespie J K, Chabak K, Trejo M, Miller V, Bellot M, Via G, Kossler M, Smith H and Tomich D. AlInN HEMT grown on SiC by metalorganic vapor phase epitaxy for millimeter-wave applications. *Phys. Stat. Sol. C*, 207(6):1348–1352, 2010.

[140] Medjdoub F, Carlin J F, Gonschorek M, Py M A, Grandjean N, Vandenbrouck S, Gaquiere C, DeJaeger J C and Kohn E. Small-signal characteristics of AlInN/GaN HEMTs. *Electron. Lett.*, 42(13):779–780, 2006.

[141] Kuzmik J. InAlN/(In)GaN high electron mobility transistors: some aspects of the quantum well heterostructure proposal. *Semicond. Sci. Technol.*, 17(6):540, 2002.

[142] J. Kuzmik, G. Pozzovivo, C. Ostermaier, G. Strasser, D. Pogany, E. Gornik, J.-F. Carlin, M. Gonschorek, E. Feltin, and N. Grandjean. Analysis of degradation mechanisms in lattice-matched InAlN/GaN high-electron-mobility transistors. *J. Appl. Phys.*, 106(12):124503, 2009.

[143] Kim J, Lochner Z, Ji M H, Choi S, Kim H J, Kim J S, Dupuis R D, Fischer A M, Juday R, Huang Y, Li T, Huang J Y, Ponce F A, and Ryou J H. Origins of unintentional incorporation of gallium in InAlN layers during epitaxial growth, Part II: Effects of underlying layers and growth chamber conditions. *J. Cryst. Growth*, 388(0):143–149, 2014.

[144] Zhu J J, Fan Y M, Zhang H, Lu G J, Wang H, Zhao D G, Jiang D S, Liu Z S, Zhang S M, Chen G F, Zhang B S and Yang H. Contribution of GaN template to the unexpected Ga atoms incorporated into AlInN epilayers grown under an indium-very-rich condition by metalorganic chemical vapor deposition (MOCVD) . *J. Cryst. Growth*, 348(1):25–30, 2012.

[145] Hiroki M M, Watanabe N, Maeda N, Yokoyama H, Kumakura K, and Yamamoto H. Influence of metalorganic vapor phase epitaxy regrowth on characteristics of InAlN/AlGaN/GaN high electron mobility transistors. *Jpn. J. Appl. Phys.*, 52:04CF02, 2013.

[146] Hiroki M, Oda Y, Watanabe N, Maeda N, Yokoyama H, Kumakura K and Yamamoto H. Unintentional Ga incorporation in metalorganic vapor phase epitaxy of In-containing iii-nitride semiconductors. *J. Cryst. Growth*, 382(0):36–40, 2013.

[147] Taylor E, Smith M D, Sadler T C, Lorenz K, Li H N, Alves E, Parbrook P J and Martin R W. Structural and optical properties of Ga auto-incorporated InAlN epilayers. *J. Cryst. Growth*, 408:97–101, 2014.

[148] Figge S, Böttcher T, Einfeldt S and Hommel D. In situ and ex situ evaluation of the film coalescence for GaN growth on GaN nucleation layers. *J. Cryst. Growth*, 221:262–266, 2000.

[149] Magalhães S, Barradas N P, Alves E, Watson I M, and Lorenz K. High precision determination of the InN content of $Al_{1-x}In_xN$ thin films by Rutherford backscattering spectrometry. *Nucl. Instr. & Meth. B*, 273(0):105–108, 2012.

[150] Bejtka K, Edwards P R, Martin R W, Fernández-Garrido S, and Calleja E. Composition and luminescence of AlInGaN layers grown by plasma-assisted molecular beam epitaxy. *J. Appl. Phys.*, 104(7):073537, 2008.

[151] Perillat-Merceroz G, Cosendey G, Carlin J-F, Butté R and Grandjean N. Intrinsic degradation mechanism of nearly lattice-matched InAlN layers grown on GaN substrates. *J. Appl. Phys.*, 113(6):063506, 2013.

[152] Jeynes C, Jafri Z H, Webb R P, Kimber A C and Ashwin M J. Accurate RBS measurements of the indium content of InGaAs thin films. *Surf. Interface Anal.*, 25(4):254–260, 1997.

[153] Smith M D, Taylor E, Sadler T C, Zubialevich V Z, Lorenz K, Li H N, O'Connell J, Alves E, Holmes J D, Martin R W and Parbrook P J. Determination of Ga auto-incorporation in nominal InAlN epilayers grown by MOCVD. *J. Mater. Chem. C*, 2:5787–5792, 2014.

[154] Schulz T, Albrecht M, Irmscher K, Hartmann C, Wollweber J and Fornari R. Ultraviolet luminescence in AlN. *Phys. Stat. Sol. B*, 248(6):1513–1518, 2011.

[155] Youngman R A and Harris J H. Luminescence studies of oxygen-related defects in aluminum nitride. *J. Am. Ceram. Soc.*, 73(11):3238–3246, 1990.

[156] Lijun Y, Tongbo W, Jianchang Y, Zhe L, Junxi W and Jinmin L. MOCVD epitaxy of InAlN on different templates. *J. Semicond.*, 32(9):093001, 2011.

[157] Karpov S Y, Podolskaya N I, Zhmakin I A and Zhmakin A I. Statistical model of ternary group-III nitrides. *Phys. Rev. B*, 70:235203, Dec 2004.

[158] Hums C, Bläsing J, Dadgar A, Diez A, Hempel T, Christen J, Krost A, Lorenz K and Alves E. Metal-organic vapor phase epitaxy and properties of AlInN in the whole compositional range. *Appl. Phys. Lett.*, 90(2):022105, 2007.

[159] Matsuoka T. Calculation of unstable mixing region in wurtzite $In_{1-x-y}Ga_xAl_yN$. *Appl. Phys. Lett.*, 71(1):105–106, 1997.

[160] Kim-Chauveau H, de Mierry P, Chauveau J-M and Duboz J-Y. The influence of various MOCVD parameters on the growth of $Al_{1-x}In_xN$ ternary alloy on GaN templates. *J. Cryst. Growth*, 316(1):30–36, 2011.

[161] Liu G, Zhang J, Li X-H, Huang G S, Paskova T, Evans K R, Zhao H and Tansu N. Metalorganic vapor phase epitaxy and characterizations of nearly-lattice-matched AlInN alloys on GaN/sapphire templates and free-standing GaN substrates. *J. Cryst. Growth*, 340(1):66–73, 2012.

[162] Liu J P, Wang Y T, Yang H, Jiang D S, Jahn U and Ploog K H. Investigations on V-defects in quaternary AlInGaN epilayers. *Appl. Phys. Lett.*, 84(26):5449–5451, 2004.

[163] Vennéguès P, Diaby B S, Kim-Chauveau H, Bodiou L, Schenk H P D, Frayssinet E, Martin R W and Watson I M. Nature and origin of V-defects present in metalorganic vapor phase epitaxy-grown $(In_xAl_{1-x})N$ layers as a function of InN content, layer thickness and growth parameters. *J. Cryst. Growth*, 353(1):108–114, 2012.

[164] Chung R B, Wu F, Shivaraman R, Keller S, DenBaars S P, Speck J S and Nakamura S. Growth study and impurity characterization of $Al_xIn_{1-x}N$ grown by metal organic chemical vapor deposition. *J. Cryst. Growth*, 324(1):163–167, 2011.

[165] Sadler T C, Kappers M J and Oliver R A. The effect of temperature and ammonia flux on the surface morphology and composition of $In_xAl_{1-x}N$ epitaxial layers. *J. Cryst. Growth*, 311(13):3380 – 3385, 2009.

[166] Choi S, Kim H J, Lochner Z, Kim J, Dupuis R D, Fischer A M, Juday R, Huang Y, Li T, Huang J Y, Ponce F A and Ryou J-H. Origins of unin-

tentional incorporation of gallium in AlInN layers during epitaxial growth, part i: Growth of AlInN on AlN and effects of prior coating. *J. Cryst. Growth*, 388(0):137 – 142, 2014.

[167] Wang K, Martin R W, Amabile D, Edwards P R, Hernandez S, Nogales E, O'Donnell K P, Lorenz K, Alves E, Matias V, Vantomme A, Wolverson D and Watson I M. Optical energies of AlInN epilayers. *J. Appl. Phys*, 103(7):073510, 2008.

[168] Jones R E, Broesler R, Yu K M, Ager J W, Haller E E, Walukiewicz W, Chen X and Schaff W J. Band gap bowing parameter of $In_{1-x}Al_xN$. *J. Appl. Phys*, 104(12):123501, 2008.

[169] Carlin J-F, Zellweger C, Dorsaz J, Nicolay S, Christmann G, Feltin E, Butté R and Grandjean N. Progresses in III-nitride distributed Bragg reflectors and microcavities using AlInN/GaN materials. *Phys. Stat. Sol. B*, 242(11):2326–2344, 2005.

[170] Meyer C, Sqalli O, Lorenz H and Karrai K. Slip-stick step-scanner for scanning probe microscopy. *Rev. Sci. Instrum.*, 76(6), 2005.

[171] Attocube Systems AG. Nanopositioners user manual v1.1, Modified December 2011.

[172] Kimura S and Munakata C. Method for measuring the spot size of a laser beam using a boundary-diffraction wave. *Opt. Lett.*, 12(8):552–554, 1987.

[173] Wallace M J, Edwards P R, Kappers M J, Hopkins M A, Oehler F, Sivaraya S, Allsopp D W E, Oliver R A, Humphreys C J and Martin R W. Bias dependence and correlation of the cathodoluminescence and electron beam induced current from an InGaN/GaN light emitting diode. *J. Appl. Phys.*, 116(3), 2014.

[174] Wallace M J, Edwards P R, Kappers M J, Hopkins M A, Oehler F, Sivaraya S, Oliver R A, Humphreys C J, Allsopp D W E and Martin R W. Effect of the barrier growth mode on the luminescence and conductivity micron scale uniformity of InGaN light emitting diodes. *J. Appl. Phys.*, 117(11), 2015.

[175] Oliver R A, Massabuau F C-P, Kappers M J, Phillips W A, Thrush E J, Tartan C C, Blenkhorn W E, Badcock T J, Dawson P, Hopkins M A, Allsopp D W E and Humphreys C J. The impact of gross well width fluctuations on the efficiency of GaN-based light emitting diodes. *Appl. Phys. Lett.*, 103(14), 2013.

[176] Pendlebury S T, Parbrook P J, Mowbray D J, Wood D A and Lee K B. InGaN/GaN quantum wells with low growth temperature GaN cap layers. *J. Cryst. Growth*, 307(2):363–366, 2007.

[177] Ju J-W, Kim H-S, Jang L-W, Baek J H, Shin D-C and Lee I-H. A well protection layer as a novel pathway to increase indium composition: a route towards green emission from a blue InGaN/GaN multiple quantum well. *Nanotechnology*, 18(29):295402, 2007.

[178] Leem S J, Shin Y C, Kim E H, Kim C M, Lee B G, Moon Y, Lee I H and Kim T G. Optimization of InGaN/GaN multiple quantum well layers by a two-step varied-barrier-growth temperature method. *Semicond. Sci. Technol.*, 23(12):125039, 2008.

[179] Kret S, Ivaldi F, Sobczak K, Czernecki R and Leszczyński M. Inhomogeneities of InGaN/GaN MOVPE multi quantum wells grown with a two temperatures process studied by transmission electron microscopy. *Phys. Stat. Sol. A*, 207(5):1101–1104, 2010.

[180] Thrush E J, Kappers M J, Dawson P, Graham D, Barnard J S, Vickers M E, Considine L, Mullins J T and Humphreys C J. GaN-InGaN quantum well and LED structures grown in a close coupled showerhead (CCS) MOCVD reactor. *Phys. Stat. Sol. A*, 192(2):354–359, 2002.

[181] Graham D M, Dawson P, Godfrey M J, Kappers M J, Costa P M F J, Vickers M E, Datta R, Humphreys C J and Thrush E J. High quantum efficiency InGaN/GaN structures emitting at 540 nm. *Phys. Stat. Sol. C*, 3(6):1970–1973, 2006.

[182] Yang J, Zhao D G, Jiang D S, Chen P, Zhu J J, Liu Z S, Le L C, Li X J, He X G, Liu J P, Yang H, Zhang Y T and Du G T. Optical and structural

characteristics of high indium content InGaN/GaN multi-quantum wells with varying GaN cap layer thickness. *J. Appl. Phys.*, 117(5), 2015.

[183] Nakamura S. III-V nitride based light-emitting devices. *Solid State Commun.*, 102:237–248, 1997.

[184] Bayliss S C, Demeester P, Fletcher I, Martin R W, Middleton P G, Moerman I, O'Donnell K P, Sapelkin A, Trager-Cowan C, Van Der Stricht W and Young C. The optical and structural properties of InGaN epilayers with very high indium content. *Mat. Sci. Eng. B*, 59:292–297, 1999.

[185] Edwards P R, Martin R W, O'Donnell K P and Watson I M. Simultaneous composition mapping and hyperspectral cathodoluminescence imaging of InGaN epilayers. *Phys. Stat. Sol. C*, 0(7):2474–2477, 2003.

[186] Chichibu S F, Abare A C, Mack M P, Minsky M S, Deguchi T, Cohen D, Kozodoy P, Fleischer S B, Keller S, Speck J S, Bowers J E, Hu E, Mishra U K, Coldren L A, DenBaars S P, Wada K, Sota T and Nakamura S. Optical properties of InGaN quantum wells. *Mat. Sci. Eng. B*, 59(13):298–306, 1999.

[187] Kuroda T and Tackeuchi A. Influence of free carrier screening on the luminescence energy shift and carrier lifetime of InGaN quantum wells. *J. Appl. Phys.*, 92(6):3071–3074, 2002.

[188] Davidson J A, Dawson P, Wang T, Sugahara T, Orton J W and S Sakai S. Photoluminescence studies of InGaN/GaN multi-quantum wells. *Semicond. Sci. Technol.*, 15(6):497, 2000.

[189] Chichibu S F, Abare A C, Minsky M S, Keller S, Fleischer S B, Bowers J E, Hu E, Mishra U K, Coldren L A, DenBaars S P and Sota T. Effective band gap inhomogeneity and piezoelectric field in InGaN/GaN multiquantum well structures. *Appl. Phys. Lett.*, 73(14):2006–2008, 1998.

[190] Graham D M, Soltani-Vala A, Dawson P, Godfrey M J, Smeeton T M, Barnard J S, Kappers M J, Humphreys C J and Thrush E J. Optical and microstructural studies of InGaN/GaN single-quantum-well structures. *J. Appl. Phys.*, 97(10), 2005.

[191] van der Laak N K, Oliver R A, Kappers M J and Humphreys C J. Role of gross well-width fluctuations in bright, green-emitting single InGaN/GaN quantum well structures. *Appl. Phys. Lett.*, 90(12), 2007.

Conference Contributions

The oral and poster contributions presented below are for both attended and unattended conferences. My contribution is highlighted in bold and the presenting author is indicated by an underline.

- 9th International Conference on Nitride Semiconductors, Glasgow, UK, July 2011:
  Poster - **E. Taylor**, Paul R. Edwards, and R. W. Martin, *"Colorimetry and efficiency of white LEDs: Spectral width dependence"*.

- UK Nitrides Consortium Summer Meeting, Sheffield, UK, July 2012:
  Talk - **E. Taylor**, F. Fang, P. R. Edwards, M. J. Kappers, C. J. Humphreys, and R. W. Martin, *"Composition and luminescence mapping of InGaN layers grown at different hydrogen flow rates"*.

- University of Strathclyde Postgraduate Physics Conference, Glasgow, UK, August 2012:
  Talk - **E. Taylor**, F. Fang, P. R. Edwards, M. J. Kappers, C. J. Humphreys, and R. W. Martin, *"Characterisation of InGaN epilayers grown at different hydrogen flow rates"*.

- International Workshop on Nitrides, Sapporo, Japan, October 2012:
  Poster - T. C. Sadler, **E. Taylor**, Z. Quan, M. Caro, H. Li, M. A. Conroy, V. Zubialevich, R. W. Martin, and P. J. Parbrook, *"Flip Chip Ultraviolet Light Emitting Diodes Utilising Polarisation Matched InAlN/AlGaN"*.

- UK Nitrides Consortium Winter Meeting, Cardiff, UK, January 2013:
  Talk - J. Bruckbauer, N.J. Findlay, S. Arumugam, G. Conboy, **E. Taylor**,

A.R. Inigo, P.R. Edwards, J. Bai, T. Wang, P.J. Skabara, and R.W. Martin, *"White light emission from InGaN/GaN nanorod LEDs using an organic compound for colour down conversion"*.

- 'Lighting the Future' Programme Grant Workshop, Cambridge, UK, July 2013:
  Talk - **E. Taylor**, P. R. Edwards, and R. W. Martin, *"Photoluminescence mapping of InGaN/GaN quantum well samples and LEDs"*.

- UK Nitrides Consortium Winter Meeting, Bristol, UK, January 2014:
  Talk - **E. Taylor**, M. D. Smith, T. C. Sadler, K. Lorenz, H. N. Li, V. Z. Zubialevich, V. D. Dinh, E. Alves, P. J. Parbrook, and R. W. Martin, *"Composition and luminescence studies of MOCVD grown AlInN layers with and without Ga auto-incorporation"*.

- International Workshop on Nitrides, Wroclaw, Poland, August 2014:
  Poster - **E. Taylor**, M. D. Smith, T. C. Sadler, K. Lorenz, H. N. Li, E. Alves, P. J. Parbrook, and R. W. Martin, *"Structural and optical properties of Ga auto-incorporated InAlN epilayers"*.

- 13th European Vacuum Conference, Aveiro, Portugal, September 2014:
  Poster - J.M.D. Sabino, A. Redondo-Cubero, N. Franco, E. Alves, P.J. Parbrook, **E. Taylor**, R.W. Martin, and K. Lorenz, *"Self-Consistent Analysis Of Near-Lattice Matched AlGaInN Epitaxial Layers"*.

- The 23rd European Workshop on Heterostructure Technology, Rauischholzhausen, Germany, October 2014:
  Talk - A. Núñez-Cascajero, L. Monteagudo-Lerma, M. Jiménez-Rodríguez, S. Valdueza-Felip, E. Monroy, **E. Taylor**, R.W. Martin, M. González-Herráez, and F.B. Naranjo, *"High In content AlInN layers grown on sapphire and p silicon (111) substrates by RF sputtering"*.